Relationships between hydrological processes and remote sensing reflectance in tidally stirred shelf seas

Claire Neil

A thesis presented in fulfilment of the requirements for the degree of Doctor of Philosophy

Department of Physics
University of Strathclyde
107 Rottenrow
Glasgow, G4 0NG

Supervisor: Professor A. Cunningham

Declaration of Author's Rights

This thesis is the result of the author's original research. It has been composed by the author and has not been previously submitted for examination which has led to the award of a degree.

Date:
Signed:

Abstract

Marked temporal and spatial variations in reflectance measured at red wavelengths are frequently observed in the Irish Sea. The obvious existence of seasonal variability suggests that the reflectance in this region may be spatially correlated with physical processes. This study investigates the feasibility of obtaining information on hydrological as opposed to biogeochemical processes from remote sensing reflectance spectra measured over tidally stirred shelf seas. As a first step, the correlation between remote sensing reflectance at 667 nm ($R_{rs}667$) and the concentration of mineral suspended solids (MSS) as investigated, and its sensitivity to the presence of other optically significant materials (OSM) quantified by a combination of radiative transfer modelling and water sample analysis. Modelled reflectance spectra were generated using inherent optical properties representative of a coastal environment. The uncertainty in the MSS retrieval varied with OSM values and was best indicated by explicitly stating the range of MSS concentrations that would be associated with a given R_{rs} signal. Results indicate that the correlation is sufficiently robust in these waters to allow reflectance to be used as an indicator of MSS concentrations and, by implication, of spatial variability in the hydrological processes on which they depend. Relationships between $R_{rs}667$ and stratification parameter delta sigma, $\Delta\sigma$, or maximum bed shear stress, τ_{max}, were investigated using MODIS ocean colour data and model derived hydrology (POLCOMS). For the majority of the test site, the relationship between $R_{rs}667$ and $\Delta\sigma$ exists as a simple power law. Furthermore, in shallow coastal regions, variability in $R_{rs}667$ can be attributed to seasonal changes in τ_{max}. Results are twofold; they demonstrate the potential of exploiting satellite images to provide information on shelf sea dynamics. They also indicate that a greater understanding of the links between biogeochemical processes and physical hydrology is necessary to accurately represent the shelf sea ecosystem.

Acknowledgements

I would like to express my gratitude to the following people who made this work possible; to my supervisor Professor Alex Cunningham for his continued support and guidance, to Dr David McKee for his encouragement and invaluable advice, to Jordan for his unwavering patience and empathy and to my parents and Gran who always knew I would do it.

Table of contents

Chapter 1

Introduction

1.1 Modelling the shelf sea ecosystem

Shelf seas are amongst the most productive and dynamic of marine environments. Their value lies in the proximity to land, providing access for fishing, transport and recreational purposes. As a consequence, they are also highly endangered and are particularly sensitive to changes brought on by pollution and over-use. It is clear that sustained use and protection of shelf seas must be accompanied by regular monitoring and efficient management (Borja, 2005 and Robinson, 2008). This relies on the ability to describe and predict present and future states of the marine environment through the establishment of ecosystem models. The shelf sea ecosystem is complex and convoluted, where biogeochemical dynamics are strongly influenced by the physical processes in which they are embedded. Therefore, accurate representation requires a multidisciplinary approach with thorough knowledge of both biogeochemical and physical processes. The model must also satisfy a number of criteria; adequate spatial and temporal scales to effectively describe short and long term processes, coupling between biological parameters and physical forces influencing variability in coastal regions and assimilation of observational data for validation and calibration. For this purpose, satellite remote sensing plays a crucial role, offering unprecedented access to measurements of oceanic parameters, such as sea surface height, surface winds and ocean colour, acquired at synoptic frequency and mesoscale resolution. Since an orbiting sensor can view every square kilometre of cloud-free ocean every 48 hours, satellite-acquired ocean colour data constitute a valuable tool for determining the abundance of ocean biological products and can be used to assess physical changes over prolonged periods. Whilst some physical parameters are produced at a satisfactory level of accuracy, biogeochemical products derived from ocean colour lack sufficient accuracy for operational assimilation. Improving the quality of products retrieved

from optical measurements of shelf seas is therefore a fundamental objective of the ocean colour community.

1.2 Overview of ocean colour remote sensing in shelf seas

Ocean colour is the spectral distribution of solar radiation emitted from the surface of the ocean in the visible and near-infrared regimes. It is determined by the concentration of optically significant constituents suspended or dissolved in the surface layer of the water column. Light entering the ocean is subject to a series of absorption, elastic and inelastic scattering interactions (with water and constituent components) and re-emerges with a modified spectral composition. Measured remotely by radiometric sensors mounted on earth observation satellites, reflectance signals detected at the top of the atmosphere are converted to water-leaving radiance by application of a series of correction routines (Gordon, 1997, Ruddick, et al., 2000 and Vermote et al., 2002). Radiance spectra are utilised for the derivation of in-water constituents using empirical relationships or model based algorithms (Schiller & Doerffer, 1999, Sathyendranath et al., 2001 and Binding et al., 2003). These provide useful information on the state of our oceans, for example, quantitative estimates of chlorophyll concentration are used to investigate phytoplankton biomass (Gohin et al., 2002). Conversion techniques perform at varied, and often insufficiently characterised, levels of accuracy, particularly in optically complex shelf seas. In these regions at least three independently varying substances, chlorophyll (CHL) (taken as a proxy for phytoplankton biomass), mineral suspended solids (MSS) and coloured dissolved organic matter (CDOM), are contributing to the optical properties of the water column, and rendering simple recovery procedures challenging. It is well understood that an alternative approach is necessary to interpret reflectance signals taken from shelf seas (IOCCG, 2000). This is reflected in the literature, where new techniques and retrieval methods are presented focussing on these optically complex regions. Recent approaches based on neural networks or spectral matching offer substantially improved performance, but they rely heavily on the quality of the spectral libraries which are employed. The difficult nature of the problem calls for a greater understanding of the mechanisms driving reflectance variability (Robinson, 2008).

This study investigates the extent to which relationships exist between the physical dynamics of the water column and the optical signal measured at the sea surface. This is a move towards a more complete understanding of the shelf sea ecosystem. By considering an intermediate step in the inversion process, i.e. the physics, not the biogeochemistry influencing the reflectance signal, additional information may be extracted from the ocean colour signal if it can be demonstrated that the surface signals are driven by processes deeper in the water column. The existence of a potential link can be explored using patterns of suspended particulate matter as a tracer of the hydrodynamics. Quantitative estimates derived from ocean colour imagery will provide insight into spatial and temporal fate of sediments in shelf seas. Detailed clarification of correlations between remote sensing reflectance and water column hydrology are potentially useful for model calibration and validation. This will assist with assimilation of satellite data into ecosystem models. Relationships are also providing conditions for the choice of locally tuned algorithms for improved interpretation of shelf sea satellite images (Dobrynin et al., 2010).

1.2.1 Basic principles

Radiative transfer theory is concerned with the change in direction and intensity of radiation in the atmosphere and ocean, due to absorption, scattering, fluorescence, inelastic scattering and air-sea interface effects (Zaneveld et al., 2005). Interpretation of ocean colour relies on a complete knowledge of radiative transfer processes. The modulated spectral distribution of radiation received at the top of the atmosphere is a function of the geometric structure of light and the properties of the ocean and atmosphere. Radiometry defines the fundamental quantities necessary to conduct radiative transfer studies. Properties directly derived from the light field, known as apparent optical properties (AOP), are characteristic of both the medium and the geometric (directional) structure of the radiance distribution. These are influenced by inherent optical properties (IOP), which depend only upon the medium through which light is propagating.

i) Radiometry

Light can be envisioned as consisting of packets of electromagnetic energy, called photons, which travel through vacuum at speed $c = 2.998 \times 10^8$ m s^{-1}. The energy of a photon, q, is related to its frequency, v, and consequently its wavelength, λ;

$$q = hv = \frac{hc}{\lambda} \tag{1.1}$$

where h is Planck's constant ($h = 6.626 \times 10^{-34}$ J s). The linear and angular momentum transported to the oceans by incident sunlight is negligible when compared to the momentum transferred by wind and waves (Mobley, 1994). Thus the physical importance of sunlight incident on the sea surface lies in its energy transport. The amount of energy per unit time, or radiant power, Φ, that arrives at a particular area, A, from a given solid angle, Ω, is described by the radiance;

$$L(\theta, \varphi, \lambda) = \frac{d^2\Phi}{dA d\Omega d\lambda} \tag{1.2}$$

where nadir, θ, and azimuthal, φ, angles define the direction of light. This is the fundamental parameter in ocean optics from which all other radiometric quantities can be derived. When projected onto a planar surface, the contribution of each photon is weighted by the cosine of the incident angle, θ, to account for the geometric change in surface area;

$$\frac{L(\theta, \varphi, \lambda)}{\cos\theta} = \frac{d^2\Phi}{dA \cos\theta d\Omega d\lambda} \tag{1.3}$$

Radiance has units of watts per unit area per solid angle per wavelength interval (W m^{-2} sr^{-1} nm^{-1}). Measurements of radiance restrict incoming light to a specific direction defined by the solid angle. By considering photons travelling in a full hemisphere of directions, the upward, E_u, and downward, E_d, plane irradiance is obtained in relation to L;

$$E_d = \int_{2\pi}^{0} L(\theta,\varphi)\cos\theta d\Omega \tag{1.4}$$

$$E_u = \int_{-2\pi}^{0} L(\theta,\varphi)\cos\theta d\Omega \tag{1.5}$$

Measured in (W m^{-2} nm^{-1}), this is the integrated flow of light through a horizontal surface. The intensity, *I*, can also be defined in terms of radiance, *L*;

$$I = \frac{d\Phi}{d\Omega} = \int_{\Delta A} L(\theta,\varphi)dA \tag{1.6}$$

ii) Apparent optical properties

At a given wavelength λ, the reflectance, *R*, just below the sea surface (depicted by 0^- or 0^+ for above surface measurement in air) is determined by the ratio of upwelling to downwelling irradiance, E_u, and E_d, respectively (Mobley, 1999);

$$R(0^-,\lambda) = \frac{E_u(0^-,\lambda)}{E_d(0^-,\lambda)} \tag{1.7}$$

Remote sensing reflectance, R_{rs}, a radiometric parameter commonly referred to in ocean colour remote sensing, exploits the upward facing component of radiance, L_u, propagated through the air-water interface to give water-leaving radiance, L_w. R_{rs} is defined as;

$$R_{rs}(\theta,\varphi,\lambda) = \frac{L_w(\theta,\varphi,\lambda)}{E_d(0^+,\lambda)} \tag{1.8}$$

Water-leaving radiance L_w, measured just above the sea surface, is the radiance backscattered out of the water into direction (θ, ϕ). To obtain R_{rs} from field observations, subsurface radiance and irradiance are often converted to above surface values;

$$L_w(\theta,\varphi,\lambda)=\left[\frac{(1-r_F(\theta,\theta'))}{n^2}\right]L_u(0^-,\theta',\varphi',\lambda) \tag{1.9}$$

where $r_F(\theta,\theta')$ is the Fresnel reflectance as seen from the water side. For L_w, transmission through the surface must account for different refractive indices, n, of air and seawater (air having a refractive index of ~1). Notations θ' and ϕ' indicate deviation from the original direction of light which can be related by Snell's Law.

$$E_d(0^+,\lambda)=E_d(0^-,\lambda)\left[\frac{(1-R_s)}{1-RR_u}\right] \tag{1.10}$$

Here, R_s and R_u are irradiance reflectances of the surface from the air and water side respectively. From in-situ measurements of L_u and E_d, R_{rs} can be obtained;

$$R_{rs}(\theta,\varphi,\lambda)=\left\{\frac{[1-r_F(\theta,\theta')(1-R_s)]}{n^2(1-RR_u)}\right\}\times\frac{L_u(0^-,\theta',\varphi',\lambda)}{E_d(0^-,\lambda)}=T\frac{R(0^-,\lambda)}{Q(\theta',\varphi',\lambda)} \tag{1.11}$$

where T is the coefficient in curly brackets, $R(0^-,\lambda)$ is defined in equation (1.7) and $Q(\theta',\phi',\lambda) = E_u(0^-,\lambda)/L_u(0^-,\theta',\phi',\lambda)$. The terms R_s and R_u are small and are commonly omitted from the R_{rs} expression.

Other AOP parameters of use include diffuse attenuation coefficients. These describe the depth dependency of radiance and irradiance, which decrease in magnitude approximately exponentially with water column depth, z. Spectral diffuse attenuation coefficients (m^{-1}) for downward irradiance, $K_d(z,\lambda)$, upward irradiance, $K_u(z,\lambda)$, and radiance, $K(z,\theta,\phi,\lambda)$ are given by the following expression;

$$K_d(z,\lambda)=-\frac{d\ln E_d(z,\lambda)}{dz}=-\frac{1}{E_d(z,\lambda)}\frac{dE_d(z,\lambda)}{dz} \tag{1.12}$$

Diffuse attenuation coefficients have several useful applications, including estimations of the depth viewable by satellite sensors ($1/K_d$).

iii) Inherent optical properties

As light passes through a volume of water ΔV, a portion of the incident radiant power, Φ_i, is transmitted through the volume, Φ_t , whilst the remainder is scattered out of the beam, Φ_s or absorbed by the medium Φ_a. If scattering processes are elastic, by conservation of energy;

$$\Phi_i(\lambda) = \Phi_t(\lambda) + \Phi_s(\lambda) + \Phi_a(\lambda) \tag{1.13}$$

The spectral absorptance, $A(\lambda)$, scatterance, $B(\lambda)$ and transmittance, $T(\lambda)$, are determined by the fraction of incident power utilised by each process ($A(\lambda) + B(\lambda) + T(\lambda) = 1$). Coefficients of spectral absorption, $a(\lambda)$, and scattering, $b(\lambda)$, are obtained by considering the absorptance and scatterance per unit length of medium, Δr, (m^{-1});

$$a(\lambda) = \lim_{\Delta r \to 0} \frac{A(\lambda)}{\Delta r} \tag{1.14}$$

$$b(\lambda) = \lim_{\Delta r \to 0} \frac{B(\lambda)}{\Delta r} \tag{1.15}$$

The spectral beam attenuation coefficient is defined as;

$$c(\lambda) = a(\lambda) + b(\lambda) \tag{1.16}$$

By considering only photon energy scattered in a particular direction, $\psi(\theta,\varphi)$, centred on a given solid angle $\Delta\Omega$, the spectral volume scattering function (VSF) can be obtained;

$$\beta(\psi,\lambda) = \lim_{\Delta r \to 0 \Delta\Omega \to 0} \frac{B(\lambda)}{\Delta r \Delta\Omega} = \lim_{\Delta r \to 0 \Delta\Omega \to 0} \frac{\Phi_s(\psi,\lambda)}{\Phi_i(\lambda)\Delta r \Delta\Omega} \tag{1.17}$$

Since $E_i = \Phi_i / \Delta A$, and $\Phi_s(\psi,\lambda) = I_s \Delta\Omega$;

$$\beta(\psi,\lambda) = \lim_{\Delta A\to 0 \Delta\Omega\to 0} \frac{I_s(\psi,\lambda)}{E_i(\lambda)\Delta A \Delta r} = \lim_{\Delta V\to 0} \frac{I_s(\psi,\lambda)}{E_i(\lambda)\Delta V} \quad (1.18)$$

This describes the angular distribution of scattered light in the water ($m^{-1}sr^{-1}$). Integrating over all angles produces the scattering coefficient, $b(\lambda)$, whilst backscattering, $b_b(\lambda)$, is obtained by restricting integration to angles greater than 90^o;

$$b_b(\lambda) = 2\pi \int_{\pi/2}^{\pi} \beta(\psi,\lambda) \sin\psi d\psi \quad (1.19)$$

The ratio of the volume scattering function and the scattering coefficient produces a parameter which describes the distribution of scattering per solid angle, known as the spectral scattering phase function (sr^{-1});

$$\tilde{\beta}(\psi,\lambda) = \frac{\beta(\psi,\lambda)}{b(\lambda)} \quad (1.20)$$

Finally, the spectral single scattering albedo, ω_0, determines the proportion of attenuation due to scattering;

$$\omega_0(\lambda) = \frac{b(\lambda)}{c(\lambda)} \quad (1.21)$$

The volume scattering function and absorption coefficient are the two basic IOPs from which all others can be derived.

For the purpose of radiance transfer, it is the total IOPs of the water column which are of interest. These are determined by the combination of dissolved or suspended optically significant constituents found in shelf seas. In addition to water molecules, optically significant constituents influencing the light leaving the surface of a shelf sea are CHL, MSS and CDOM. Suspended particles can be of biological or physical nature, and contain variable absorption and scattering properties. Phytoplankton, which falls into the organic category, is a strong absorber of light. Due to the

chlorophyll a pigment, phytoplankton absorption is enhanced in the blue and red regions of the visible spectrum. Inorganic suspended particles, which are strong scatterers of light and absorb mainly at short wavelengths, are highly optically significant in shelf seas. Similarly, dissolved matter, which predominantly originates from decaying vegetation, is common to coastal regions. CDOM absorbs greatly in the blue region of the visible spectrum, becoming exponentially less significant at longer wavelengths. It does not contribute to the scattering properties of the water column. Each of these components contributes individually to the total IOP, altering the bulk absorption, a, and scattering, b, or backscattering, b_b, coefficients of the medium. Total IOP budgets are established by the summing the various contributions of constituents and seawater;

$$a(\lambda) = a_w(\lambda) + a_{CHL}(\lambda) + a_{MSS}(\lambda) + c_{CDOM}(\lambda) \tag{1.22}$$

$$b_b(\lambda) = b_{b_W}(\lambda) + b_{b_{CHL}}(\lambda) + b_{b_{MSS}}(\lambda) \tag{1.23}$$

To determine individual contributions, IOPs can be expressed as a product of the constituent specific IOPs and concentrations of the constituents, assuming the dimension and shape of constituent particles are consistent. For example, suspended sediment absorption, a_{MSS}, is given by ($a^*_{MSS}MSS$), where the specific IOP is denoted by superscript asterisk, the subscript MSS denotes the relevant constituent and MSS is the constituent concentration. The bulk absorption a and backscattering b_b can be expressed as the sum of the individual components (λ, dropped for brevity);

$$a = a_w + a^*_{CHL} CHL + a^*_{MSS} MSS + c^*_{CDOM} CDOM \tag{1.24}$$

$$b_b = b_{b_W} + b^*_{b_{CHL}} CHL + b^*_{b_{MSS}} MSS \tag{1.25}$$

where subscript w indicates the contribution by sea water.

iv) Relationships between inherent and apparent optical properties

Light leaving the water column and corresponding constituent concentrations can be connected through relationships between AOPs and IOPs. In these examples, notations, θ, ϕ, θ', ϕ' and λ have been dropped for brevity. Irradiance reflectance just below the surface is obtained by the ratio of backscattering to absorption coefficient;

$$R = f \times \frac{b_b}{a} \tag{1.26}$$

Therefore, from equation (1.11) the remote sensing reflectance is given by;

$$R_{rs} = T \frac{f}{Q} \frac{b_b}{a} \tag{1.27}$$

where T and Q are defined previously. The factor f, is a geometric parameter which relates the backscattering and absorption properties of the water to reflectance. It is predominantly dependent on the distribution of the ambient light field and the viewing angle of the sun and satellite (Barnard et al., 1999, Ladner et al., 2002 and Lee et al., 2004). However it also changes in response to varying VSF, which in turn depends on particle characteristics. This is also true for Q, the ratio of upwelling radiance to irradiance. Minimum values of f / Q are obtained when the sun is at zenith and increase with increasing zenith angle. In shelf seas, values of f / Q fall within the range 0.05 to 0.2 (Morel & Gentili, 1993, Morel et al., 2002)

Combining equations (1.24) and (1.25), equation (1.27) can be expanded to include all possible optically significant constituents found in shelf seas;

$$R_{rs} = F\left(\frac{b_{b_w} + b^*_{b_{MSS}} MSS + b^*_{b_{CHL}} CHL}{a_w + a^*_{MSS} MSS + a^*_{CHL} CHL + a^*_{CDOM} CDOM} \right) \tag{1.28}$$

Here, F, denotes R_{rs} is a function of the terms in brackets. From equation (1.28), there are five parameters that could potentially alter the remote sensing signal, the

backscattering, b_b, and absorption, a, coefficients derived from specific IOPs for MSS and CHL, and derived absorption due to CDOM.

1.2.2 Radiance transfer equation (RTE)

The radiance transfer equation, required to effectively model the underwater light field, describes all processes affecting the change in radiance along a given path. Consider a beam of light entering a volume of medium, ΔV, from direction $\zeta(\theta,\varphi)$. Along path length Δr, the incident radiant power will experience gains and losses due to absorption and scattering processes within the path.

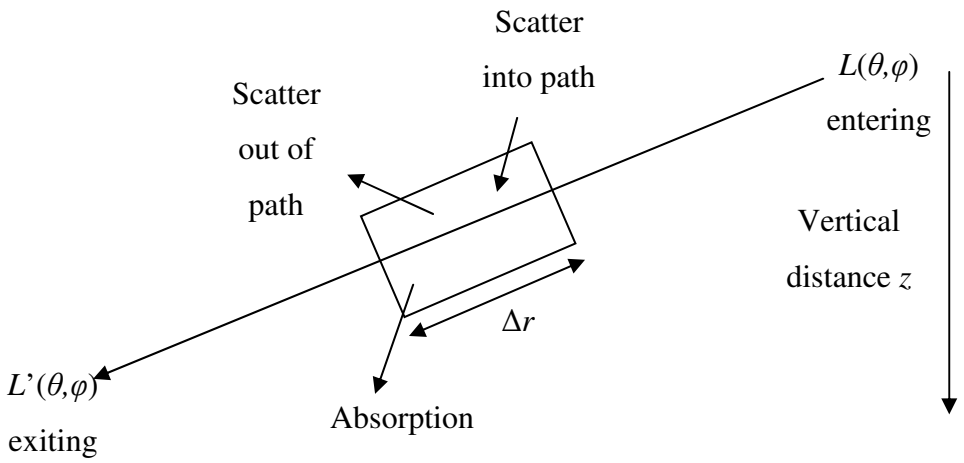

Figure 1.1 Change in radiance along a given directional path. Losses occur due to absorption and scattering out of the path Δr, whilst gains in radiance can be attributed to scattering into the path.

On a molecular and atomic scale, when molecules absorb visible light, the incoming energy excites electrons to a higher internal (electronic, vibrational or rotational) energy state. If the photon energy exactly matches the molecular transition it may be completely absorbed and converted to non-radiant energy. This is the process of true absorption. Elastic scattering occurs when the molecule instantaneously returns to its original state by emission of a photon with the same energy. If the photon experiences a photon change, as occurs in Raman scattering or fluorescence,

scattering is described as inelastic. True emission is possible where non-radiant energy is converted into light, for example, bioluminescence. Formulation of the radiance transfer equation must account for each process. Losses from the radiance path may be attributed to photon annihilation due to absorption of radiant energy or the scattering of photons from the beam (elastic or inelastic). In the absence of external sources, photon gain in a given direction is solely the result of scattering into the beam. However, the creation of radiant energy through true emission processes such as bioluminescence may also contribute to photon gain. Processes required for the equation of transfer are shown schematically in Figure 1.2.

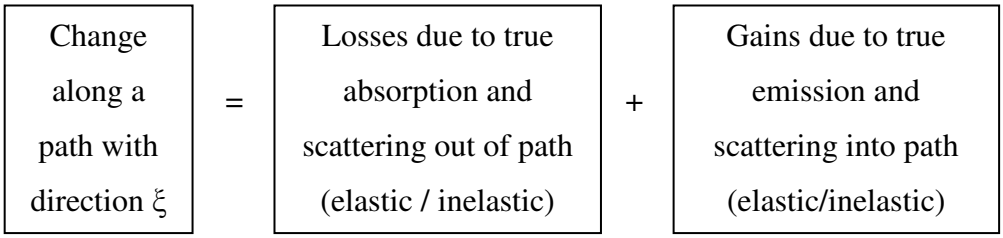

Figure 1.2 Schematic description of the processes involved in defining the radiance transfer equation.

i) Radiance transfer gains

Photons scattered into a light beam in direction, ξ, produce an observed spectral radiance, $L_{\Delta r}(\xi,\lambda)$ which per unit distance provides the path function for elastic scattering, L_*^E ;

$$L_*^E = \frac{L_{\Delta r}(\xi,\lambda)}{\Delta r} \tag{1.29}$$

Assuming the generated radiance per unit length is proportional to the incident spectral irradiance, E_i, from direction ξ', falling on ΔV, the proportionality constant is given by;

$$\beta(\xi' \rightarrow \xi, \lambda) = \frac{L_{\Delta r}(\xi, \lambda)/\Delta r}{E_i(\xi', \lambda)} \tag{1.30}$$

Spectral irradiance, written in terms of radiance gives;

$$E_i(\xi', \lambda) = L(\xi', \lambda)\Delta\Omega(\xi') \tag{1.31}$$

Therefore, combining equations (1.30) and (1.31) and integrating over all ξ' in the domain, Ξ, provides the path function in relation to the incident radiance and VSF (Mobley, 1994);

$$L_*^E = \int_{\xi' \in \Xi} L(\xi', \lambda)\beta(\xi' \rightarrow \xi, \lambda)d\Omega(\xi') \tag{1.32}$$

A similar expression describes gain due to inelastic scattering in the medium, L_*^I;

$$L_*^I = \int_{\Xi}\int_{\Lambda} L(\xi', \lambda)\beta(\xi' \rightarrow \xi, \lambda \rightarrow \lambda')d\lambda' d\Omega(\xi') \tag{1.33}$$

Here the double integral accounts for changes in wavelength owing to inelastic scattering into direction ξ and wavelength λ, by photons of all other wavelengths, λ', in the electromagnetic spectrum, Λ. Radiant energy gain is a function of the angular distribution of scattering.

Gain by true emission depends on the particular emission process and is described by the source path function, L_*^S. Commonly, L_*^S, and L_*^I are combined to generate the effective source function, S, (which is frequently considered known in natural waters).

$$S = L_*^I + L_*^S \tag{1.34}$$

ii) Radiance transfer losses

As described previously, true absorption occurs in a medium when incident photons are absorbed and their corresponding energy is converted to non-radiant energy. The true absorption coefficient is denoted with superscript e, $a^e(\lambda')$. Alternatively, radiant power can be lost through inelastic absorption where emitted photons contain a fraction of the incident energy. The inelastic absorption coefficient a^I, is related to the inelastic scattering coefficient, b^I, through the expression;

$$a^I(\lambda') = \int_\Lambda b^I(\lambda' \rightarrow \lambda) d\lambda \tag{1.35}$$

The integral of b^I describes how strongly light is transferred from wavelength, λ' to all other wavelengths. The total absorption coefficient is the additive combination of both absorption processes;

$$a(\lambda') = a^e(\lambda') + a^I(\lambda') \tag{1.36}$$

Finally, photons scattered from a collimated beam of light also enhance loss of radiant power, $b(\lambda)$. Decrease in radiance through a medium is proportional to the radiance and the distance;

$$\frac{\Delta L(\xi,\lambda)}{\Delta r} = -\left[a^e(\lambda) + a^I(\lambda) + b(\lambda)\right] L(\xi,\lambda) = -c(\lambda) L(\xi,\lambda) \tag{1.37}$$

All possible losses of radiant power from a collimated beam of photons are accounted for by the beam attenuation coefficient, $c(\lambda)$.

iii) Standard form of RTE

In terms of geometric depth and VSF, the standard form of the radiance transfer equation is given by;

$$\frac{dL(z,\xi,\lambda)}{dr} = \mu \frac{dL(z,\xi,\lambda)}{dz} = -c(z,\lambda)L(z,\xi,\lambda) + \int_{\Xi} L(z,\xi',\lambda)\beta(z,\xi \to \xi',\lambda)d\Omega(\xi') + S(z,\xi,\lambda) \tag{1.38}$$

Here, $dr = dz / \mu = dz / cos\theta$. This describes the radiant power gains and losses necessary to predict the underwater light field (source parameter S is not considered further in this study). It also shows that accurate representation relies on the proficient measurement of four parameters, a, b, $\tilde{\beta}$ and z.

1.2.3 State of the art

Ocean colour remote sensing began in 1978 with the successful launch of NASA's Coastal Zone Color Scanner (CZCS) on NIMBUS-7. This was an experimental mission devoted to the measurement of ocean colour. With six spectral bands, the primary objective of the CZCS mission was to determine if satellite remote sensing of colour could be used to identify and quantify material suspended or dissolved in ocean waters. The success of the mission, which lasted almost a decade, provided justification for the development and application of future missions. However, there followed a significant gap of 10 years before the launch of the next operational ocean colour sensor. In 1996, India launched IRS-P3, which housed the German Modular Optical Scanner (MOS), quickly followed by Japan with ADEOS-1 (OCTS), which lasted only 10 months, and the US with SeaStar (SeaWiFS). This instigated a series of earth observation missions, with scientific contributions to satellite ocean colour measurements provided from space agencies worldwide, including China, Korea and Europe.

At the time of writing, 12 historical sensors have ceased to function, whilst 9 remain operational. The majority of past and present ocean colour sensors are mounted on polar orbiting satellite platforms, providing near global coverage every 1-2 days. The spatial resolution of images recorded by current instrumentation ranges from 250 to

6000 m with swath widths between 200 and 2800 km. Ocean colour measurements are most commonly made at multiband spectral resolution, with MODIS Aqua and Terra containing the maximum number of spectral wavebands (36 bands). The first hyperspectral instrument (> 100 bands) was released in 2009, onboard the International Space Station (ISS). This instrument combines high spectral resolution (124 bands between 380 – 1000 nm) with high spatial resolution (100 m), however it is limited to 50 km swaths orbiting between ± 51.6º latitude. 2010 also saw a new development in ocean colour remote sensing with the introduction of the first geostationary satellite dedicated to ocean colour measurement. The South Korean COMS satellite centred on the Korean peninsula generates hourly temporal coverage of a 2500 km^2 region. With a spatial resolution of 500 m, this instrument provides the capability of monitoring physical and biological processes at tidal and diurnal scales.

The continuous global time series of ocean colour measurements currently provided by the SeaWiFS, MODIS and MERIS group of sensors is of increasing importance for monitoring long term changes in ocean conditions and associated climatic variability. This time series is expected to be extended with the launch of an additional 8 sensors proposed by 2015.

1.2.4 Capabilities and limitations

Through its sensitivity to materials suspended and dissolved in the water column, ocean colour remote sensing provides a unique window into biogeochemical processes occurring in surface layers of the ocean. The primary parameter monitored through ocean colour remote sensing is the concentration of chlorophyll, an index of phytoplankton biomass. Phytoplankton are microscopic single or multi-celled plants found floating in the oceans. They contribute up to 25% of the total vegetation in the sea and are a major source of food for many marine animals (Falkowski & Raven, 1997). Phytoplankton use photosynthesis to convert light energy into chemical energy, in the process removing carbon dioxide from the atmosphere and supplying oxygen as a by product. Because of these two main features, phytoplankton are extremely important and their activities integrated over time are significant enough to influence global environmental change. Ocean colour remote sensing plays a crucial

role in monitoring chlorophyll concentration on a global scale. However its exploitation offers many societal benefits in addition to the retrieval of chlorophyll. The following section contains a summary of potential applications as defined the IOCCG in their 2008 report (IOCCG, 2008).

1.2.4a Applications of ocean colour remote sensing

i) Ecosystem modelling

As discussed previously in this chapter, oceanic parameters retrieved remotely by satellite instrumentation are essential for initialisation and validation of ocean numerical models. The application of ocean colour data is required for two functions; to improve the understanding of processes influencing constituent variability and to allow prediction of future and current state for operational purposes. Coupling between satellite measurements and modelling enhances the quality and quantity of information obtained by each individually.

ii) Ocean physics

The distribution of constituents in shelf seas is intimately linked to hydrodynamic processes. For example phytoplankton growth relies on the supply of nutrients to the surface mixed layer, which in turn is determined by physical processes such as advection and mixing. Coincident analysis with biogeochemical dynamics can be used to identify the underlying physical mechanisms responsible for observed biological features. Ocean colour remote sensing therefore provides insight into the physical forces driving variability in shelf seas.

iii) Biogeochemical cycles

Remote observations of ocean colour from space are directly related to various components of biogeochemical cycles, including the exchange of CO_2 with the atmosphere through the sea surface, conversion of CO_2 into organic carbon by phytoplankton photosynthesis, and loss of carbon by settling of particulate matter or by diffusive transport. Ocean colour radiometry allows investigation of carbon fluxes in the ocean and serves as an essential tool for quantifying aspects of biogeochemical cycles.

iv) Fisheries

Satellite data can be used to characterize the habitat and ecosystem properties that influence marine resources. There are two primary functions of ocean-colour in fisheries management; to monitor the environment providing a better understanding of ecosystem processes, and to locate populations of fish, increasing fishing efficiency. Additionally, ocean-colour data can be used to monitor a number of issues that impact fisheries, such as harmful algal blooms and coastal pollution.

v) Water quality

Management of water quality is the fundamental objective of several European initiatives (Robinson, 2008), developed to protect and maintain the marine environment. Products derived from satellite measurements of radiance can be used directly as water quality indicators; for example spectral light attenuation can be related to water clarity. Combining ocean colour data with numerical or statistical models generates an effective monitoring tool for operational management of the ocean.

vi) Hazards

Shelf seas are subject to a variety of oceanic hazards which occur from natural or man-made origin. These can have a significant impact on the marine ecosystem. Satellite measurements of ocean colour assist with the detection and monitoring of natural hazards such as harmful algal blooms. They can also be utilised to investigate the impact of extreme weather events such as hurricanes and storms. Man-made hazards such as oil spills may also be tracked using ocean colour data.

1.2.4b Limitations of ocean colour remote sensing

i) Cloud cover

One of the major limitations in the use of ocean colour remote sensing is its dependency on lack of cloud cover. Clouds reflect shortwave radiation back to space, preventing penetration of light within the visible domain. Therefore radiometry relies on a cloud free path between the ocean surface and orbiting satellite. Shelf seas surrounding the UK are commonly covered by cloud, meaning an average of 20-30 partially cloud free images are available for this region each year. As expected, cloud coverage is highly seasonal, with an increase found in winter months. During this period it is extremely difficult to obtain an approximately cloud free image of the Irish Sea. This is problematic for real time ocean management and also generates breaks in archived time series. This highlights the potential usefulness of assimilating remote sensing data into ecosystem models, where model outputs could effectively bridge data gaps. Generation of composite images can also compensate for lack of cloud free data. Composites are created by merging satellite images obtained over duration, producing a temporally and spatially averaged image. Some transient features may be lost during this process. Nevertheless composite images allow investigation of persistent biogeochemical patterns and trends.

ii) Atmospheric correction and adjacency effects

Only a small percentage of radiance detected at the top of atmosphere is emitted from the ocean, where approximately 90% originates from scattering by the atmosphere. Atmospheric correction procedures for ocean-colour data are required to evaluate what the ocean-colour signal would have been in the absence of an intervening atmosphere. Atmospheric effects must be removed from the reflectance signal by a series of correction procedures, which commonly rely on the assumption that there is no reflectance from the ocean in the near-infrared (NIR) regime. This assumption is not true in turbid, coastal regions, where backscattering is sufficiently high to generate reflectance at near-infrared wavelengths. Discrepancies due to non-zero NIR reflectance can be significant in highly turbid areas and as a consequence, reduce the quality of the radiometric measurement and subsequent ocean colour products. New methods are continuously being developed in an attempt to improve

atmospheric correction in shelf seas (Chami, 2007, Zhang et al., 2010 and Sanwlani et al., 2010).

Radiance from the ocean is significantly smaller in magnitude than radiance from the land. As a consequence, radiometric measurements obtained in coastal regions may be enhanced by stray light atmospherically scattered from the brighter adjacent land target. This process is known as the adjacency effect, and its occurrence prohibits the use of image pixels located adjacent to the coast (Liu, 2007). The system is further complicated by adjacency effects generated by clouds or by stray light within the optical sensor, as well as the sensor response time. This effect must be accounted for in accordance with atmospheric correction over coastal waters (Thome et al., 1998 and Santer et al., 2000).

iii) Algorithm performance in shelf seas

In a scheme proposed by Morel and Prieur (1977), oceanic waters can be separated into two categories depending on their optical properties, denoted as case 1 and case 2 types. Case 1 waters are waters in which the concentration of phytoplankton is high compared to non-biogenic particles. Here, optical properties of the water column are influenced predominantly by phytoplankton and its covarying biological material. The presence of additional substances such as CDOM and suspended minerals, forces classification into case 2, which is defined as everything else. These waters are optically more complex and IOPs are a consequence of independently varying constituents. Coastal shelf seas are commonly classified as case 2. Ratio algorithms developed for the retrieval of chlorophyll in case 1 regions often break down in those classified as case 2 due to the presence of other optically significant constituents (Gohin et al., 2002, Wang et al., 2003 and McKee et al., 2007a). For example, chlorophyll concentrations are overestimated in regions containing relatively high volumes of particulate matter. At these locations algorithms need to deconvolve the reflectance signal to generate independent estimates of each constituent. However varying combinations of substances may influence the optical signal in a similar manner, making it difficult to distinguish between materials. The problem may become simpler if the objective is to recover suspended mineral concentrations

without requiring accurate estimates of the other optically significant constituents. Accuracy of quantitative constituent retrievals can also be improved by incorporating field data to determine algorithm coefficients.

1.3 Choice of the Irish Sea as a test site

A potential link between ocean colour and water column hydrology was explored using the Irish Sea as a test site. This is a semi-enclosed shelf sea bordered by Britain and Ireland which covers approximately 58000 km^2, Figure 1.3. The maximum depth is 275m which corresponds to a deep water channel running through the centre from the Malin Sea in the north to the Celtic Sea in the south. Relatively shallow regions (< 50 m) are located east of the deep channel in the Eastern Irish Sea and Cardigan Bay. For the purpose of this study, the region of interest is extended south to include the Bristol Channel and the northerly territory of the Celtic Sea. Water circulates around the Irish Sea creating turbulence along coastal regions, with the main residual flow running south to north and an anti-clockwise circular flow dominating the eastern regions (Figure 1.4 c)). The primary forces responsible for movement of water in the region, and by implication the transport of suspended sediment, are tides, weather and density differences. The Irish Sea is a region of high tidal energy (Simpson and Hunter, 1974), with two entrances in the north and south allowing propagation of tides from the Atlantic Ocean. The amplitude of tidal velocity has significant spatial variability which determines many of the hydrodynamic features found in the region of interest. Maximum tidal currents (> 1.2 m s^{-1}) can be found at Anglesey, Wicklow Head and the Bristol Channel, whilst minimum values are located south west of the Isle of Man and in the eastern Irish Sea. There are two notable sea fronts, one to the north-west separating mixed waters of the Irish Sea with stratified regions in the north, and one in the south-west, separating the Irish Sea from warmer surface waters of the Celtic sea (Figure 1.4 b)). A permanent salinity front is also present in the eastern Irish Sea due to freshwater input from rivers located along the English coast. This area contains consistently lower values of salinity when compared to the remainder of the region of interest. The surface temperature in the Irish Sea ranges from 6ºC in the winter to 16ºC in the summer.

The Irish Sea is largely classified as a case 2 water type, meaning its optical properties are determined by at least three optically significant constituents in addition to seawater. Here you can find CHL, MSS and CDOM, with concentrations varying significantly over temporal and spatial frames. A measurement campaign consisting of several Irish Sea research cruises has provided statistical information on seawater composition in the region (see section 2.2). The average CHL (taken as a proxy for phytoplankton biomass) concentration measured in-situ was 1.08 mg m^{-3} with a standard deviation of 0.76 mg m^{-3}. CHL concentrations are generally lowest in the Irish Sea during winter months. Increased light in spring promotes phytoplankton reproduction generating raised levels of chlorophyll. This period displays maximum concentrations due to optimised conditions. The inverse pattern exists for MSS concentrations, where maximum and minimum values are observed in winter and summer months respectively. Three locations contain consistently high values of MSS, located in the Bristol Channel, Anglesey and Wicklow Head. These correspond to positions of maximum tidal energy. Mean values obtained for MSS and coloured dissolved organic matter (CDOM) were 5.16 g m^{-3} and 0.13 m^{-1} respectively with standard deviations of 5.74 g m^{-3} and 0.06 m^{-1}.

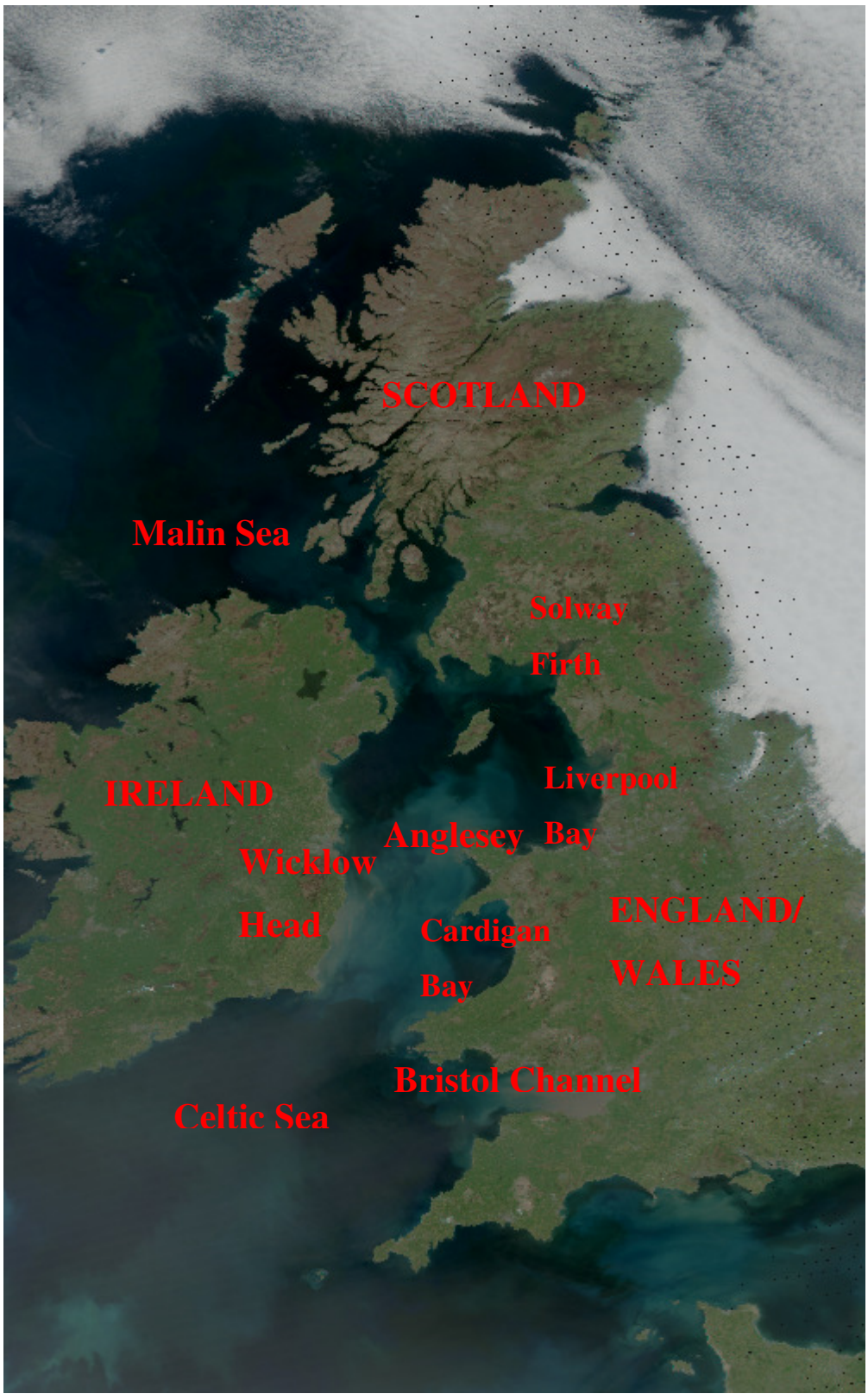

Figure 1.3 True colour image of the Irish Sea and north Celtic Sea showing locations of interest (image generated from MERIS reflectance data).

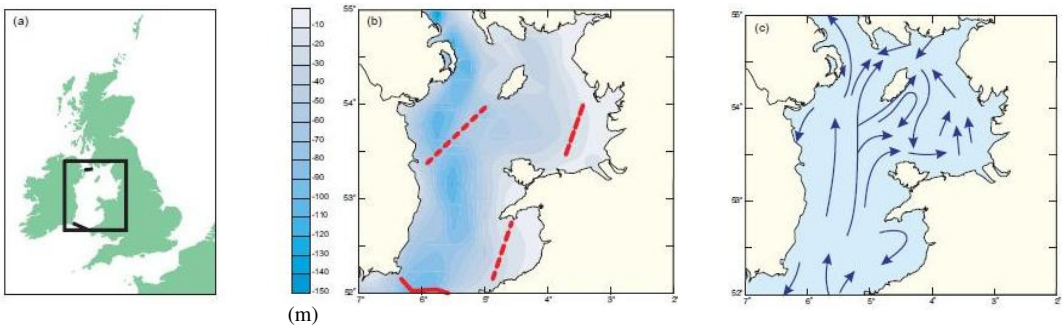

Figure 1.4 Physical characteristics of the Irish Sea a) map of Great Britain and Ireland showing boundaries of Irish Sea b) bathymetry of Irish Sea and front system indicated by red lines c) residual circulation of Irish Sea (Lees and Mackinson, 2007)

Significant research into the optical properties of this area have already been conducted, lead primarily by the School of Ocean Sciences at Bangor University, Wales and the Environmental Optics Group at the University of Strathclyde. There exist several locally tuned algorithms for the retrieval of constituent concentrations from the Irish Sea. Binding et al., (2003 and 2005), demonstrated the usefulness of reflectance measured as red wavelengths as a quantitative indicator of suspended sediment concentrations. It was shown that a single band algorithm, rather than variations in ocean colour ratios, was most effective for obtaining MSS in the Irish Sea. In the 2005 paper, it was hypothesised that errors in the retrieval were associated with changes of the mass-specific scattering coefficient for MSS. Deviations from a single value were used to explain variability in the in-situ data set. Potential origins of error in the MSS retrieval shall be discussed in detail in chapter 4. The effectiveness of reflectance measured at red wavelengths was also apparent in a paper published by McKee et al (2007a). In this example normalised water leaving radiance at 665 nm was used as a threshold for segregating optical water types into two classes before application of a chlorophyll retrieval algorithm. The performance of the standard OC4v4 chlorophyll algorithm could be greatly improved by considering individually, water types exhibiting low or high reflectance at 665 nm. Furthermore, optical water type classification is a useful way of understanding ambiguity in general algorithms. An alternative classification scheme will be discussed later in this study. Optical complexity is the primary limiting factor in

obtaining accurate estimates of biogeochemical products in shelf seas. For this reason, great effort has been applied to understanding the causes of uncertainty. Bowers et al. (1996) highlighted the effect of MSS on the recovery of chlorophyll from the Irish Sea. The presence of MSS decreased the sensitivity of the blue-green ratio to changes in chlorophyll, a result which was also determined previously by Brown and Simpson (1990). The use of sun induced chlorophyll fluorescence (SICF) for the derivation is also restricted by the presence of MSS. Using radiance transfer simulations, McKee et al (2007b), determined the degree to which MSS (and CDOM) reduced the SICF signal, suggesting caution should be applied when interpreting SICF from coastal seas.

It is clear that MSS contributes significantly to errors in the retrieval of optical products from shelf seas and a greater understanding of sediment dynamics may facilitate the inversion problem. This is the primary objective of this thesis. Previous work on sediment dynamics in the Irish Sea has been conducted by the Bangor School of Ocean Science. A link between tidal stirring, particularly during spring tides, and beam attenuation (which was used as an indicator of sediment concentration) was presented by Weeks et al. (1993). A seasonal signal was observed in the data with a reduction in beam attenuation from late May to September, however it was suggested this was not related to wind stirring. The study was continued by Bowers et al. (1998) over a longer time frame, with MSS concentrations estimated from satellite measurements of reflectance. Again, a seasonal cycle of reflectance was presented with maximum values occurring during winter months. Using a simple energy based model, it was shown that for regions of water depth between 40 and 80 m, an approximately linear relationship existed between tidal stirring and surface MSS concentrations. The hypothesis was extended to consider the available turbulent kinetic energy calculated from tides and wind (Bowers, 2003). The spatial distribution and seasonal variations of surface sediments could be explained generally in terms of available energy. However, lack of sufficient wind data generated discrepancies between model predictions and in-situ observations. Nonetheless, this is an interesting result and warrants further investigation. Locations of turbidity maxima found at Anglesey and Wicklow Head

are particularly difficult to replicate using numerical models. Patterns of sediment have been explained in terms of flocculation and disaggregation in high velocity zones (Ellis et al., 2004, Bowers et al., 2005, Ellis et al., 2008). Inward diffusion of larger flocculated particles from surrounding waters could continually maintain a turbidity maximum in the absence of a sediment source. However, validation of this hypothesis with in-situ field data is problematic due to increased tidal velocities at the relevant locations.

In more recent years, emphasis has been placed on understanding the effect of particle size on the radiometric signal. Satellite measurements of reflectance have been used to derive geographical distributions of suspended particle size in the Irish Sea (Bowers et al., 2007). Although, several assumptions were made in the derivation of the particle size theory, results were interestingly linked to the physical dynamics of the water column through use of the Kolmogorov length scale. This study was later extended by van der Lee et al. (2009). Bowers et al. (2009) demonstrated that variability in specific scattering by particles depends on changes in the apparent density of sediment (dry weight/'wet' volume) and mean size of the particles. This has implications in regions containing large percentages of flocculated particles where concentrations of MSS may be underestimated. Further investigation implied both particle absorption and scattering coefficients depend strongly on the particle cross sectional area (Bowers et al., 2011). It was suggested that reflectance in the red part of the spectrum is proportional to the cross sectional area of particles in suspension whilst reflectance measured at green/blue wavelengths depend also on diameter as particle absorption becomes more important. This result has major implications for satellite remote sensing in shelf seas and merits further investigation.

1.4 Thesis structure

It is clear that ocean colour remote sensing is a useful and essential part of modern oceanography, providing supplementary information to complement traditional measuring methods. However, significant work is required to develop ocean colour methods to operational standards. In light of the above, the following questions arise;

1. *Can methods of quantitatively interpreting satellite images in optically complex waters be developed?* This is the first stage of this study which focuses on the retrieval of MSS concentrations from optically complex seas. The relationships between reflectance measured remotely by satellite and concentration of MSS will be investigated using a combination of radiance transfer simulations and water sample analysis. Algorithms will be applied to satellite data to track spatial and temporal patterns of MSS in the region of interest.

2. *Given the existence of a significant archive of ocean colour images, is it possible to reconstruct temporal events from time series, even in areas such as the UK where there is high cloud cover?* To answer this question, a large database of Irish Sea satellite imagery is required. This will be constructed from available reflectance data measured by the MODIS Aqua (NASA) radiometer. Analysis of time series will provide information on temporal patterns of reflectance.

3. *Is it possible to use ocean colour radiometry to gain useful insights into physical processes in shelf seas beyond patterns of primary productivity?* Assigning MSS as a hydrodynamic tracer will provide useful insight into the mechanisms driving reflectance variability in the region. This will be investigated using a combination of individual reflectance images and established time series.

4. *Can it be demonstrated that surface reflectance signals are driven by processes deeper in the water column?* To understand the processes affecting

surface MSS concentrations, remote sensing data will be analysed in conjunction with physical dynamics derived from the POLCOMS hydrodynamic model. Physical parameters such as stratification and mixing, or bed shear stress, will be considered as drivers of reflectance variability. Derivation of relationships between surface reflectance and physical dynamics will provide information on the processes deeper in the water column affecting surface sediment patterns. Analysis of potential relationships will include detailed classification of geographical regions in which parameters are statistically linked.

5. *Furthermore, is it possible to infer directly from ocean colour, physical properties of the water column through development of simple algorithms?* As a final step, relationships between physical parameters and surface reflectance shall be investigated in detail to determine whether physical properties can be obtained directly from ocean colour. This will include a statistical classification of errors and potential uncertainties.

This thesis attempts to answers these important questions. The thesis has been written so that each results chapter is self-contained, containing the relevant methodology and theory specific to the study. Chapter 2 deals with standard methodology, which includes information on the relevant processing and manipulation of satellite images, as well as a detailed description of radiance transfer simulations and field observations used for algorithm development and validation. Chapter 3 focuses on the use of the POLCOMS hydrodynamic model and includes general methodology, a simple validation of model parameters and a theoretical description of secondary outputs used in this study. Chapters 4 to 7 contain the primary results of this study. Chapter 4 focuses on the derivation of a MSS retrieval algorithm, developed specifically for use in shelf seas. This forms the basis of chapter 5, which relies on the result that MSS can be monitored by interpretation of satellite imagery. Using reflectance as an indicator of surface sediment concentrations, time series of satellite data are utilised to investigate temporal and spatial patterns of reflectance in the Irish Sea. Statistical analysis of individual time

series allows classification of the region of interest into two dynamical areas containing low and high reflectance variance respectively. The low variance regime is then analysed in conjunction with POLCOMS stratification parameters (chapter 6), whilst high variance regimes are investigated in terms of available bed shear stress (chapter 7). The thesis concludes with a general conclusion, summarising the results from each chapter and proposing future work. Figure 1.5 shows a schematic diagram of the thesis structure.

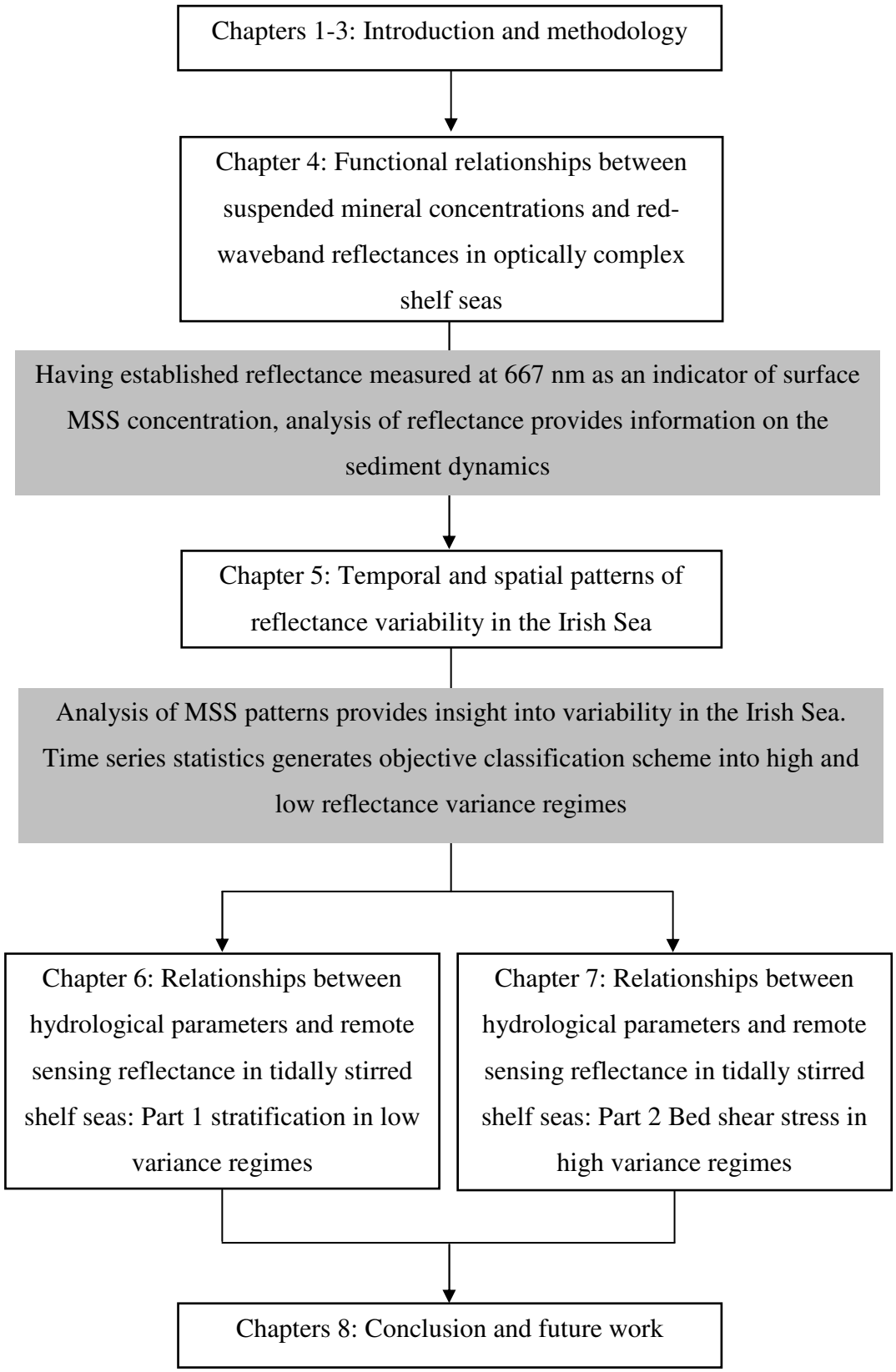

Figure 1.5 Schematic description of thesis structure.

References

Barnard, A.H., Zaneveld, J.R.V., Pegau, W.S., 1999. In situ determination of the remotely sensed reflectance and the absorption coefficient: closure and inversion. APPLIED OPTICS, 38 (24), 5108-5117.

Binding, C.E., Bowers, D.G., Mitchelson-Jacob, E.G., 2003. An algorithm for the retrieval of suspended sediment concentrations in the Irish Sea from SeaWiFS ocean colour satellite imagery. INTERNATIONAL JOURNAL OF REMOTE SENSING, 24 (19), 3791-3806.

Binding, C.E., Bowers, D.G., Mitchelson-Jacob, E.G., 2005. Estimating suspended sediment concentrations from ocean colour measurements in moderately turbid waters; the impact of variable particle scattering properties. REMOTE SENSING OF ENVIRONMENT, 94 (3), 373-383.

Borja, A, 2005. The European water framework directive: A challenge for nearshore, coastal and continental shelf research. CONTINENTAL SHELF RESEARCH, 25 (14), 1768-1783.

Bowers, D.G., Harker, G.E.L., Stephan, B., 1996. Absorption spectra of inorganic particles in the Irish Sea and their relevance to remote sensing of chlorophyll. INTERNATIONAL JOURNAL OF REMOTE SENSING, 17 (12), 2449-2460.

Bowers, D.G., Boudjelas, S., Marker, G.E.L., 1998. The distribution of fine suspended sediments in the surface waters of the Irish Sea and its relation to tidal stirring. INTERNATIONAL JOURNAL OF REMOTE SENSING, 19 (14), 2789-2805.

Bowers, D.G., 2003. A simple turbulent energy-based model of fine suspended sediments in the Irish Sea. CONTINENTAL SHELF RESEARCH, 23 (16), 1495-1505.

Bowers, D.G., Ellis, K.M., Jones, S.E., 2005. Isolated turbidity maxima in shelf seas. CONTINENTAL SHELF RESEARCH, 25 (9), 1071-1080.

Bowers, D.G., Binding, C.E., Ellis, K.M., 2007. Satellite remote sensing of the geographical distribution of suspended particle size in an energetic shelf sea. ESTUARINE COASTAL AND SHELF SCIENCE, 73 (3-4), 457-466.

Bowers, D.G., Braithwaite, K.M., Nimmo-Smith, W.A.M., Graham, G.W., 2009. Light scattering by particles suspended in the sea: The role of particle size and density. CONTINENTAL SHELF RESEARCH, 29 (14), 1748-1755.

Bowers, D.G., Braithwaite, K.M., Nimmo-Smith, W.A.M., Graham, G.W., 2011. The optical efficiency of flocs in shelf seas and estuaries. ESTUARINE COASTAL AND SHELF SCIENCE, 91 (3), 341-350.

Brown, J., Simpson, J.H., 1990. The radiometric determination of total pigment and seston and its potential use in shelf seas. ESTUARINE COASTAL AND SHELF SCIENCE, 31 (1), 1-9.

Chami, M., 2007. Importance of the polarization in the retrieval of oceanic constituents from the remote sensing reflectance. JOURNAL OF GEOPHYSICAL RESEARCH-OCEANS, 112 (C5), Art. No. C05026.

Dobrynin, M., Gayer, G., Pleskachevsky, A., Gunther, H., 2010. Effect of waves and currents on the dynamics and seasonal variations of suspended particulate matter in the North Sea. JOURNAL OF MARINE SYSTEMS, 82 (1-2), 1-20.

Ellis, K.M., Bowers, D.G., Jones, S.E., 2004. A study of the temporal variability in particle size in a high-energy regime. ESTUARINE COASTAL AND SHELF SCIENCE, 61 (2), 311-315.

Ellis, K.M., Binding, C.E., Bowers, D.G., Jones, S.E., Simpson, J.H., 2008. A model of turbidity maximum maintenance in the Irish Sea. ESTUARINE COASTAL AND SHELF SCIENCE, 76 (4), 765-774.

Falkowski, P.G., Raven, J.A., 1997. Aquatic Photosynthesis. Malden: Blackwell Science, 323-324.

Gohin, F., Druon, J.N., Lampert, L., 2002. A five channel chlorophyll concentration algorithm applied to SeaWiFS data processed by SeaDAS in coastal waters. INTERNATIONAL JOURNAL OF REMOTE SENSING, 23 (8), 1639-1661.

Gordon, H.R., 1997. Atmospheric correction of ocean color imagery in the Earth Observing System era. JOURNAL OF GEOPHYSICAL RESEARCH-ATMOSPHERES, 102 (D14), 17081-17106.

IOCCG (2000). Remote Sensing of Ocean Colour in Coastal, and Other Optically-Complex, Waters. Sathyendranath, S. (ed.), Reports of the International Ocean-Colour Coordinating Group, No. 3, IOCCG, Dartmouth, Canada.

IOCCG (2008). Why Ocean Colour? The Societal Benefits of Ocean-Colour Technology. Platt, T., Hoepffner, N., Stuart, V. and Brown, C. (eds.), Reports of the International Ocean-Colour Coordinating Group, No. 7, IOCCG, Dartmouth, Canada.

Ladner, S.D., Arnone, R.A., Gould, R.W., Weidermann, A.D., Haltrin,V.I., Lee, Z., Martinolich, P., Bergmann Ladner, T., 2002. Variability in the backscattering to scattering and f/Q ratios observed in natural waters. Proc. Ocean Optics XVI, Santa Fe, NM, 2002.

Lees, K. and Mackinson, S., 2007. An Ecopath model of the Irish Sea: ecosystems properties and sensitivity analysis. Sci. Ser. Tech Rep., Cefas Lowestoft, 138, 49pp.

Lee, Z., Carder, K.L., Du, K.P., 2004. Effects of molecular and particle scatterings on the model parameter for remote-sensing reflectance. APPLIED OPTICS, 43 (25). 4957-4964.

Liu, C.H., 2007. Error propagation from aerosol retrieval to atmospheric correction due to adjacency effect for FORMOSAT-2 RSI band. TERRESTRIAL ATMOSPHERIC AND OCEANIC SCIENCES, 18 (4), 827-841.

McKee, D., Cunningham, A., Dudek, A., 2007a. Optical water type discrimination and tuning remote sensing band-ratio algorithms: Application to retrieval of chlorophyll and K-d(490) in the Irish and Celtic Seas. ESTUARINE COASTAL AND SHELF SCIENCE, 73 (3-4), 827-834.

McKee, D., Cunningham, A., Wright, D., Hay, L., 2007b. Potential impacts of nonalgal materials on water-leaving Sun induced chlorophyll fluorescence signals in coastal waters. APPLIED OPTICS, 46 (31), 7720-7729.

Mobley, C.D., 1994. Light and Water: Radiative Transfer in Natural Waters. San Diego: Academic Press, 143.

Mobley, C.D., 1999. Estimation of the remote-sensing reflectance from above-surface measurements. APPLIED OPTICS, 38 (36), 7442-7455.

Morel, A., Prieur, L., 1977. Analysis of variations in ocean color. LIMNOLOGY AND OCEANOGRAPHY, 22 (4), 709-722.

Morel, A., Gentili, B., 1993. Diffuse-reflectance of oceanic waters. 2. Bidirectional aspects. APPLIED OPTICS, 32 (33), 6864-6879.

Morel, A., Antoine, D., Gentili, B., 2002. Bidirectional reflectance of oceanic waters: accounting for Raman emission and varying particle scattering phase function. APPLIED OPTICS, 41 (30), 6289-6306.

Robinson, I., 2008. Marine Board European Science Foundation Position Paper 12. Remote Sensing of Shelf Sea Ecosystem - State of the Art and Perspectives.

Ruddick, K.G., Ovidio, F., Rijkeboer, M., 2000. Atmospheric correction of SeaWiFS imagery for turbid coastal and inland waters. APPLIED OPTICS, 39 (6), 897-912.

Santer, R., Schmechtig, C., 2000. Adjacency effects on water surfaces: primary scattering approximation and sensitivity study. APPLIED OPTICS, 39 (3), 361-375.

Sanwlani, N., Chauhan, P., Navalgund, R.R., 2010. Atmospheric Correction Over Coastal Turbid Waters of Bay of Bengal Using OCEANSAT-I Ocean Colour Monitor (OCM) Data. JOURNAL OF THE INDIAN SOCIETY OF REMOTE SENSING, 38 (4), 617-626.

Sathyendranath, S., Cota, G., Stuart, V., Maass, H., Platt, T., 2001. Remote sensing of phytoplankton pigments: a comparison of empirical and theoretical approaches. INTERNATIONAL JOURNAL OF REMOTE SENSING, 22 (2-3), 249-273.

Schiller, H., Doerffer, R., 1999. Neural network for emulation of an inverse model - operational derivation of Case II water properties from MERIS data. INTERNATIONAL JOURNAL OF REMOTE SENSING, 20 (9), 1735-1746.

Simpson, J.H., Hunter, J.R., 1974. Fronts in the Irish Sea. NATURE, 250, 404 – 406.

Thome, K., Palluconi, F., Takashima, T., Masuda, K., 1998. Atmospheric correction of ASTER. IEEE TRANSACTIONS ON GEOSCIENCE AND REMOTE SENSING, 36 (4), 1199-1211.

van der Lee, E.M., Bowers, D.G., Kyte, E., 2009. Remote sensing of temporal and spatial patterns of suspended particle size in the Irish Sea in relation to the Kolmogorov microscale. CONTINENTAL SHELF RESEARCH, 29 (9), 1213-1225.

Vermote, E.F., El Saleous, N.Z., Justice, C.O., 2002. Atmospheric correction of MODIS data in the visible to middle infrared: first results. REMOTE SENSING OF ENVIRONMENT, 83 (1-2), 97-111.

Wang, J., Cota, G.F., 2003. Remote-sensing reflectance in the Beaufort and Chukchi seas: observations and models. APPLIED OPTICS, 42 (15), 2754-2765.

Weeks, A.R., Simpson, J.H., Bowers, D., 1993. The relationship between concentrations of suspended particulate matter and tidal processes in the Irish Sea. CONTINENTAL SHELF RESEARCH, 13 (12), 1325-1334.

Zaneveld, J.R.V., Twardowski, M.J., Barnard, A., and Lewis, M.R., 2005. Introduction to Radiative Transfer. Remote Sensing of Coastal Aquatic Envirmonments. Dodrecht: Springer, 1-20.

Zhang, Z.M., He, G.J., Wang, X.Q., 2010. A practical DOS model-based atmospheric correction algorithm. INTERNATIONAL JOURNAL OF REMOTE SENSING, 31 (11), 2837-2852.

Chapter 2

General methodology

Summary

This chapter is concerned with the methods involved in collecting and processing data used in the course of this work. The first section focuses on the use of satellite remote sensing data and includes information on processing and analysis techniques. There follows a description of in-situ field observations relevant to this study. These were utilised primarily for the derivation and validation of an ocean colour algorithm. The final section describes the implementation of radiance transfer calculations used to effectively model shelf sea radiance distributions.

2.1 Satellite remote sensing

Satellite remote sensing relies on the interpretation of visible and near-infrared radiation emitted from the surface of the ocean. For over three decades, satellites have played a crucial role in the monitoring and assessment of our seas. Various oceanic parameters can be measured, ranging from chlorophyll concentrations derived from radiometric observations, to estimates of sea surface height by active radar altimeters. The process of transmission of electromagnetic radiation through the atmosphere only allows several regions or "windows" in the visible, infrared and microwave wavelength bands to view the oceans (Sabins, 1978), as shown in Figure 2.1.

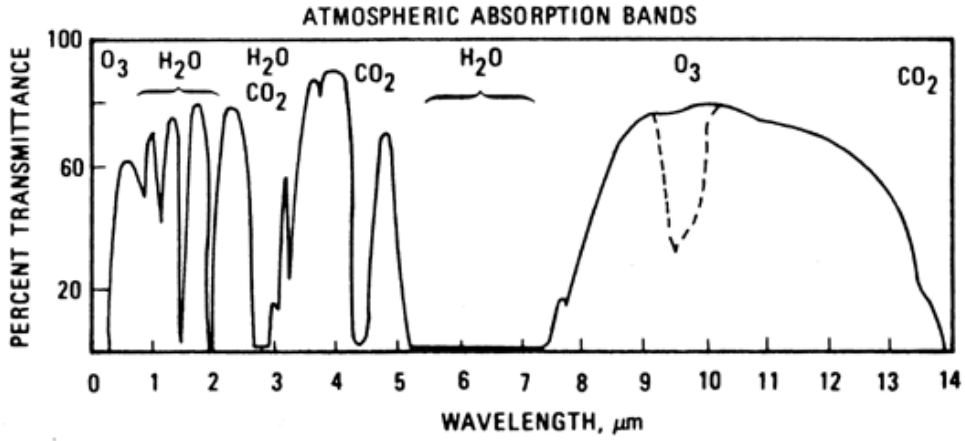

Figure 2.1 Atmospheric transmission as a function of wavelength within the electromagnetic spectrum employed for satellite oceanography (Sabins, 1978).

Radiation detected in visible wavelengths is used to monitor changes in the ocean colour. These wavelengths require cloud-free paths to propagate and can only be detected in daytime. Observations made in the infrared determine the blackbody radiation emitted from the ocean and are used to measure the sea surface temperature (Kilpatrick et al., 2001). These too require cloud-free paths to propagate but can be detected at night. Finally, microwaves can determine sea surface and atmospheric properties such as sea surface height, waves, wind vectors and amounts of water vapour (Nghiem et al., 1995). Microwaves have the added advantage that cloud cover appears transparent in this frequency domain, thus information can be retrieved during day or night.

This study concentrates primarily on the measurement of ocean colour, and more specifically, data collected by the MODIS and SeaWiFS radiometers (NASA). These instruments are mounted on polar-orbiting satellites, so named due to their approximate passing of the poles on each consecutive orbit. As the Earth rotates below them, the satellites capture a different part of the Earth's surface allowing near global coverage in 1 day. The sun-synchronous orbit path ensures time consistency of measurements, as the satellite passes the equator at the same time each day. The Moderate Resolution Imaging Spectroradiometer (MODIS), mounted on the Aqua (EOS-PM1) satellite platform, began operation in May 2002. At an orbiting altitude

of 705 km, MODIS uses a double-sided, continuously rotating scanning mirror which scans cross-track at ±55 degrees to produce 2330 km swaths with a spatial resolution of approximately 1000 m (increased resolution is available for 7 of the atmospheric/land bands). Radiance is reflected off either side of the scan mirror onto another mirror, which in turn reflects the beam to a fixed telescope that transmits the radiances to an optics bench where the spectrum is analysed. The instrument records 12 bit data and uses the received signal to create a 2-D image. Collected data spans 36 wavebands ranging from 405-14385 nm, meaning MODIS has the technical capability to measure temperature as well as colour. Wavebands are divided into job specific groups, shown in Table 2.1, of which 9 are reserved for ocean colour analysis (bands 8 – 16). In contrast, the Sea-viewing Wide-Field-of-view Sensor (SeaWiFS) mounted on Orb-View 2, has 8 wavebands (405-855 nm) designed specifically to investigate ocean colour. Orbiting at a similar altitude to MODIS, SeaWiFS generates data at 2 levels of resolution, 1.1 km Merged Local Area Coverage, MLAC, or 4.5 km Global Area Coverage, GAC (coverage limitations are explained later in this section). SeaWiFS was launched in 1997 and was the replacement for retired US sensor CZCS.

Table 2.1 MODIS band information

Band group	Bandwidth (nm)	Primary Use
1 – 2	620 - 876	Land/Cloud/Aerosols Boundaries
3 – 7	459 - 2155	Land/Cloud/Aerosols Properties
8 – 16	405 - 877	Ocean Colour/ Phytoplankton/ Biogeochemistry
17 – 19	890 - 965	Atmospheric Water Vapour
20 – 23	3660 - 4080	Surface/Cloud Temperature
24 – 25	4433 – 4599	Atmospheric Temperature
26 – 28	1360 – 7475	Cirrus Clouds Water Vapour
29	8400 – 8700	Cloud Properties
30	9580 – 9880	Ozone
31 – 32	10780 – 12270	Surface/Cloud Temperature
33 – 36	13185 – 14385	Cloud Top Altitude

2.1.1 Data processing

MODIS and SeaWiFS satellite data are distributed by NASA (http://oceancolor.gsfc.nasa.gov/) via the Goddard Space Flight Centre Ocean Biology Processing Group (OBPG). Data is free and easily accessible by means of an interactive web-based portal operated by Ocean Color Web (user registration is required for SeaWiFS access). There are three sampling formats, Local Area Coverage, LAC, Global Area Coverage, GAC, and Merged Local Area Coverage, MLAC. GAC data are subsampled and recorded onboard the spacecraft and subsequently downloaded twice a day at NASA/Goddard. These data have effective resolutions of approximately 4.5 km along the centre of the swath. LAC data are recorded at 1.1 km resolution and broadcast to High Resolution Picture Transmission (HRPT) sites operating as ground-receiving stations, as well as downloaded at Goddard. MLAC data contain all available HRPT and LAC files consolidated for a given orbit. In case of HRPT overlap, quality tests are applied to ensure only the best quality scans are stored. SeaWiFS generates data in MLAC and GAC sampling format, although contract restrictions limit the time period of available MLAC to December 2004. MODIS data is available for LAC from the date of first operation until present.

OBPG have developed the SeaWiFS Data Analysis System (SeaDAS), a software package that, used in conjunction with the NASA funded Ocean Color project, allows users to download, process and analyse their own remote sensing data. The software is available free of charge (downloadable from Ocean Color Web), and is fully supported by the group. It consists of a series of FORTRAN and IDL program codes which can be used to process the acquired satellite data through the relevant processing stages. It offers an extensive range of tools and features to assist the user with data analysis and visualisation. Data can be extracted and output from SeaDAS in several formats, including *png, ASCII* and *binary* files. (As MODIS and SeaWiFS data processing follows similar procedural steps, this report shall focus on the processing of MODIS data only to avoid repetition).

The lowest level of data, Level 0, is that which is recorded onboard the spacecraft. These are the raw radiance counts collected by the radiometer. The first processing stage simply incorporates navigation and calibration data with the raw radiance values, giving Level 1A data. Next, a geolocation file is created with corresponding attitude and ephemeris data. The combination of geolocation and Level 1A files are required to generate Level 1B data, where the pixels are now geolocated. Quality flags and error estimates are also available at this stage. Atmospheric corrections are applied to produce the Level 2 file. Empirical algorithms are then applied to the raw radiance counts to calculate geophysical properties. The Level 2 product corresponds exactly in geographical coverage (scan-line and pixel extent) to that of its parent Level 1A product and is stored in one physical HDF file. Ancillary Meteorological (MET) and Optimum Interpolation Sea Surface Temperature (OISST) data can be manually acquired to ensure accurate processing during atmospheric correction stages. A schematic of the processing steps for MODIS data and corresponding SeaDAS program code is shown in Figure 2.2.

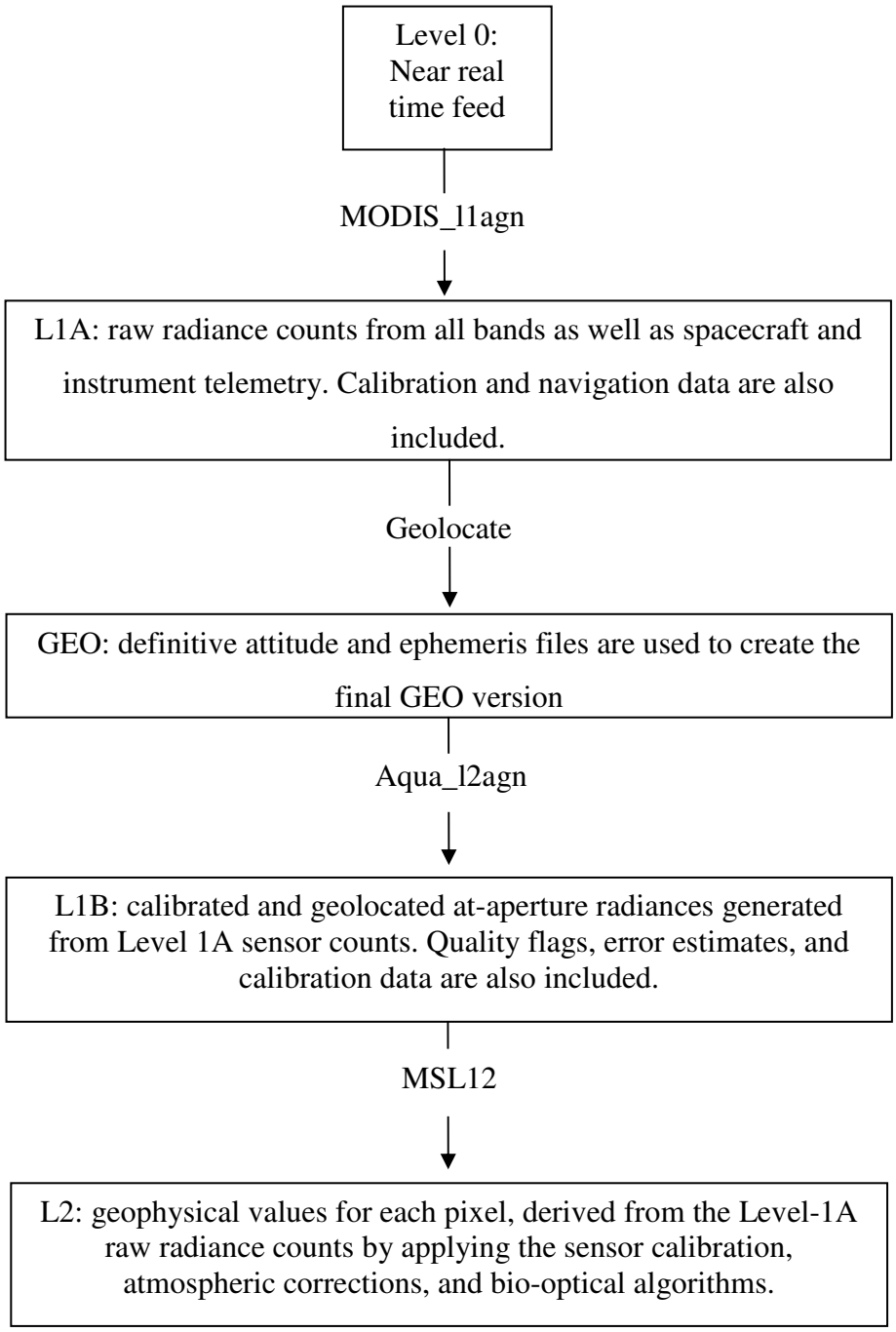

Figure 2.2 Schematic of MODIS processing stages. The figure contains the names of the SeaDAS program implemented code at each step and a description of how the data is affected.

2.1.2 Atmospheric correction

The radiance signal detected by the satellite consists of an oceanic and atmospheric component. Whilst the ocean element contributes approximately 10% of the total signal, atmospheric and surface scattering effects are removed by application of an atmospheric correction (Bailey et al., 2010). The total wavelength dependent reflectance, ρ_t, measured at the top of the atmosphere is given by;

$$\rho_t = \rho_r + (\rho_a + \rho_{ra}) + t\rho_{wc} + t\rho_g + t\rho_w \quad (2.1)$$

The purpose of atmospheric correction is to retrieve the water leaving reflectance, ρ_w from the above equation. The terms, ρ_g and ρ_{wc}, account for the addition of reflectance due to ocean surface effects. Sunglint, ρ_g, is the photons reflected from the rough ocean surface and ρ_{wc} is included where white caps are present. Both terms are estimated from wind vectors and removed from the top-of-atmosphere measurements. Diffuse transmittance, t, is a function of Rayleigh and ozone optical thickness. The remaining components of ρ_t are the result of atmospheric scattering. Reflectance introduced by molecular scattering (Rayleigh scattering), ρ_r, can be accurately modelled and subtracted from the total reflectance value. The final two terms, ρ_a and ρ_{ra} are defined as reflectance due to aerosol and molecular-aerosol interactions. To resolve the aerosol contributions, the concentrations and optical properties of the aerosol are required throughout the image. These are estimated in the NIR and extrapolated to visible wavelengths using an aerosol model. Assumptions made at this stage of the atmospheric correction process introduce errors when deriving reflectance in coastal regions.

2.1.3 Level 2 products

The standard Ocean Colour product contains 12 geophysical values derived for each pixel: six water-leaving radiances for bands 1 to 6, the chlorophyll a concentration, the diffuse attenuation coefficient at band 3, the epsilon value for the aerosol correction of bands 7 and 8, the angstrom coefficient for bands 4 and 8, and the aerosol optical thickness at band 8. Additionally, the standard Sea Surface Temperature (SST) product contains 11-micron and 4-micron (night time only) SST

for each pixel. There is also a flag product which contains 32 flags developed to report any failures or warnings that may be associated with a specific pixel. In the region of interest, consistent flags include the turbid water and coccolithophore flags. In addition to the standard ocean colour and SST products, a series of non-standard parameters are available.

Products available to view and analyse include;

- R_{rs}*_nnn* – Remote sensing reflectance at 412 nm, 443 nm, 488 nm, 531 nm, 551 nm, 667 nm, 678 nm, 748 nm, 869 nm (mW cm^{-2} μm^{-1} sr^{-1}). Sea surface reflectance defined as the ratio of water-leaving radiance to surface irradiance.
- *AOT* – Aerosol optical thickness (dimensionless). This is a by product of the atmospheric correction. As aerosols absorb and scatter, they directly affect the radiation reflected to space, and the aerosol optical thickness is a measure of the aerosols and how the transmitted light is affected by them.
- *Cdom_index* – CDOM index determines the proportion of Chlorophyll-chromophoric dissolved organic matter (CDOM) by considering simultaneously the relationship between chlorophyll and CDOM dependent reflectance ratios (Morel & Gentili, 2009).
- *Kd_490* – Downwelling diffuse attenuation coefficient at 490 nm (m^{-1}). This describes the turbidity of the water column. It is directly connected to the scattering and absorption coefficients of a medium and describes how blue/green wavelength radiation penetrates the water. The algorithm employs the ratio of normalised water leaving radiance measured at 443 and 551 nm to determine Kd_490.
- *L2_flags* – Flags stored for processing warnings.
- *PAR* – Photosynthetically available radiation from 400 – 700 nm. This is the spectral range of solar radiation that photosynthetic organisms are able to use in the process of photosynthesis.
- *PIC*/POC – Particulate inorganic concentration and particulate organic concentration respectively.
- *Angstrom_exponent* – Angstrom exponent for aerosol model.

- *Chlor_a* – Chlorophyll *a* concentration (mg m^{-3}). This provides the concentration of chlorophyll a which is used to assess phytoplankton concentration.
- *SST* – Sea surface temperature (degrees C). Provides information on the temperature of the surface. Values determined by algorithm utilising 11μm and 12μm channels.
- *SST4* – As above using 3 and 4 micron channels. SST4 is often used to determine night time SST as the short-wave infrared bands near 4μm are affected by bright reflective sources such as sun glint.

2.1.4 Standard algorithms

i) Chlorophyll a concentration

Chlorophyll a is the photosynthetic pigment, found in all phytoplankton species, which is a measure of concentrations of phytoplankton in the ocean. Phytoplankton mostly absorbs light in the blue and red wavelength regions and scatters light predominantly of green wavelengths, giving it a green appearance. Because of this, standard algorithms used to estimate chlorophyll *a* concentrations rely on ratios between the radiance of blue and green light reflected by the sea. The OC3 algorithm, employed by MODIS-A, uses the greatest (>) of the $R_{rs}(443)/R_{rs}(551)$, and $R_{rs}(488)/R_{rs}(551)$ ratios (O'Reilly et al., 1998);

$$c_a = 10.0^{\left(0.2830 - 2.753 R_{3M} + 1.457 R_{3M}^2 + 0.659 R_{3M}^3 - 1.403 R_{3M}^4\right)} \quad (2.2)$$

where $R_{3M} = \log_{10}\left(R_{550}^{443} > R_{550}^{490}\right)$, and R_B^A is $R_{rs}(A)/R_{rs}(B)$. (2.3)

Studies into the accuracy of chlorophyll a algorithms have shown that in case 1 waters, they produce good results (O'Reilly *et al*., 1998). However in case 2 waters, which are more optically complex, the standard algorithms perform poorly, overestimating concentrations of chlorophyll a (Gohin et al., 2002 and McKee et al., 2007).

ii) Sea Surface Temperature (SST)

In satellite radiometry, Sea Surface Temperature (SST) refers to the temperature of a thin layer on the surface of the ocean (~10μm) known as the skin. The SST algorithm utilises MODIS bands 31 and 32 at 11 and 12 μm respectively. Brightness temperatures are derived from the observed radiances by inversion (in linear space) of the radiance versus blackbody temperature relationship. The nonlinear SST algorithm (Kilpatrick et al., 2001) is tuned for two different regimes based on brightness temperature difference. The algorithm for computing SST from observed brightness temperatures BT_{11} and BT_{12} (brightness temperature in deg-C at 11 μm and 12 μm respectively) is shown below, where $dBT = BT_{11} - BT_{12}$.

For $dBT <= 0.5$

$$sst = a_{00} + (a_{01} \times BT_{11}) + (a_{02} \times dBT \times b_{sst}) + (a_{03} \times dBT \times [1/(\mu - 1)]) \quad (2.4)$$

For $dBT >= 0.9$

$$sst = a_{10} + (a_{11} \times BT_{11}) + (a_{12} \times dBT \times b_{sst}) + (a_{13} \times dBT \times [1/(\mu - 1)]) \quad (2.5)$$

For $0.5 < dBT < 0.9$

$$sstlo = a_{00} + (a_{01} \times BT_{11}) + (a_{02} \times dBT \times b_{sst}) + (a_{03} \times dBT \times [1/(\mu - 1)]) \quad (2.6)$$

$$ssthi = a_{10} + (a_{11} \times BT_{11}) + (a_{12} \times dBT \times b_{sst}) + (a_{13} \times dBT \times [1/(\mu - 1)]) \quad (2.7)$$

$$sst = sstlo + \frac{(dBT - 0.5)}{0.9 - 0.5} + (ssthi - sstlo) \quad (2.8)$$

where b_{sst} is the baseline SST taken from OISST and μ is the cosine of sensor zenith angle. Coefficients a_{00} to a_{13} are temporally variable and are obtained from look up tables. Validation of the SST product suggests a measurement accuracy of better than 1 K (Marcello et al., 2004, Minnett et al., 2002).

2.1.5 Validation of R_{rs} measurements

The accuracy of the retrieved standard ocean colour product is of variable quality. In particular, estimates generated in shelf seas often fall short of the ± 35 % pre-launch error objective (McClain et al., 1992). Fundamentally, the performance of any ocean colour algorithm relies on the accuracy of the reflectance measurement. R_{rs} values are validated using coincidentally measured in situ observations. Well defined match-up criteria are in place to encourage validation with suitable in situ data. These criteria restrict comparisons to field observations measured within 3 hours of the satellite pass. In situ stations must be separated by 12 km and duplicate casts are confined to the spectra containing the greatest value of nLw490. For the satellite image, the number of non-land pixels must be greater than 50% of the total. Field measurements can be obtained from various databases, developed to assist users with satellite validation (i.e. NASA SeaBASS (http://seabass.gsfc.nasa.gov/), ESA Mermaid, (http://calvalportal.ceos.org/cvp/web/guest/mvt)). Even with these facilities, suitable match ups are difficult to obtain in the Irish Sea due to the high volume of cloud cover. A time series of cloud cover fraction, Figure 2.3, calculated for over 1000 images of the Irish Sea demonstrates the restriction of potential data due to cloud cover. One tenth of the images contain less than 50% cloud cover, whilst 70% have lost all useful pixel information due to cloud masking. Similarly, Figure 2.4 displays the number of cloud free pixels available in the Irish Sea in 2007 on a pixel by pixel basis. The lack of suitable satellite imagery makes in situ based validation challenging. Of 158 measurement stations in the Irish Sea and Bristol Channel obtained during research cruises conducted by Strathclyde University (see section 2.2), 5 are consistent with the match-up protocol. Validation of MODIS R_{rs} measurements obtained from these locations is shown in Figure 2.5. Satellite data has been averaged over a 5x5 pixel area centred on the station latitude / longitude coordinate. The solid line depicts the 1:1 line and dashed lines depict the 5% pre-

launch error objective for radiance values. Good agreement between satellite and field radiometric measurements can be seen at stations 5, 6 and 9. Results for station 10, which contains the greatest residual difference and lowest corresponding time discrepancy, suggests in some part, anomalies are independent of time. Therefore, a relaxed version of the match-up protocol may yield more valid comparisons.

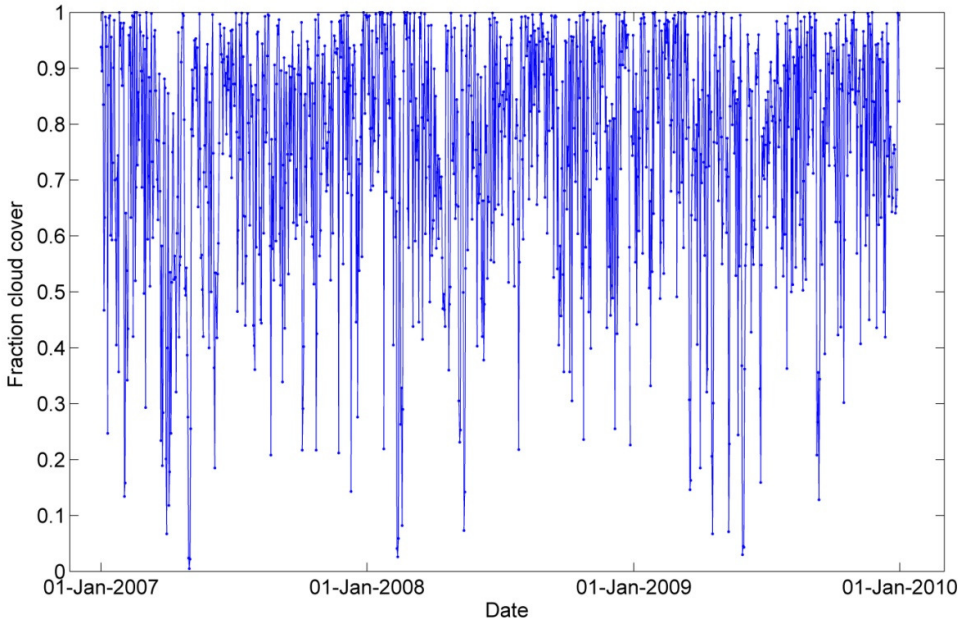

Figure 2.3 Cloud cover fraction for Irish Sea images, taken 01 January 2007 to 01 January 2010. Only a small fraction of images contain sufficient pixel information to effectively validate satellite measurements. Data courtesy of GES DISC via Giovanni web portal (http://disc.sci.gsfc.nasa.gov/giovanni).

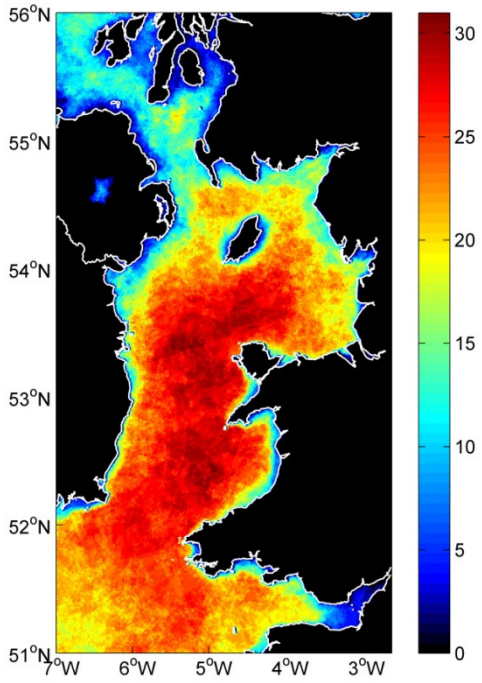

Figure 2.4 Number of cloud free pixels available in the MODIS Aqua dataset for the year 2007.

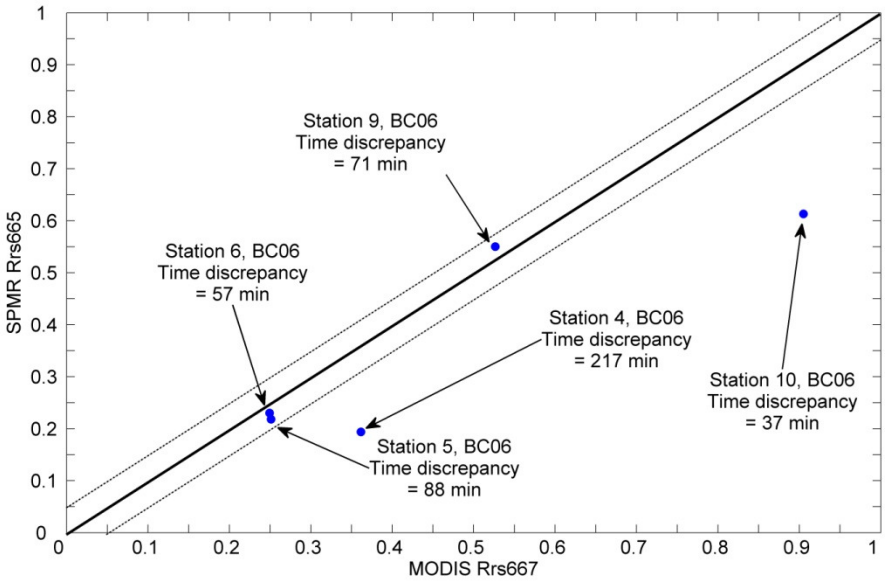

Figure 2.5 Validation of MODIS R_{rs} 667 using field observations. The solid 1:1 represents an exact match between radiometric instrumentation measurements. Dashed lines depict the pre-launch objective error of 5% for radiance measurements. The residual difference is independent of time.

Satellite data were processed using SeaDAS version 6.1. All images were map projected onto a 2-dimensional Mercator grid to ensure geographical consistency of pixels. Analysis was conducted using Matlab software, in particular the image processing toolbox and University of Columbia Earth Observation Sciences M_Map freeware mapping toolbox for Matlab (http://www.eos.ubc.ca/~rich/map.html). A list of scripts and functions written specifically for this project can be found in Table 2.2 (relevant scripts may be available on request).

Table 2.2 Matlab scripts relevant to satellite remote sensing.

Name	Description
allatonce	Imports and cleans satellite reflectance data.
blotch_data	Allows sub-selection of satellite image.
create_composite	Generates composites of satellite images.
descriptors	Classifies reflectance data by relevant descriptor.
imagesat	Creates satellite image
mss_calc	Calculates upper and lower limits of MSS algorithm
plot_ts_grid	Plots time series data
POLsat	Projects POL data and satellite data onto consistent corrdinates
select_points_scat	Allows selection of data from scatterplot and displays geographical location of pixels on map
time_series_grid/selection	Generates time series from gridded satellite data
time_series_class	Determines classification group for time series data
transectplots	Allows selection and generates of transects

2.2 Field observations

A common practice in the field of environmental optics is the participation in research cruises. This involves going to sea and measuring various oceanic parameters in situ. Data collected in this manner are often considered to be "truth" values, to which modelled and remotely acquired data are compared. Field observations used in this study were collected on 6 research cruises in the Irish Sea and Bristol Channel, spanning the period August 2001 to August 2006. Measurements were conducted at the stations illustrated in Figure 2.6.

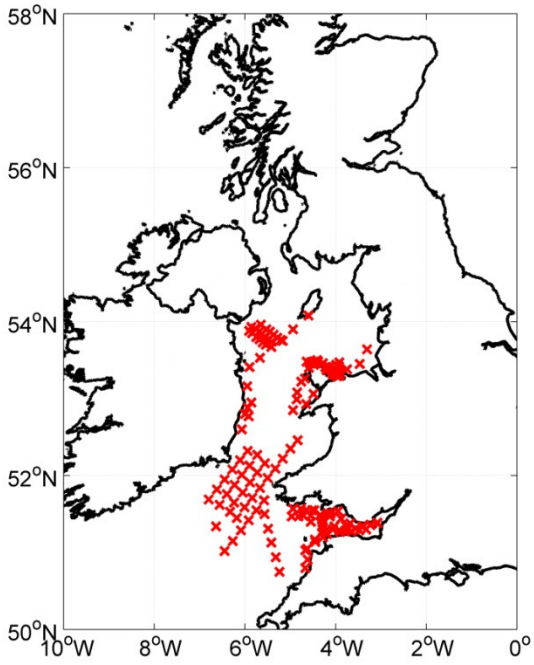

Figure 2.6 Station locations from 6 Irish Sea and Bristol Channel cruises.

The purpose of an optics research cruise is to obtain information on the inherent and apparent optical properties of the water. To do this, marine instrumentation is deployed to monitor how light interacts with the water column. This coincides with the collection of corresponding in-water constituent concentrations. There are three main categories of instrument which differ in practical use. Stand alone radiometers (e.g., RAMSES), which are placed statically on a ship or floatation device, collect upwelling and downwelling distributions of light. Profilers (e.g., SeaWiFS Profiling Multichannel Radiometer, SPMR) measure small scale changes in the underwater

light field as a function of depth. More modern instrumentation can be based on Autonomous Underwater Vehicles, which independently gather information across large areas. This study focuses on data gathered by 3 profiling instruments, a Satlantic freefalling SPMR, WETLabs ac-9 Absorption and Attenuation Meter and HOBI Labs HydroScat-2 Backscattering Sensor. The Satlantic SPMR is discussed in greater detail than the other instruments as it provides the data required for validation purposes.

2.2.1 Satlantic SeaWiFS Profiling Multichannel Radiometer

The Satlantic (Satlantic Inc., Nova Scotia, Canada) SeaWiFS Profiling Multichannel Radiometer (SPMR) is a multispectral instrument designed specifically for the purposes of SeaWiFS validation. It generates measurements of upwelling radiance, L_u, and downwelling irradiance, E_d, across the visible spectrum (412, 443, 489, 510, 554, 665 and 700 nm), with associated bandwidths of 10 nm. Designed as a freefalling profiler, the SPMR instrument decouples the measurements from ship motion and minimises light interference, such as ship shadowing.

Data collected by the SPMR are processed using the Satlantic ProSoft version 7.7 data analysis package (ProSoft 7.7 User Manual, 2009). Essentially, the program converts raw signals detected by the instrument into higher level products such as water leaving radiance and reflectance profiles. At the first level (1a/1b/2), calibration and reference data are subtracted from the collected signal. Any measured points greater than 10 times the cast standard deviation are removed, as well as points where the tilt of the instrument was greater than a defined value (10 degrees). Processing to level 2s involves defining a pressure coordinate system. The E_d and L_u sensors, located at the top and bottom of the instrument respectively, are separated on the SPMR by a distance of 1.4 m. The measurements per depth are corrected to a common depth defined by the E_d sensor. To progress to level 3, the data is wavelength interpolated and sorted into depth-averaged bins of 0.5 m. Optical sensor data (L_u etc.) are natural log transformed to "straighten" the data prior to averaging. The final stage incorporates radiometric equations to calculate level 4 products. A linear polynomial fit is applied to the initial 5 points of depth profiles lnL_u and lnE_d.

The exponential of the polynomial coefficients are used to derive *K* and sub-surface values, $L_u(0^-,\lambda)$ and $E_d(0^-,\lambda)$, *K* being obtained from the gradient and sub-surface values estimated from the intercept. Accounting for air-sea interface effects, L_u and E_d are extrapolated through the surface to give $L_w(0^+,\lambda)$ and $E_d(0^+,\lambda)$;

$$L_W\left(0^+,\lambda\right)=L_u\left(0^-,\lambda\right)\frac{1-\rho(\lambda,\theta)}{\eta_w^2(\lambda)} \tag{2.9}$$

$$E_d\left(0^+,\lambda\right)=E_d\left(0^-,\lambda\right)/1-\alpha \tag{2.10}$$

where $\rho(\lambda,\theta)$ is the Fresnel reflectance index for water (0.021 for seawater), $\eta_w(\lambda)$ is the Fresnel refractive index of seawater (1.345) and α is the Fresnel reflection albedo for irradiance from sun and sky (0.043). The above-surface values of radiance and radiance then provide inputs for calculating radiometric quantities, for example remote sensing reflectance;

$$R_{rs}\left(0^+,\lambda\right)=\frac{L_W\left(0^+,\lambda\right)}{E_d\left(0^+,\lambda\right)} \tag{2.11}$$

During the course of ProSoft data processing (version 7.7.11), an error was uncovered with the procedure responsible for extrapolating optical values to the surface. The first two quantities of L_u profiles derived at level 3 were marginally lower than those presented in the level 2s data. An example of this is shown in Figure 2.7. The error was found to be consistent across all wavelengths and was only present for the L_u sensor.

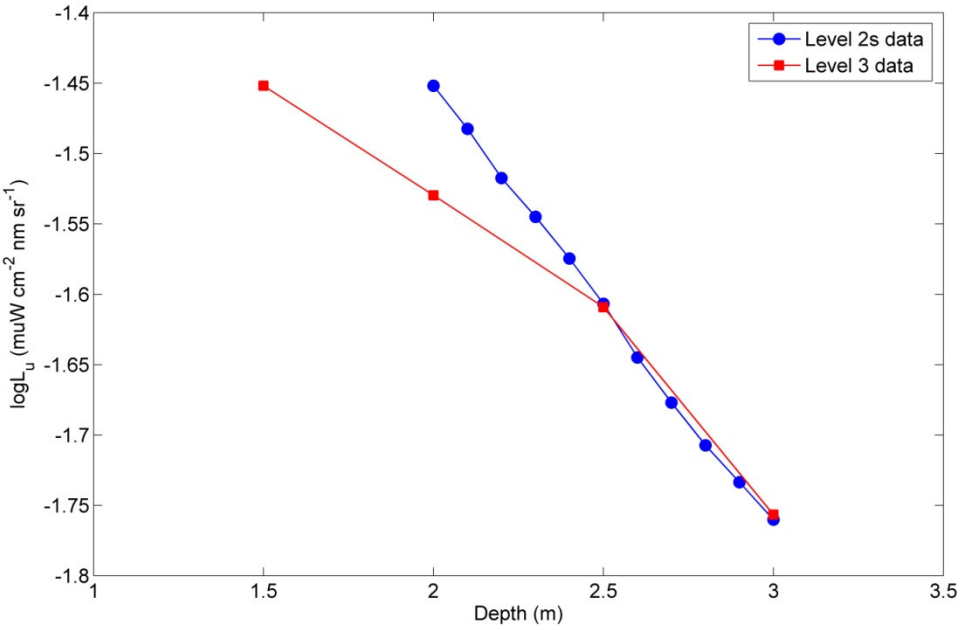

Figure 2.7 Errors in first two points of level 3 depth-averaged L_u values.

The binning algorithm used by ProSoft was determined as the cause of the error, whereby the program was unable to effectively deal with NaN values. Spatial differences between the SPMR L_u and E_d sensors prevent L_u measurements in the top several metres of the profile. These "blank" data points were subsequently being replaced by NaNs which were included in the depth-average binning. A correction routine was developed to address this issue, which ignored the first two data points when performing extrapolations on L_u. Figure 2.8 details the statistical difference between corrected and uncorrected surface R_{rs} values as a function of wavelength. The box plot has lines at the lower quartile, median, and upper quartile values. Whiskers extend from each end of the box to the most extreme values within 1.5 times the inner quartile range. Outliers, displayed as blue dots, are data with values beyond the ends of the whiskers. The results suggest uncorrected SPMR data were underestimating surface R_{rs}. In some cases, the percentage difference between corrected and uncorrected data was greater than 150%. $R_{rs}665$ had the greatest anomaly with a 39% median difference. Minor differences in L_u translate into significant errors in the recovered R_{rs} spectrum, as shown in Figure 2.8.

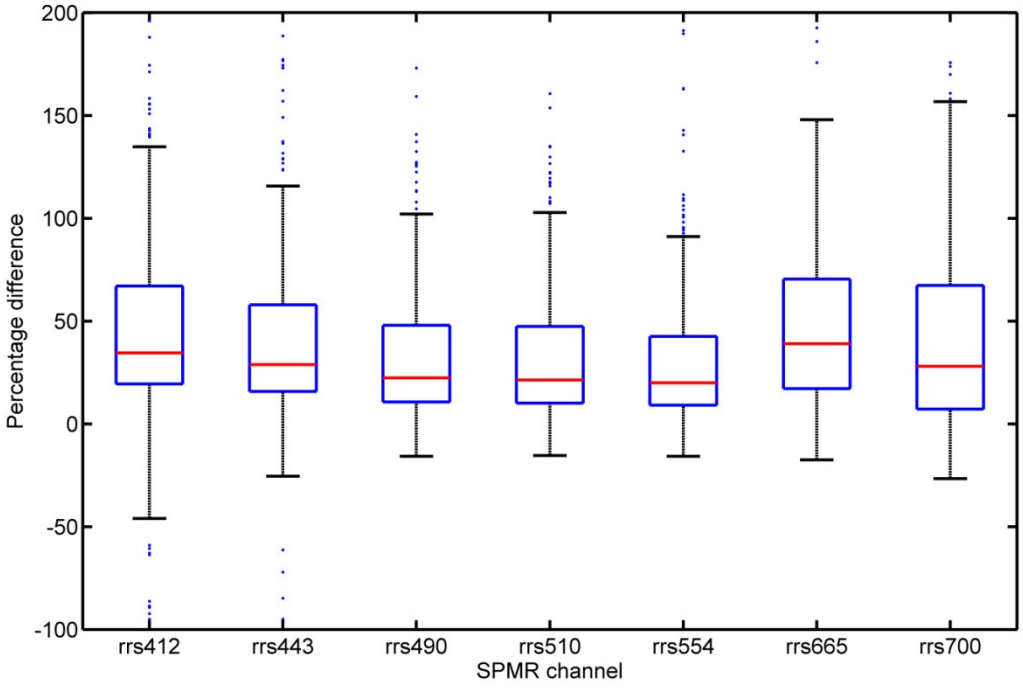

Figure 2.8 Statistics of percentage difference between corrected and uncorrected SPMR data. The variable median values range from 20% to 39%, however maximum differences of greater than 150% were recorded. This highlights the effect of a small underestimation of L_u.

2.2.2 ac-9 Absorption and Attenuation Meter

The dual-path ac-9 Absorption and Attenuation Meter (WETLabs ac-9 plus User's Guide, 2008), measures in situ inherent optical properties of particulate and dissolved material at nine wavelengths across the visible and NIR spectrum (412, 440, 488, 510, 532, 555, 650, 676 and 715 nm). The instrument contains two incandescent light sources, which are transmitted through separate enclosed volumes of sample water. The internal wall of the flow tube used for attenuation measurements is black to encourage absorption of photons scattered out of the transmitted beam. This excludes the detection of scattered light by the housed lens. For absorption measurements, a reflective flow tube reflects forward scattered photons back into the transmitted beam, ensuring an optimal contribution to the intensity measurement. Software provided by WETLabs converts the transmitted irradiance into attenuation, $c(\lambda)$, and

absorption, $a(\lambda)$, coefficients. The non-water scattering coefficient, $b(\lambda)$, is obtained using the expression $b_n(\lambda) = c_n(\lambda) - a_n(\lambda)$.

2.2.3 HydroScat-2 Backscattering Sensor

The HydroScat-2 Backscattering Sensor (hs-2) is an optical instrument developed to generate measurements of total backscattering $b_b(\lambda)$ at 2 wavelengths, 470 nm and 676 nm, as well as simultaneous measurements of chlorophyll fluorescence at 676 nm (HOBI Labs User's Manual, 2008). It consists of 2 independent channels, each containing frequency modulated LED light sources and an optical receiver. Light emitted by the wavelength specific LED penetrates the water sample at 20^o from the normal. A prism contained within the optical receiver bends the detection field-of-view towards the source beam. Unwanted light is excluded by means of a band-pass interference filter and the remaining photons are focused on a silicon detector. The volume scattering function at 140° is estimated from the irradiance detected by the hs-2, and the backscattering coefficient is subsequently estimated using the method of Maffione & Dana (1997). The configuration of the two channels provides the secondary capability of measuring chlorophyll fluorescence by excitation from the shorter wavelength source.

2.2.4 Specific inherent optical properties (SIOP)

The absorption coefficients and spectral slope for *CDOM* were determined by filtering seawater samples through a 0.2 μm membrane filter and measuring the optical density of the filtrate in a 10 cm pathlength cuvette. Absorption coefficients for suspended particles were determined by filtering 500 ml of seawater through 25mm diameter Whatman GF/F filters and measuring the optical density of these filters before and after extraction of pigments with acetone. Subtraction of the two optical density spectra allowed the contributions of phytoplankton pigments and non-algal particulates to be determined. Filter pad optical densities were converted to absorption coefficients for phytoplankton (a_p) and non-algal particulates (a_{nap}) using a pathlength amplification factor of 1.7: this was established empirically by comparing total absorption coefficients estimated from the sum of the particulate and dissolved components with those measured in situ using the ac-9. Since suspended

mineral particles in the Irish Sea are strongly coloured, it was assumed that a_{nap} was effectively a_{mss}. Specific absorption coefficients were then derived by linear regression of absorption coefficients on the relevant variable concentrations to give a^*_{CHL}, a^*_{MSS} and a^*_{CDOM} (Brown, 2010). Scattering and backscattering coefficients were partitioned between algal and non-algal particles using multiple linear regression (Stavn & Richter 2008). Reconstructions of total inherent optical properties for waters dominated by minerals and chlorophyll using specific inherent optical derived by the procedures described above generated reasonably representative values (McKee & Cunningham 2006). SIOP values are shown in Table 2.3. All Matlab scripts relevant to this section are found in Table 2.4 (scripts available on request).

Table 2.3 Specific inherent optical properties used in radiance transfer modelling. Wavelengths correspond to specific MODIS channels.

Waveband	*a*CHL*	*a*MSS*	*a*CDOM*	*b*CHL*	*b*MSS*	*bb*CHL*	*bb*MSS*
412	0.029	0.071	1.562	0.052	0.475	0.001	0.015
443	0.029	0.056	0.970	0.047	0.479	0.001	0.014
488	0.021	0.039	0.517	0.055	0.488	0.001	0.013
531	0.014	0.022	0.313	0.066	0.493	0.001	0.012
551	0.012	0.005	0.251	0.065	0.494	0.001	0.011
667	0.018	0.003	0.054	0.061	0.494	0.001	0.009

Table 2.4 Matlab scripts relevant to field observations.

Name	Description
SPMRcorrection	Corrects SPMR data

2.3 Hydrolight – Ecolight radiative transfer numerical model

Radiance is the fundamental radiometric quantity that describes the depth (z), directional (θ,ϕ), and wavelength (λ) behaviour of light (Mobley, 1994) and can be simulated using radiative transfer modelling (chapter 1). This study uses reflectance values calculated from the Hydrolight radiative transfer model. Hydrolight (version 5, HE5) is a numerical radiative transfer model distributed by Sequoia Scientific Inc (Mobley & Sundman, 2008). It solves the time-independent, one-dimensional, unpolarized radiative transfer equation (RTE) to compute radiance distributions and derived quantities, for example remote sensing reflectance, within or leaving a body of water. A subset of the Hydrolight package is Ecolight, which solves the azimuthally-averaged version of the RTE. By supplying absorption, scattering and backscattering coefficients, Hydrolight is able to effectively simulate an underwater water climate representative of coastal seas. Inherent optical properties (IOP) can be supplied in the form of ac-9 and hs-2 measurements. Other physical parameters known to alter light leaving the surface of the water can also be included, such as bottom reflectance boundary types and ambient wind speeds. Table 2.5 presents the Hydrolight settings used for successful radiance modelling of the Irish Sea.

For the purposes of this study, total IOPs were reconstructed for waters dominated by minerals and chlorophyll using specific inherent optical properties (Table 2.3). Appropriate ranges of constituent concentrations were derived from field observations in the Irish Sea and Bristol Channel: these were 0 to 1.0 m^{-1} absorption at 440 nm for CDOM, 0 to 10 mg m^{-3} for CHL and 0 to 20 g m^{-3} for MSS. Values for the total inherent optical properties of a given volume of seawater were then calculated by summing the contributions of the individual constituents. Within these ranges, concentrations were specified for each constituent at logarithmic intervals and all possible combinations of concentrations considered, so that a total of 20328 model runs were completed. Hydrolight performs calculations at specified wavebands and by default interpolates IOP data to the relevant wavelength. Interpolating spectral IOPs to MODIS wavebands before supplying coefficients to the model avoids the necessity for interpolation by Hydrolight. A comparison of backscattering spectra interpolated before and during model simulation is shown in

Figure 2.9. Clear spectral differences are present in data generated by two separate interpolation methods. The spectral location of the final constant value can be extended to longer wavelengths by applying the pre-interpolation method. This effect is most prominent for backscattering coefficients as data is only available in two wavebands.

Model simulations generated for this study were performed using Ecolight due to the reduced computational run time and data storage requirements. For the combinations of optically significant constituents measured in-situ, reflectance spectra were generated by supplying IOPs derived from measured constituent concentrations and SIOPs to the radiance transfer model. A comparison between modelled and measured reflectance demonstrates the performance of the radiance transfer modelling routine, shown in Figure 2.10. The model generates reasonable estimates of remote sensing reflectance with an increasing trend of the R^2 value with wavelength indicating the radiance transfer calculations are more accurately representing reflectance at longer wavelengths. Results show $R_{rs}667$ is adequately replicated by the radiance transfer modelling technique. Analysis of Ecolight outputs were conducted using the Matlab software package. Relevant script headings can be found in Table 2.6 (scripts available on request).

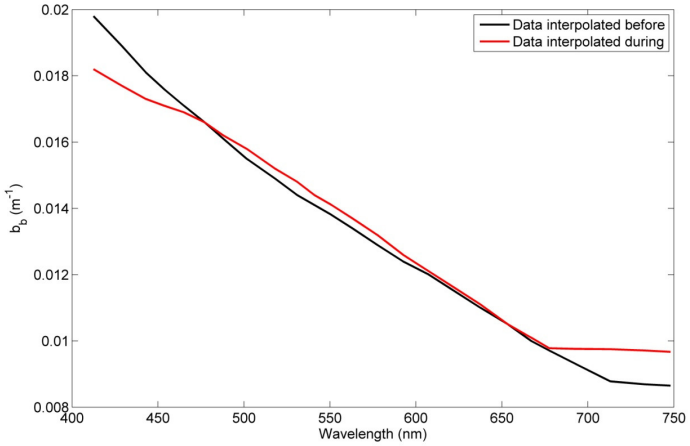

Figure 2.9 Comparison of backscattering coefficients interpolated before and during Hydrolight simulations. Differences are present due to the Hydrolight default interpolation scheme.

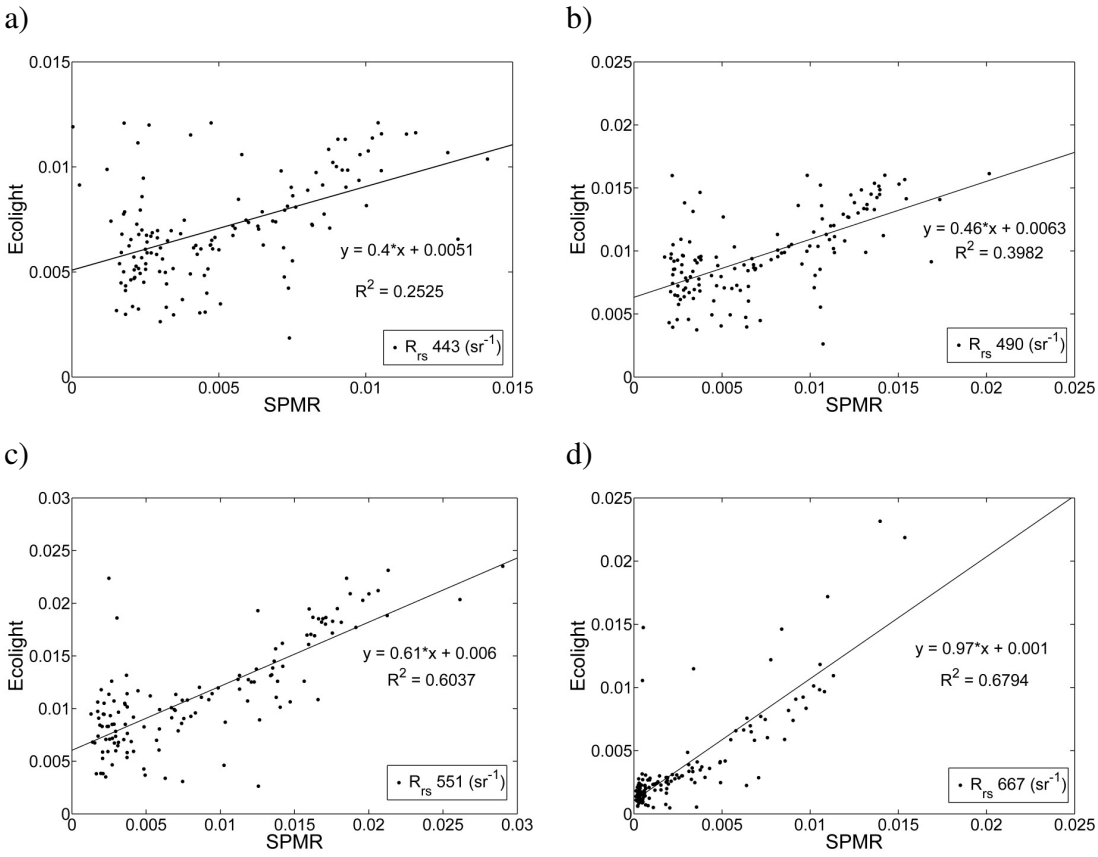

Figure 2.10 Comparison of SPMR reflectances and reflectances generated by the Ecolight radiance transfer modelling package, at a) 443 nm, b) 490 nm, c) 551 nm and d) 667 nm. $R_{rs}667$ is sufficiently modelled by radiance transfer modelling.

Table 2.5 Control inputs provided to Hydrolight for representative radiance modelling

Variable	**Description**	**Value**
PARmin	Lowest wavelength included in PAR calculations	400 nm
PARmax	Highest wavelength included in PAR calculations	700 nm
PhiChl	Chlorophyll fluorescence efficiency	0.02

Raman0	Raman reference wavelength	488 nm
RamanXS	Raman scattering coefficient at the reference wavelength	0.00026
iIOPmodel	IOP model selection	IOP data model (user supplied)
iSkyRadModel	Sky radiance model selection	Semi-empirical sky radiance model of Harrison and Coombes
iSkyIrradModel	How are sky irradiances obtained	RADTRANX
Iastropt	Absorption model (pure water)	Smith and Baker
Itype	Type of concentration input	Constant with depth
Wavel	Wavelength selection	MODIS
Ichlfl	Chlorophyll fluorescence	On
icdomfl	CDOM fluorescence	Off
ibiolum	Bioluminescence presence	Off
iraman	Raman scattering (inelastic)	Off
Iflagsky	Sky model	Semi-analytical
suntheta	Solar zenith angle (in degrees)	45
sunphi	Solar azimuthal angle	0
cloud	Cloud cover	0
Windspeed	Windspeed	3.10 m/s
Ibotm	Type of bottom boundary	Water column is infinitely deep
Output depths	Depth values	Zero to 50 m, increments of 2 m

Table 2.6 Matlab scripts relevant to radiance transfer modelling

Name	**Description**
generateiops	Generates IOP files for Ecolight run
sampleerrors	Generates IOPs for given parameters
alt_ouput	Combines all model outputs into one file for each quantity

Key points from chapter 2

1. MODIS Aqua satellite remote sensing measurements were used to construct a database of Irish Sea reflectance. These data were processed from level 0 to level 2B using SeaDAS data analysis package. Consolidation of satellite reflectance data created time series covering the extent of the Irish Sea. Matlab routines were developed for the purpose of correcting and analysing satellite data.

2. In-situ measurements of SPMR upwelling radiance, L_u, were reprocessed using a Matlab routine developed to correct a processing error uncovered during the course of the study. Pre processed L_u values generated discrepancies in subsequent R_{rs} of up to 150%.

3. SIOPs and varying ranges of in-water constituents were provided to Ecolight radiance transfer package to generate 20328 model runs. Matlab software developed specifically for use with Ecolight allowed the batch processing and extraction of data.

References

Bailey, S.W., Franz, B.A., Werdell, P.J., 2010. Estimation of near-infrared water-leaving reflectance for satellite ocean color data processing. OPTICS EXPRESS, 18 (7), 7521-7527.

Brown, I.C., 2010. The inversion of in situ inherent optical property measurements in shelf seas. Ph.D. Thesis, University of Strathclyde, Glasgow.

GES DISC via Giovanni web portal, 2010. http://disc.sci.gsfc.nasa.gov/giovanni.

Gohin, F., Druon, J.N., Lampert, L., 2002. A five channel chlorophyll concentration algorithm applied to SeaWiFS data processed by SeaDAS in coastal waters. INTERNATIONAL JOURNAL OF REMOTE SENSING, 23 (8), 1639-1661.

HOBI Labs. 2008. Hydroscat-2 spectral backscattering sensor user's manual (Revision H). HOBI Labs Inc., Washington, USA.

Kilpatrick, K.A., Podesta, G.P., Evans, R., 2001. Overview of the NOAA/NASA advanced very high resolution radiometer Pathfinder algorithm for sea surface temperature and associated matchup database. JOURNAL OF GEOPHYSICAL RESEARCH-OCEANS, 106 (C5), 9179-9197.

Lee, M.A., Tzeng, M.T., Hosoda, K., Sakaida, F., Kawamura, H., Shieh, W.J., Yang, Y., Chang, Y., 2010. Validation of JAXA/MODIS Sea Surface Temperature in Water around Taiwan Using the Terra and Aqua Satellites. TERRESTRIAL ATMOSPHERIC AND OCEANIC SCIENCES, 21 (4), 727-736.

Maffione, R.A. & D.R. Dana. 1997. Instruments and methods for measuring the backward-scattering coefficient of ocean waters. APPLIED OPTICS, 36, 6057–6067.

Marcello, J., Eugenio, F., Hernandez, A., 2004. Validation of MODIS and AVHRR/3 sea surface temperature retrieval algorithms. IGARSS 2004: IEEE INTERNATIONAL GEOSCIENCE AND REMOTE SENSING SYMPOSIUM PROCEEDINGS, VOLS 1-7 - SCIENCE FOR SOCIETY: EXPLORING AND MANAGING A CHANGING PLANET, 839-842.

McClain, C.R., W.E. Esaias, W. Barnes, B. Guenther, D. Endres, S. Hooker, G. Mitchell, and R. Barnes, 1992: Calibration and Validation Plan for SeaWiFS. NASA Tech. Memo. 104566, Vol. 3, S.B. Hooker and E.R. Firestone, Eds., NASA Goddard Space Flight Center, Greenbelt, Maryland, 41 pp.

McKee, D., Cunningham, A., 2006. Identification and characterisation of two optical water types in the Irish Sea from in situ inherent optical properties and seawater constituents. ESTUARINE COASTAL AND SHELF SCIENCE, 68 (1-2): 305-316.

McKee, D., Cunningham, A., Dudek, A., 2007. Optical water type discrimination and tuning remote sensing band-ratio algorithms: Application to retrieval of chlorophyll and K-d(490) in the Irish and Celtic Seas. ESTUARINE COASTAL AND SHELF SCIENCE, 73 (3-4), 827-834.

Mermaid calval portal, 2010, http://calvalportal.ceos.org/cvp/web/guest/mvt.

Minnett, P.J., Evans, R.H., Kearns, E.J., Brown, O.B., 2002. Sea-surface temperature measured by the Moderate Resolution Imaging Spectroradiometer (MODIS). IGARSS 2002: IEEE INTERNATIONAL GEOSCIENCE AND REMOTE SENSING SYMPOSIUM AND 24TH CANADIAN SYMPOSIUM ON REMOTE SENSING, VOLS I-VI, PROCEEDINGS - REMOTE SENSING: INTEGRATING OUR VIEW OF THE PLANET, 1177-1179.

M_Map: Mapping toolbox for Matlab, 2009, http://www.eos.ubc.ca/~rich/map.html.

Mobley, C.D. 1994. Light and water: radiative transfer in natural waters. Academic Press. San Diego, California.

Mobley, C.D., Sundman, L.K., 2008. Hydrolight 5 Ecolight 5 User's Guide, Sequioa Scientific, Bellevue, USA.

Morel, A., Gentili, B., 2009. A simple band ratio technique to quantify the colored dissolved and detrital organic material from ocean color remotely sensed data. REMOTE SENSING OF ENVIRONMENT, 113 (5), 998-1011.

NASA Ocean Color Web, 2010, http://oceancolor.gsfc.nasa.gov/.

NASA SeaWiFS Bio-optical Archive and Storgae System (SeaBASS), 2010, http://oceancolor.gsfc.nasa.gov/.

Nghiem S.V., Li, F.K., Lou, S.H., Neumann, G., Mcintosh, R.E., Carson, S.C., Carswell, J.R., Walsh, E.J., Donelan, M.A., Drennan, W.M., 1995. Observations of RADAR backscatter at KU and C-BANDS in the presence of large waves during the surface-wave dynamics experiment. IEEE TRANSACTIONS ON GEOSCIENCE AND REMOTE SENSING, 33 (3), 708-721.

O'Reilly, J.E., Maritorena, S., Mitchell, B.G., Siegel, D.A., Carder, K.L., Garver, S.A., Kahru, M., McClain, C., 1998. Ocean color chlorophyll algorithms for SeaWiFS. JOURNAL OF GEOPHYSICAL RESEARCH-OCEANS, 103 (C11), 24937-24953.

ProSoft 7.7 User Manual, 2009. Satlantic Inc., Nova Scotia, Canada.

Sabins, F.F. Jr., 1978. Remote sensing principles and interpretations. San Francisco, W.H. Freeman.

Stavn, R.H & H.J. Richter. 2008. Biogeo-optics: particle optical properties and the partitioning of the spectral scattering coefficient of ocean waters. APPLIED OPTICS, 47, 2660–2679.

WETLabs. 2008. ac-9plus Users Guide (Revision K). WETLabs Inc. Philomath, Oregon.

Chapter 3

Use of the Proudman Oceanographic Laboratory Coastal Ocean Modelling System (POLCOMS)

Summary

POLCOMS is a physical ocean model developed by the Proudman Oceanographic Laboratory (Holt et al., 2001, Holt et al., 2005 and Holt et al., 2008). The model simulates hydrological processes in the shallow and deep waters of the UK shelf, with a fine resolution grid of approximately 1.85 km covering the Irish and north Celtic Sea. Baroclinic layers are combined to construct a three-dimensional model which can generate small scale vertical and horizontal changes in density. Physical properties of the water column are simulated incorporating actual climatological observations. With excellent feature-preserving properties, POLCOMS can effectively simulate on-shelf baroclinic processes such as fronts and river plumes. The purpose of this chapter is to provide a general introduction to the POLCOMS model. This includes a simple validation of model outputs and a description of secondary variables relevant to this work. This chapter shall also include a section related to estimating bed shear values in the Irish Sea.

3.1 Model equations

Equations of state and motion are the foundation of the POLCOMS model. The coordinate system is defined in spherical polar sigma coordinates, with χ, ϕ and σ describing eastward, northward and vertical directions respectively. Here, $\sigma = (z - \xi) / (h + \xi)$, where z is the Cartesian vertical coordinate, h is the water depth relative to mean sea level ($z = 0$) and ξ is the elevation above this point. Subsequently, total water depth $H = h + \xi$. Discretised levels in σ represent baroclinic layers which are variable over horizontal space. An approximation of the UNESCO equation of state (Fofonoff and Millard, 1983) is used to calculate density as a function of potential temperature (T), salinity (S) and pressure (p);

$$\rho(T,S,p) = \rho(T,S,0) + \rho'(T,S,p) \tag{3.1}$$

with

$$\rho'(T,S,p) = 10^4 \frac{p}{c^2}\left(1 - 0.2\frac{p}{c^2}\right) \tag{3.2}$$

and

$$c = 1449.2 + 1.34(S-35) + 4.55T - 0.045T^2 + 0.00821p + 15.0\times10^{-9}p^2 \tag{3.3}$$

following Mellor (1991). The hydrostatic pressure is given by;

$$P = P_\alpha + \rho_0(\psi + g\xi - gz) + 0.002282gZ^2 \tag{3.4}$$

Here ρ_0 = 1027kgm^{-3}, $Z = z - \xi = \sigma H$. P_α is the atmospheric pressure and $\psi = H\int_0^\sigma b d\sigma$. The incompressible, hydrostatic, Boussinesq equations of motion are solved to allow time splitting between barotropic and baroclinic components. The equations are divided into depth varying and depth independent parts; so the eastwards velocity is $u = \bar{u}(\chi,\varphi,t) + u_r(\chi,\varphi,\sigma,t)$ and the northward velocity is $v = \bar{v}(\chi,\varphi,t) + v_r(\chi,\varphi,\sigma,t)$. The depth mean equations are;

$$\frac{\delta\bar{u}}{\delta t} = f\bar{v} - (R\cos\varphi)^{-1}\left[g\frac{\delta\xi}{\delta\chi} + \rho_0^{-1}\frac{\delta P_\alpha}{\delta\chi}\right] + H^{-1}\left[F_S - F_B\right] + NLB_\chi \tag{3.5}$$

and

$$\frac{\delta\bar{v}}{\delta t} = -f\bar{u} - R^{-1}\left[g\frac{\delta\xi}{\delta\varphi} + \rho_0^{-1}\frac{\delta P_\alpha}{\delta\varphi}\right] + H^{-1}\left[G_S - G_B\right] + NLB_\varphi \tag{3.6}$$

whilst the equations for the depth varying components are given by;

$$\frac{\delta u_r}{\delta t} = -L(u) + fv_r + \frac{uv\tan\varphi}{R} - \Pi_\chi + D(u) - H^{-1}\left[F_S - F_B - NLB_\chi\right] \qquad (3.7)$$

and

$$\frac{\delta v_r}{\delta t} = -L(v) + fu_r + \frac{u^2\tan\varphi}{R} - \Pi_\varphi + D(v) - H^{-1}\left[G_S - G_B - NLB_\varphi\right] \qquad (3.8)$$

A full description of the derivation of these equations and their component terms can be found in (Holt & James, 2001).

3.2 Model variables

The POLCOMS model generates a series of functional physical parameters, as shown in Table 3.1. Each property is computed as a three-dimensional variable. Primary model outputs relevant to this study include potential temperature (^{o}C), salinity (p.s.u), depth (m) and vector components of current velocities (ms^{-1}), which were obtained from Dr Jeff Polton at the Proudman Oceanographic Laboratory, Liverpool. Daily average temperature and salinity values were generated for the top and bottom of the water column, whilst current velocities, *u* and *v*, were depth averaged. The period of simulation ranged from 1st January 2006 to 31st December 2007.

Table 3.1 POLCOMS model variables.

Variable	Description	Units
aa	Turbulent viscosity	$m^2 s^{-1}$
ak	Turbulent diffusivity	$m^2 s^{-1}$
al	Mixing length	m
b	Buoyancy	$m s^{-2}$
bsal	Boundary condition salinity	p.s.u.
btmp	Boundary condition temperature	^oC
fu	u volume flux (per length)	$m^2 s^{-1}$
fv	v volume flux (per length)	$m^2 s^{-1}$
om	Vertical velocity (σ-units)	s^{-1}
qsq	Turbulent kinetic energy x 2	$m^2 s^{-2}$
sal	Salinity	p.s.u.
tmp	Potential temperature	^oC
u	Eastward horizontal velocity	$m s^{-1}$
v	Northward horizontal velocity	$m s^{-1}$
u0	Eastward velocity (last time step)	ms^{-1}
v0	Northward velocity (last time step)	$m s^{-1}$
ur	Eastward velocity (depth varying)	$m s^{-1}$
vr	Northward velocity (depth varying)	$m s^{-1}$
met1	Surface forcing data (time 1)	Various
met2	Surface forcing data (time 2)	Various
pressure	Pressure for compressibility	$N m^{-2}$
rhobar	Mean density	$kg m^{-3}$
aln	Mixing length profile	n.d.
spm	Suspended particulate matter or tracer	$g m^{-3}$
bed	Deposited material	$g m^{-2}$

3.3 Model performance

As a first step, model performance was investigated by comparison with satellite measured sea surface temperature (SST). The high spatial and temporal coverage of satellite measurements make this an efficient technique for model validation. The two-dimensional correlation coefficient, which describes the degree of linear dependence between two vectors (images), was calculated using monthly averages of satellite measured (MODIS) and model simulated SST. Figure 3.1 shows seasonal changes in the two-dimensional correlation coefficient (Noda and Ozaki, 2004) for SST comparisons over a period of two years. For both years, a general decrease in the correlation coefficient in spring and summer months, suggests the model is failing to reproduce surface temperature values during this hydrologically complex period. Accurate model representation of SST for the remaining months in 2006 is indicated by correlation coefficients close to 1. Results for 2007 show varied levels of agreement between MODIS and POLCOMS data. The minimum coefficient values for the 2007 simulation occur during autumn months, contradictory to the expected summer (Holt et al., 2005).

Images of September 2007 monthly averaged SST magnitudes are shown in Figure 3.2. With the lowest correlation coefficient, this example has been chosen due to the apparent poor performance of model simulations for this period. The spatial variation in SST can be observed from images generated from MODIS and POLCOMS data. Analysis of transect data from SST images indicates the existence of a temperature offset, where for a large part of the region of interest, POLCOMS is systematically underestimating the surface temperature values. Figure 3.3 contains data from the displayed transect (Figure 3.2) which runs south to north from point A. Values obtained from POLCOMS are approximately 2 ^{o}C less than those measured by the satellite at each stage of the transect. The temperature gradient located between 60 km and 100 km of Figure 3.3 is indicative of a thermal front. A difference of ~10 km separates the location of the measured and modelled front, demonstrating the model capability of accurately reproducing hydrological features.

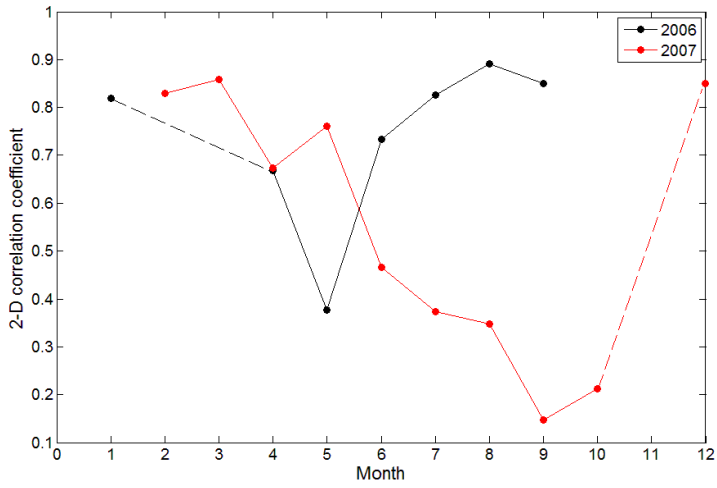

Figure 3.1 Two dimensional correlation coefficients calculated for monthly averaged MODIS and POLCOMS SST. The data time series ranges from 2006 to 2007, depicted by black and red markers respectively. Months containing no data points did not yield any cloud-free satellite measurements in the region of interest. High correlation coefficients indicate a good level of agreement between measured and modelled data.

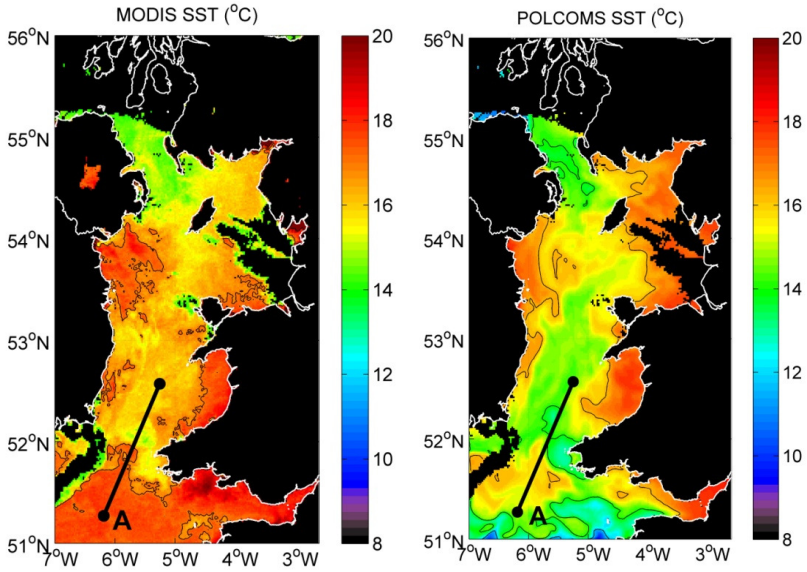

Figure 3.2 MODIS and POLCOMS September 2007 (lowest 2-d correlation coefficient) monthly averaged SST. The black line depicts location and orientation of transect.

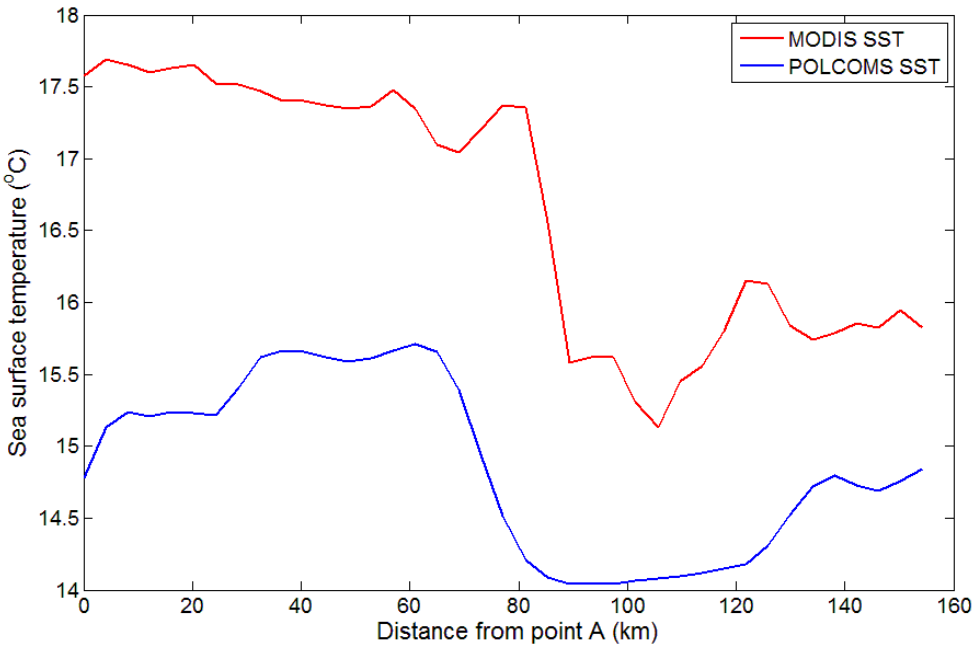

Figure 3.3 Transect extract of MODIS (red) and POLCOMS (blue) September 2007 monthly averaged SST. POLCOMS is under-estimating SST as illustrated by consistent offset. However similar locations of region of strongest thermal gradient suggest the model is effectively simulating hydrological features.

Verification of POLCOMS SST has shown varied levels of model performance. Winter simulations produce estimations of SST which closely correlate with satellite measurements. The model effectively fails to reproduce absolute sea surface temperatures during spring and summer months, where quantitative under-estimations of SST are generated. In these examples, the maximum difference between measured and modelled SST is approximately 2°C. Nonetheless, important spatial features are captured by POLCOMS meaning modelled data can be used for the purposes of this study.

3.4 Derived variables

POLCOMS model variables provide predictive information on UK waters. Application of primary outputs to alternative hydrological equations can offer additional information on the state of our seas. A hydrological feature of particular interest is the stratification and mixing process of coastal shelf seas. Stratification of the water column is a phenomenon present in most coastal and shelf seas. There are two stratification types considered, salinity, where a vertical gradient in the saline content promotes separation from mixed waters and thermal, where the water column is separated by large temperature differences. Thermal stratification occurs during periods of calm, when high insolation heats the top layer of water creating a temperature difference between the upper and lower layers. The upper, less dense water is separated from the cooler, more dense water by a thin layer known as the thermocline in which there are distinct temperature and density gradients. A similar separation occurs when the water column in salinity stratified. Here discretised layers of density are induced by variations in the saline content of the water.

3.4.1 Simpson-Hunter criterion

Predictions of stratification and mixing regimes can be obtained by considering changes to the potential energy available in the water column relative to mixed conditions. For stratification to occur, potential energy must exceed turbulent kinetic energy. The rate of change of potential energy, V, per area, A, with time is given by;

$$\frac{dV}{dt} = \gamma \frac{4}{3\pi} \varepsilon k_b \rho_w U^3 + \delta k_s \rho_a W^3 - \frac{\alpha g Q h}{2c} \qquad (3.9)$$

where U is the tidal current amplitude, W is wind speed, Q is the heating rate and h is water depth. Definitions for the remaining terms in this equation can be found in Table 3.2. Wave and current induced mixing provides a positive input to potential energy (decreasing stratification), whilst heat exchange at the ocean surface (and buoyancy effects from freshwater river discharge) reduce the available potential energy and increase stratification. At a front, where transitions between stratified and mixed regimes occur, $V = 0$;

$$\frac{\alpha g Q h}{2c} = \gamma \frac{4}{3\pi} \varepsilon k_b \rho_w U^3 + \delta k_s \rho_a W^3 \qquad (3.10)$$

If the wind effect is uniform and ε, γ, and k are considered constants, the formation of a front is determined by the parameter h/U^3. This is known as the Simpson-Hunter criterion (SHC) (Simpson & Hunter, 1974). High values of SHC indicate stratification – the surface mixed layer is large or the current velocity is inadequate to overturn the surface layer. Low values indicate mixing of the water column, with shallow depths or strong tidal velocities. In this form, the SHC is seasonally dependent and can only be used to predict stratification in summer climates.

Table 3.2 Terms from equation (3.9)

Term	Description	Unit
ρ_w, ρ_a	Density of seawater and air respectively	kg m^{-3}
k_b, k_s	Bottom and surface drag coefficient respectively	n.d.
γ	Ratio of wind-induced surface current to wind speed	n.d.
α	Volume expansion coefficient	K^{-1}
g	Acceleration due to gravity	m s^{-2}
c	Specific heat	J kg^{-1} K^{-1}
ε, δ	Efficiencies	n.d.

3.4.2 Delta sigma

One technique for investigating stratification in coastal seas involves analysis of the density structure of the water column. Using temperature and salinity outputs from the POLCOMS model, stratification can be predicted by comparing the density estimated at the water surface and seafloor. The density of seawater, ρ, depends on temperature, (T), salinity, (S) and pressure, (p) through a relation known as the equation of state;

$$\rho(S,T,p) = \rho(S,T,0)/\left[1 - p/K(S,T,p)\right] \tag{3.11}$$

where $K(S,T,p)$ is the bulk modulus. Fofonoff and Millard (1983) published a detailed description of this algorithm in a UNESCO technical paper. The quantity *sigma-T* (σ_T), is more commonly employed and is equal to (ρ-*1000*). Delta sigma (or $\Delta\sigma$), the difference in σ_T between the top and bottom of the water column, is used to predict patterns of stratification. High and low values of $\Delta\sigma$ are expected in stratified and mixed regimes respectively.

The feasibility of $\Delta\sigma$ as a predictor of stratification can be assessed using field observations of *Sigma-T*, which is measured routinely on research cruises using conductivity – temperature – depth profiling instruments (CTD) (Sea-Bird Electronics Inc., Washington, USA). Salinity is estimated from conductivity measurements and pressure derived from depth. Figure 3.4 a) shows model-derived $\Delta\sigma$ calculated with temperature and salinity from 07 August 2006 (consistent with Bristol Channel 2006 research cruise). Station locations are highlighted on the map with the corresponding CTD profiles shown in Figure 3.4 b). Stations 3, 4 and 5 are located in a region with high values of $\Delta\sigma$ and would therefore be described as stratified. The density gradients, measured in CTD profiles at these stations, which are indicative of stratification, corroborate this assumption. General agreement between model predicted and in-situ observed stratification suggests $\Delta\sigma$ can be used as a suitable predictor of stratification.

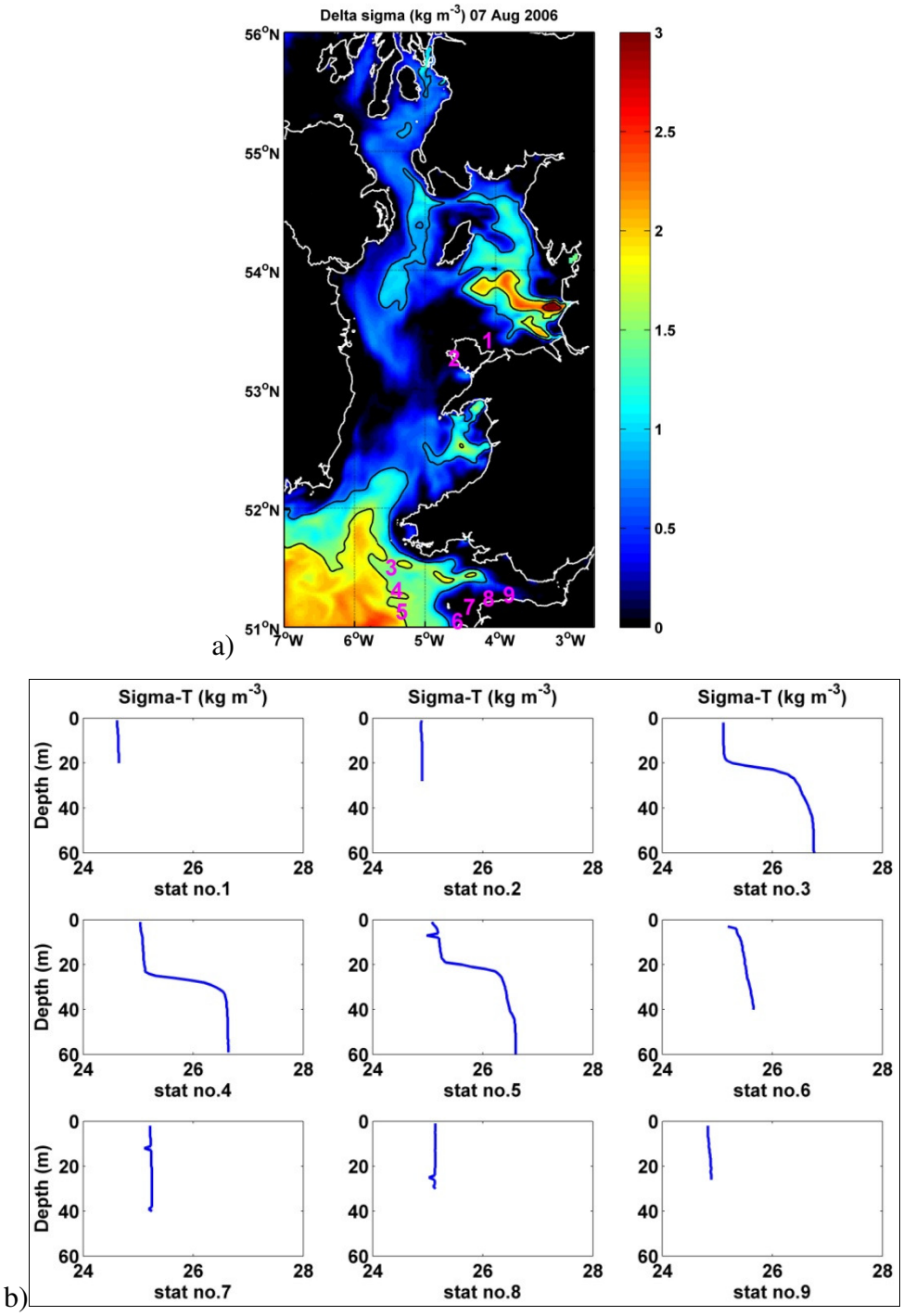

Figure 3.4 a) Δσ calculated from modelled temperature and salinity for 07 August 2006, with station locations highlighted in magenta. Density gradients in depth profiles b) measured at each station indicate the presence of stratification. Results from modelled predictor of stratification are consistent with in-situ field measurements.

3.4.3 Bed shear stress calculation

The erosion, suspension and deposition of sediment in coastal seas is controlled by the bed shear stress (BSS) (Soulsby & Clarke, 2005) which is a measure of the frictional force exerted on an area of the sea floor by wave and current flows (N m^{-2}). The inclusion of a wave component to the total BSS introduces seasonality to this hydrodynamic parameter, where increased wind-induced waves raise the levels of BSS in shallow (< 100 m) waters.

For a rough turbulent flow regime (determined by the Reynolds number) (Thorpe, 2005), maximum bed shear stress, τ_{max}, under combined waves and currents is a function of the depth averaged current velocity, $\bar{U}$, and the maximum drag coefficient, C_{Dmax};

$$\tau_{\max} = \rho C_{D\max} \overline{U}^2 \tag{3.12}$$

where ρ is the density of sea water. C_{Dmax} can be found using the following expression;

$$C_{D\max} = \left[\left(C_{Dm} + T_3 \left(\frac{U_w}{\overline{U}} \right) \left(\frac{f_{wr}}{2} \right)^{1/2} \left| \cos\varphi \right| \right)^2 + \left(T_3 \left(\frac{U_w}{\overline{U}} \right) \left(\frac{f_{wr}}{2} \right)^{1/2} \left| \sin\varphi \right| \right)^2 \right]^{1/2} \tag{3.13}$$

where

$$T_1 = \max\left\{ a_r \left(\frac{f_{wr}}{2} \right)^{1/2} \left(\frac{A}{z_0} \right), 12 \right\} \tag{3.14}$$

$$T_2 = \frac{h}{T_1 z_0} \tag{3.15}$$

$$T_3 = \left[C_{Dr}^2 + \left(\frac{f_{wr}}{2} \right)^2 \left(\frac{U_w}{\overline{U}} \right)^4 \right]^{1/4} \tag{3.16}$$

Here,

$$C_{Dr} = \left[\frac{0.4}{\ln(h/z_0) - 1} \right]^2 \tag{3.17}$$

For equation (3,13),

$$C_{Dm} = \left[\left(A_1^2 + A_2 \right)^{1/2} - A_1 \right]^2 \tag{3.18}$$

with

$$A_1 = \frac{1}{2} \left(\frac{u_{*e}}{\overline{U}} \right) \frac{\ln(h/\delta) - 1}{\ln(\delta/z_0)} = \frac{T_3 \left[\ln(T_2) - 1 \right]}{2 \ln T_1} \tag{3.19}$$

$$A_2 = \frac{\kappa u_{*e}}{\overline{U}} \frac{1}{\ln(\delta/z_0)} = \frac{0.4 T_3}{\ln T_1} \tag{3.20}$$

Here, h is the water depth z_0 is the bed roughness length (median grain diameter, d_{50} = 0.5 mm, divided by 12), δ is the wave boundary layer thickness, κ is von Karman's constant (= 0.40), ϕ is the angle between wave and current directions, a_r = 0.24, and u_{*e} is the effective friction velocity. The parameter u_{*e} can be written in terms of the current, τ_c, and wave, τ_w, contributions to BSS;

$$u_{*e}^2 = \frac{\left(\tau_c^2 + \tau_w^2 \right)}{\rho} \tag{3.21}$$

The wave-only component of BSS, τ_w, is dependent on the wave orbital velocity amplitude at the seabed, U_w, and the friction factor for rough turbulent flows, f_{wr};

$$\tau_w = \frac{1}{2}\rho f_{wr} U_w^2 \tag{3.22}$$

and

$$f_{wr} = 1.39\left(\frac{A}{z_0}\right)^{-0.52} \tag{3.23}$$

The orbital amplitude of wave motion, A, is the product of the wave orbital velocity and the wave period;

$$A = \frac{U_w T}{2\pi} \tag{3.24}$$

Here wave orbital velocity, U_w, is obtained from measurements of wave period, T, significant wave height, H, and water depth, h;

$$U_w = \frac{\pi H}{T \sinh(kh)} \tag{3.25}$$

k is the wave number, derived from wavelength L;

$$k = \frac{2\pi}{L} \tag{3.26}$$

where (for deep water waves),

$$L = \frac{T^2 g}{2\pi} \tag{3.27}$$

For τ_{max} calculations, wave information was extracted from a spectral WAve Model (WAM) coupled with POLCOMS high resolution Irish Sea tidal model (Brown et al., 2010). τ_{max} was calculated using maximum daily wave (T, H) and current ($\bar{U}$) POLCOMS-WAM outputs for 2005. The unknown angle between wave and current directions was set to 0^{o} for all BSS calculations. Figure 3.5 shows τ_{max} varying as a function of angle. Setting the angle between wave and current flows to constant zero ensures the generation of absolute maxima. Estimations of τ_{max} and $\Delta\sigma$ will be used to identify hydrological features in the Irish Sea. These shall form the basis of the physical parameters predicted to influence sediment dynamics in the region. Modelled parameters will be analysed in conjunction with ocean colour data to determine whether reflectance variability can be attributed to physical properties. All POLCOMS data was analysed using the Matlab software package. Relevant scripts are described in Table 3.3 (scripts available on request).

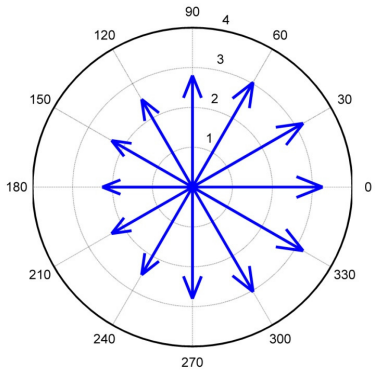

Figure 3.5 Varying τ_{max} as a function of angle between wave and current flows.

Table 3.3 Matlab scripts for POLCOMS analysis

Name	**Description**
POLsat	Projects POL and satellite data to consistent coordinates
equation_of_state	Calculates density as a function of temperature, salinity and depth.
timeseries_rrs667_delsig	Generates time series of satellite and POLCOMS data
read_daily_UV_max	Extracts maximum current and wave data
calculate_trms	Calculates maximum bed shear stress τ_{max}

Key points from chapter 3

1. POLCOMS data were obtained from the Proudman Oceanographic Laboratory. These consisted of surface and bottom temperature and salinity, depth and depth-averaged current velocities. From the WAM model, wave height and period were also obtained.

2. Temperature, salinity and depth data were used to calculate surface and bottom density using equations of state.

3. Validation of model temperature predictions were performed using MODIS satellite Sea Surface Temperature (SST) data. This demonstrated a discrepancy in the absolute value of modelled sea surface temperature, however geographical locations of thermal fronts were approximately consistent with MODIS SST.

4. Comparison between top and bottom density provides an indicator of stratification, $\Delta\sigma$. The use of $\Delta\sigma$ as a suitable stratification parameter was validated using CTD field measurements of sigma-T stratification. Stations containing gradients in sigma-T from density profiles corresponded to locations exhibiting increased $\Delta\sigma$.

5. Bed shear stress was calculated for the Irish Sea using POLCOMS-WAM model outputs. These will be used to highlight physical features in the region of interest.

References

Brown, J.M., Souza, A.J., Wolf, J., 2010. An 11-year validation of wave-surge modelling in the Irish Sea, using a nested POLCOMS-WAM modelling system. OCEAN MODELLING, 33 (1-2), 118–128.

Fofonoff, N.P., Millard Jr, R.C., 1983. Algorithms for computation of fundamental properties of seawater. UNESCO TECHNICAL PAPERS IN MARINE SCIENCE, 44.

Holt, J.T., James, I.D., 2001. An *s* coordinate density evolving model of the northwest European continental shelf 1, Model description and density structure. JOURNAL OF GEOPHYSICAL RESEARCH, 106 (7), 14015-14034.

Holt, J.T., Allen, J.I., Proctor, R., Gilbert, F., 2005. Error quantification of a high-resolution coupled hydrodynamic-ecosystem coastal-ocean model: Part 1 model overview and assessment of the hydrodynamics. JOURNAL OF MARINE SYSTEMS 57 (1-2), 167 – 188.

Holt, J., Umlauf, L., 2008. Modelling the tidal mixing fronts and seasonal stratification of the Northwest European Continental shelf. CONTINENTAL SHELF RESEARCH, 28 (7), 887-903.

Mellor, G.L., Ezer, T., 1991. A Gulf-stream model and an altimetry assimilation scheme. JOURNAL OF GEOPHYSICAL RESEARCH-OCEANS, 96 (C5), 8779-8795.

Noda, I., Ozaki, Y., 2004. Two-dimensional correlation spectroscopy: applications in vibrational and optical spectroscopy. John Wiley & Sons.

Sea-Bird. 2008. SBE19 plus User's Guide (version 17). Sea-Bird Electronics Inc., Washington.

Simpson, J.H., Hunter, J.R., 1974. Fronts in the Irish Sea. NATURE 250, 404–406.

Soulsby, R.L., Clarke, S., 2005. Bed Shear-stresses Under Combined Waves and Currents on Smooth and Rough Beds. Defra project FD1905 (EstProc), TR 137, Rev 1.0.

Thorpe, S.A., 2005. The turbulent ocean. Cambridge University Press.

Chapter 4

Relationships between suspended mineral concentrations and red-waveband reflectances in optically complex shelf seas

Summary

This chapter considers the uncertainties in estimates of mineral suspended solid (MSS) concentration that arise in waters where unknown quantities of optically significant constituents chlorophyll a, (CHL) and coloured dissolved organic matter, (CDOM) are present. It uses a combination of radiative transfer modelling and in-situ measurements of specific inherent optical properties to generate a data set representative of UK shelf seas. A range of constituent concentrations were considered: 0 - 20 g m^{-3} for MSS, 0 - 10 mg m^{-3} for CHL and absorption coefficients of 0 – 1.0 m^{-1} at 440 nm for CDOM. When only MSS was present, the modelled relationship between R_{rs} and MSS concentration was described by a series of hyperbolic curves containing wavelength dependent coefficients. A near linear relationship existed between modelled $R_{rs}667$ and MSS, where the curve saturation plateau occurred at concentrations greater than 20 g m^{-3}. This is a consequence of the dominance of pure water absorption which contributed 80 percent of the total absorption signal at red wavelengths. The addition of CHL and CDOM generated a more complex relationship. Second-order polynomial functions were therefore derived to give the upper and lower MSS values corresponding to a given $R_{rs}667$ measurement for specified ranges for CHL and CDOM. Validation of the relationship using UK field observations showed substantial agreement except at $R_{rs}667$ values less than 0.001 sr^{-1}, where MSS concentrations were underestimated. This however could be a result of differences in the nature of MSS measured at coastal and offshore sites. Overall, the results indicate that MSS distributions in coastal regions can be estimated to a precision of +/- 2.5 g m^{-3} at concentrations of 20 g m^{-3} and +/1.0 g m^{-3} at 5 g m^{-3} provided the concentrations of the other optically

significant materials are within the range specified in the model. A non-linear approach is required for concentrations of MSS greater than 20 g m^{-3}.

4.1 Introduction

Optical reflectance variations are the result of changes in concentrations of three optically significant constituents, chlorophyll a (CHL), mineral suspended solids (MSS) and coloured dissolved organic matter (CDOM) (Kirk, 1994). Commonly, algorithms derived for the simultaneous estimation of each of these constituents are based on statistical regression methods and generate considerable errors (Sathyendranath 2000). Difficulties arise from the complexity of the three component inversion procedure. More recently, the development of neural network (Doerfer & Schiller 2007) and spectral matching techniques (Kuchinke et al., 2009) have produced more accurate retrievals of combinations of constituents. However, these too are subject to various disadvantages, as the accuracy of their retrievals relies on the quality of the training data sets (neural networks) and look-up tables (spectral matching) on which they are based. Furthermore, the geographical area specific nature of spectral matching and neural network techniques prevents transference to non represented regions. By attempting to retrieve concentrations of MSS only, the problem is made simpler. Accurate estimations of MSS hold many practical applications, such as the monitoring of hydrological features such as river outflows and plumes (Warrick et al. 2007, D'Sa & Ko 2008, Lahet & Stramski 2010), assessment of extreme weather events (Lohrenz et al, 2008, Yan & Tang, 2009) and for tracking the transport of chemicals and pollutants (Aldridge et al., 2003, Charlesworth et al., 2006). Estimates of suspended mineral concentrations are also necessary for predicting the light climate in coastal seas. Methods for quantifying suspended mineral concentrations in highly turbid areas have recently been reviewed by Hommersom et al. (2010). In less turbid waters, the contribution by other constituents is not masked by the dominance of MSS. To date, there have been no systematic studies conducted to review the interfering effects of other constituents on the MSS retrieval. The object of this study is to quantify these effects. This will be done using the Irish Sea, a semi-enclosed basin located between the islands of Great Britain and Ireland, as a test site. Here, an empirical algorithm exists for the retrieval

of MSS concentrations (Binding et al., 2003) and concentration ranges of the other two constituents have been previously determined (Tilstone et al. 2005, McKee et al. 2007).

4.2 Remote sensing reflectance

For a given wavelength λ, remote sensing reflectance $R_{rs}(\lambda)$ is defined as the ratio of the water leaving radiance $L_w(\lambda)$ to downward irradiance just above the sea surface $E_d(\lambda)$. Remote sensing reflectance is related to the total backscattering and absorption coefficients of a uniform water column (b_b and a) by;

$$R_{rs}(\lambda) = \frac{(1 - r_F)}{n^2}\left[\frac{f_{L\beta}}{Q}\right]\frac{b_b(\lambda)}{a(\lambda)} \tag{4.1}$$

where $f_{L\beta}$ is a variable function of the radiance distribution and volume scattering function, Q is the ratio of upwelling irradiance to radiance just below the surface, r_F is the Fresnel reflectance and n is the refractive index of seawater (Mobley, 1999). Values for the factor $f_{L\beta}$ are difficult to derive analytically, and so solutions of equation (4.1) are usually computed numerically by radiative transfer modelling. By holding illumination conditions and scattering phase function constant and ignoring inelastic scattering, R_{rs} can be considered to be proportional to b_b/a in restricted circumstances. Total backscattering and absorption coefficients can be expressed as the sum of the contributions from the three optically significant constituents (CHL, MSS and CDOM). Total a and b are obtained by multiplying the concentration of each constituent by the appropriate specific inherent optical property (indicated by an asterisk). Consequently, assuming that scattering from CDOM can be neglected:

$$R_{rs} \propto \frac{b_b}{a} = \frac{b^*_{bW} + b^*_{bMSS}MSS + b^*_{bCHL}CHL}{a_W + a^*_{MSS}MSS + a^*_{CHL}CHL + a^*_{CDOM}CDOM} \tag{4.2}$$

Radiance transfer modelling was completed using the Ecolight radiance transfer package version 5 (Sequoia). Reflectance signals were generated under standard conditions, i.e., a solar zenith angle of 45 degrees, zero cloud cover and low wind

(3.1 ms^{-1}). As a first step, SIOPs were interpolated to MODIS wavelengths. Inherent optical properties were derived using the values shown in Table 2.3 and corresponding concentration ranges representative of the Irish Sea, 0 to 1.0 m^{-1} for CDOM, 0 to 10 mg m^{-3} for CHL and 0 to 20 g m^{-3} for MSS. Particulate volume scattering functions were estimated by selecting Fournier-Forand phase functions (Fournier and Forand, 1994) with relevant b_b/b_p ratios from the Ecolight library. With concentration ranges spaced in logarithmic increments, 20328 model runs were carried out.

4.3 Satellite images

Irish Sea reflectance values, measured by the MODIS Aqua radiometer, were obtained from GSFC Ocean Color Web. Using SeaDAS version 6.1, the data were processed with the default 2-band aerosol model and iterative NIR correction. Level 2 (R_{rs}) data was mapped to an equidistant cylindrical projection and further processing carried out in Matlab (see section 2.1 for details).

4.4 Modelled relationships between MSS and R_{rs}

Using MSS SIOPs noted in Table 4.1, along with absorption and backscattering coefficients for pure seawater, the fractional contribution by seawater to total absorption and backscattering was investigated with the inclusion of increasing concentrations of MSS. Results are shown in Figure 4.1. The graph highlights the increasing importance of absorption by seawater at red wavelengths. Here, absorption by seawater contributes approximately 80% to total absorption measured at 667 nm. In contrast, backscattering by seawater is low, meaning the total backscattering coefficient is mainly dependent on MSS concentration. This has a profound consequence on the relationship between MSS and R_{rs} at red wavelengths, where the denominator of equation (4.2) is dominated by absorption due to seawater and the numerator covaries with MSS concentration. Therefore, the b_b/a ratio is a strong function of MSS producing an effective estimator of the constituent. Due to the effects of CHL fluorescence at 678 nm, and the use of NIR wavebands in atmospheric correction routines, R_{rs} measured at 667 nm is the most suitable

estimator of MSS. A similar conclusion was drawn from a more complex analysis of the underlying optics by Nechad et al. (2010).

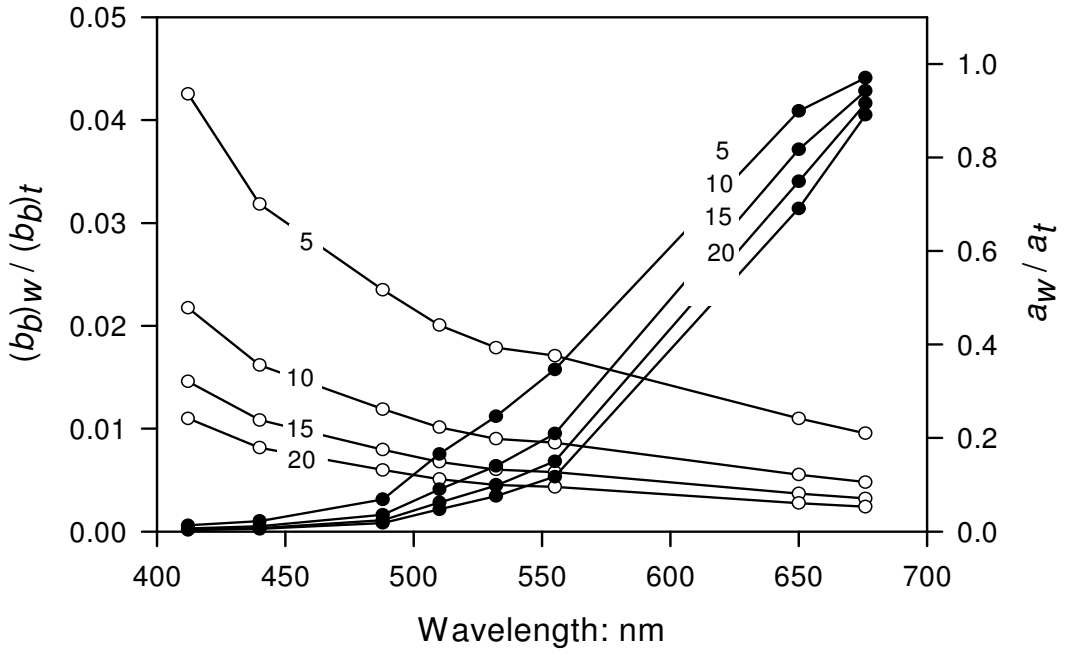

Figure 4.1 Fractional contribution of pure water to the total backscattering coefficients (left axis and open symbols) and absorption coefficients (right axis and filled symbols) for water columns containing varying concentrations of mineral suspended solids. MSS values in units of g m^{-3} are indicated for each curve.

The importance of the wavelength dependency of pure seawater absorption can also be seen in Figure 4.2. This shows reflectance measured at several MODIS wavebands as a function of MSS. R_{rs} value were calculated using Ecolight radiance transfer calculations in which CHL and CDOM were equal to zero. The solid lines depict a family of hyperbolic curves calculated using equation (4.3) with wavelength dependent coefficients given in Table 4.1.

$$R_{rs} = A + \frac{B \times MSS}{C + MSS} \tag{4.3}$$

Coefficient A, the intercept of the curves on the y- axis, equals the value of b_b/a for water. The sum of coefficients A and B provide the value at which R_{rs} saturates and coefficient C controls the sign and steepness of the curves. For wavelengths greater than 550 nm, coefficient A is equal to zero and equation (4.3) is of the same form as the Nechaud et al. (2010) suspended matter algorithm. The range for which R_{rs} can be considered as an approximately linear function of MSS increases with wavelength, and the reflectance curve for 667 nm is close to linear up to the displayed value of 20 g m^{-3}.

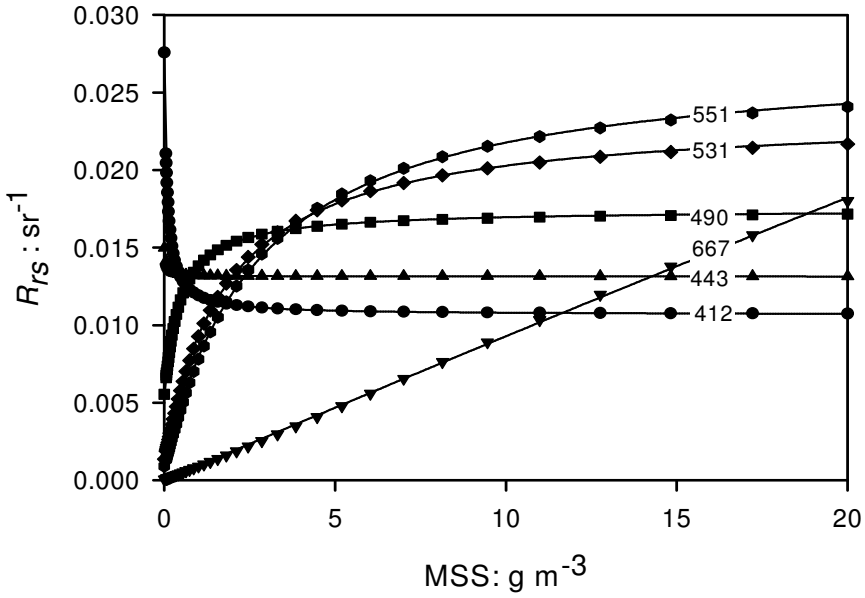

Figure 4.2 Modelled relationships between concentrations of mineral suspended solids (MSS) and remote sensing reflectance (R_{rs}) for MODIS wavebands. The symbols indicate values calculated using Ecolight, and the lines are hyperbolic curves generated using equation (4.3) with the wavelength-dependent coefficients listed in Table 4.1.

Table 4.1 Wavelength-dependent coefficients for equation (4.3).

Waveband	412	443	490	531	551	667
A	0.028	0.015	0.005	0.001	0.001	0.001
B	-0.017	-0.002	0.012	0.023	0.027	0.083
C	0.079	0.052	0.441	1.746	2.693	69.93

4.5 Sensitivity to interfering substances

The separate addition of CDOM and CHL to MSS plus seawater are shown in Figure 4.3 and Figure 4.4 respectively. The effect of adding CDOM (Figure 4.3) always decreases the $R_{rs}667$ value, as CDOM supplements only the absorption coefficient of equation (4.2). Adding CHL (Figure 4.4) has a more complex effect, whereby below 5 g m^{-3} of MSS, its addition increases the total value of $R_{rs}667$ and above 5 g m^{-3} MSS it reduces it. This is a consequence of the relative significance of the chlorophyll contribution compared to seawater in the total backscattering to absorption ratio. The combined effect of adding CHL and CDOM is shown in Figure 4.5, which shows a plot of the maximum and minimum MSS values which are consistent with a given R_{rs} when the CDOM and CHL components are allowed to vary over the full range of the model (0-1 m^{-1} for CDOM, 0-10 g m^{-3} for CHL). The upper (u) and lower (l) boundaries of these potential MSS values can be described by second order polynomials of the form:

$$MSS_{(u,l)} = C_1(u,l) \times (R_{rs}667)^2 + C_2(u,l) \times (R_{rs}667) + C_3(u,l) \qquad (4.4)$$

where MSS has units of g m^{-3} and $R_{rs}667$ has units of sr^{-1}. Values for the coefficients (C_1, C_2, C_3) for the two boundaries (u,l) are listed in Table 4.2. Interestingly, the calculated boundaries cover the range of variability in the MSS vs R_{rs} 667 relationship that was attributed to variability in the specific scattering coefficient of mineral particles by Binding et al. (2005).

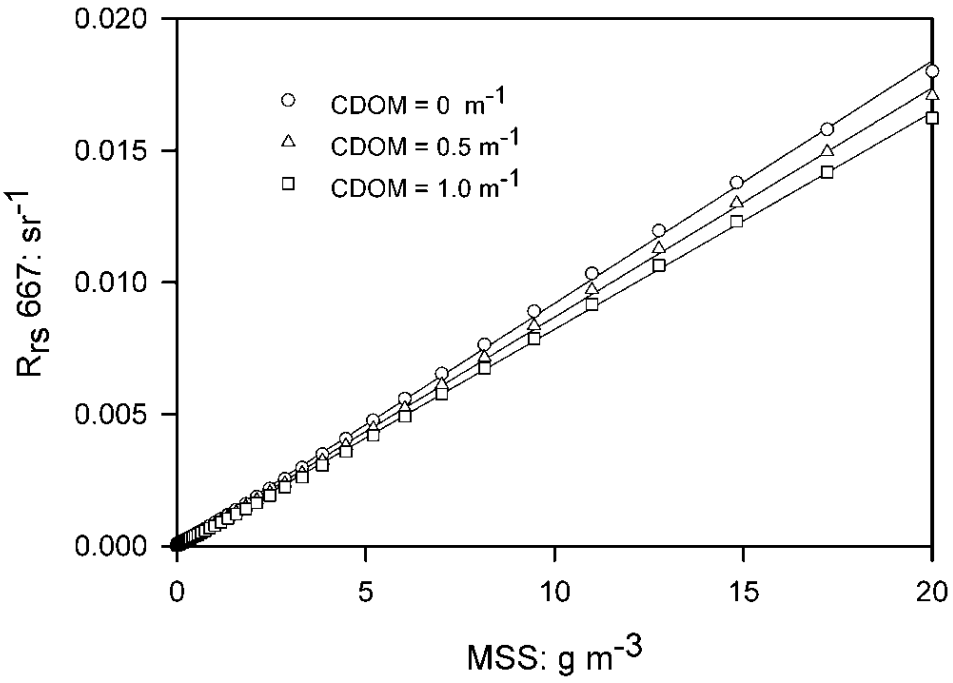

Figure 4.3 Effects of adding CDOM at the concentrations indicated on the relationship between MSS and R_{rs} in the 667 nm waveband.

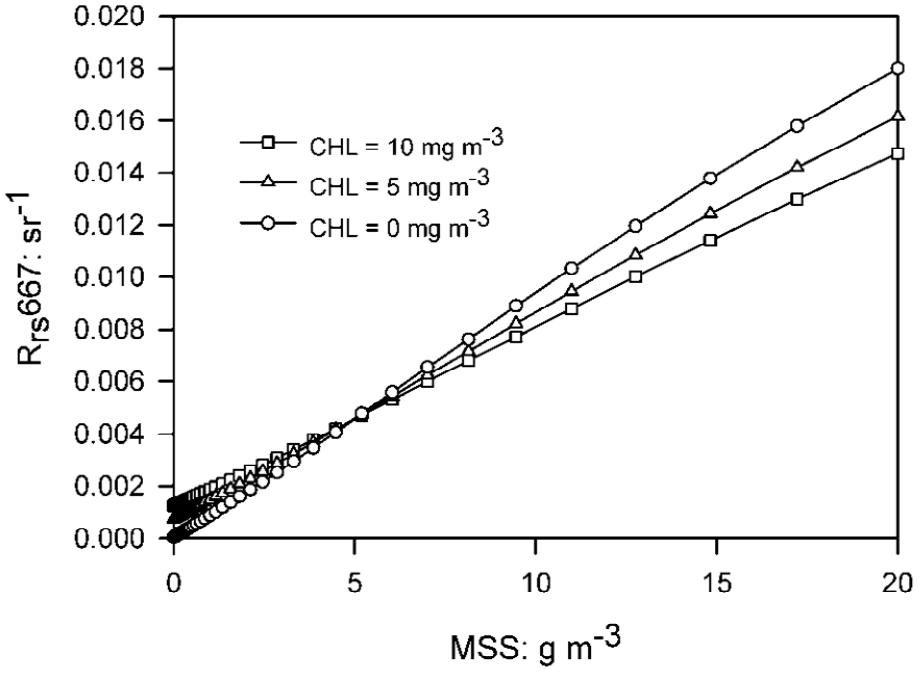

Figure 4.4 Effects of adding CHL at the concentrations indicated on the relationship between MSS and R_{rs} in the 667 nm waveband.

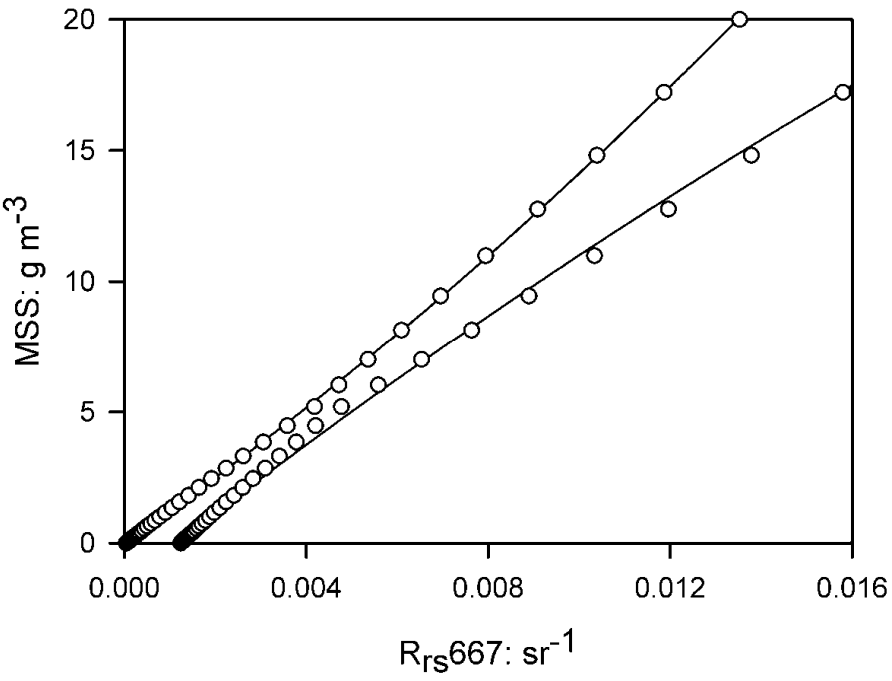

Figure 4.5 Upper and lower boundaries for the MSS values corresponding to a given R_{rs} at 667 nm when CHL and CDOM are simultaneously present in the ranges 0-10 mg m^{-3} and 0-1 m^{-1} respectively. The symbols indicate values calculated by radiative transfer modelling and the lines are best fits of equation (4.4), generated using the coefficients listed in Table 4.2.

Table 4.2 Coefficients for equation (4.4).

Boundary	C1	C2	C3
Upper	1.20×10^4	1214.3	-0.01
Lower	1.10×10^4	1365.2	-1.5

4.6 Validation using in situ measurements

Standard MSS analyses do not distinguish between different classes of mineral particles. Particle populations which are dominated by phytoplankton are known to exhibit a pronounced absorption peak at 676 nm. Conversely, this peak is not present in the absorption spectrum of MSS. Therefore, it is possible to distinguish between particle assemblages dominated by phytoplankton and those by suspended minerals using the ration of particulate absorption measured at 650 nm and 676 nm. Figure

4.6 shows a histogram of the relevant ratio of absorption coefficients averaged over the top 5 m of the water column. The distribution is clearly bimodal, and a threshold figure of 0.8 has been used to classify the stations into two groups. Further analysis showed that stations in Group 1 (phytoplankton dominated) were all located offshore in depths greater than 60 m. Additional evidence suggests group consists predominantly of biogenic minerals and is not resuspended sediment.

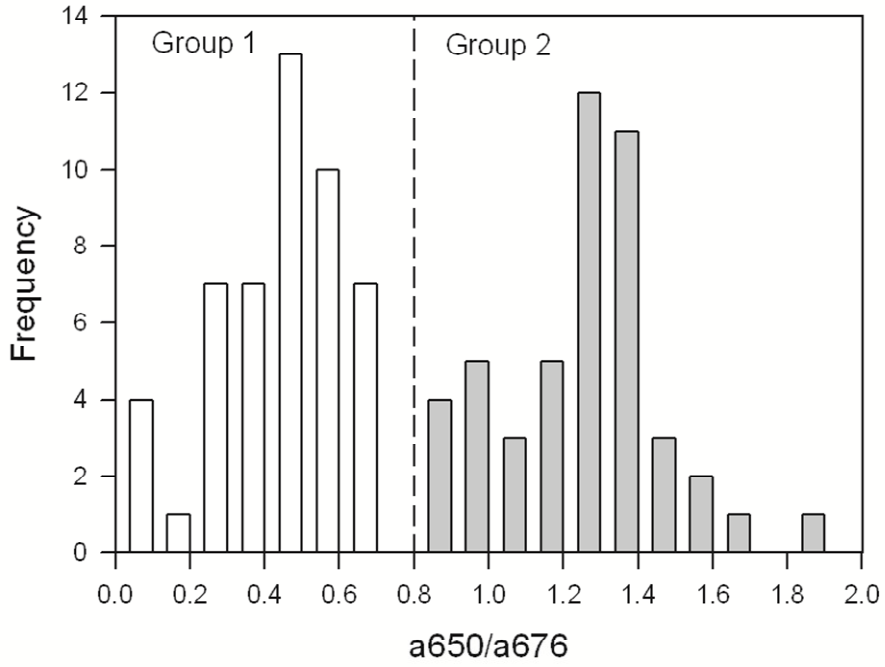

Figure 4.6 Bimodal frequency distribution for the ratio of the non-water absorption coefficients in the 650 nm and 676 nm wavebands measured in situ using the ac-9. The ratio value of 0.8 was used to classify stations as Group 1 (white bars) or Group 2 (grey bars).

The frequency of cloud cover over the Irish Sea makes satellite based validation of this technique difficult. Therefore, results were validated against R_{rs} profile measurements obtained by the Satlantic SPMR. Measurement errors were estimated where duplicate cast or sample analyses existed. These were taken to be the standard deviation of residuals from a least square fit of scatterplots of duplicate measurements and were +/- 0.7 g m^{-3} for MSS and +/- 0.001 sr^{-1} for R_{rs}. Figure 4.7 contains water sample measurements of MSS plotted against SPMR derived $R_{rs}667$

for 120 stations in the Irish Sea. Superimposed on this figure are the upper and lower boundaries derived from the MSS equation. When taking into account the relevant errors, estimated from multiple measurements obtained at stations, approximately 90% of field observations fall within the limits of the proposed MSS boundaries. Points lying outside the limits have $R_{rs}667$ values less than 0.001 sr^{-1} and all fall within the Group 1 stations defined above. Figure 4.7 implies that the boundaries generated by equation (4.4) are effective for mineral particles derived from suspended sediment, but under-estimate the presence of biogenic silica produced by diatoms.

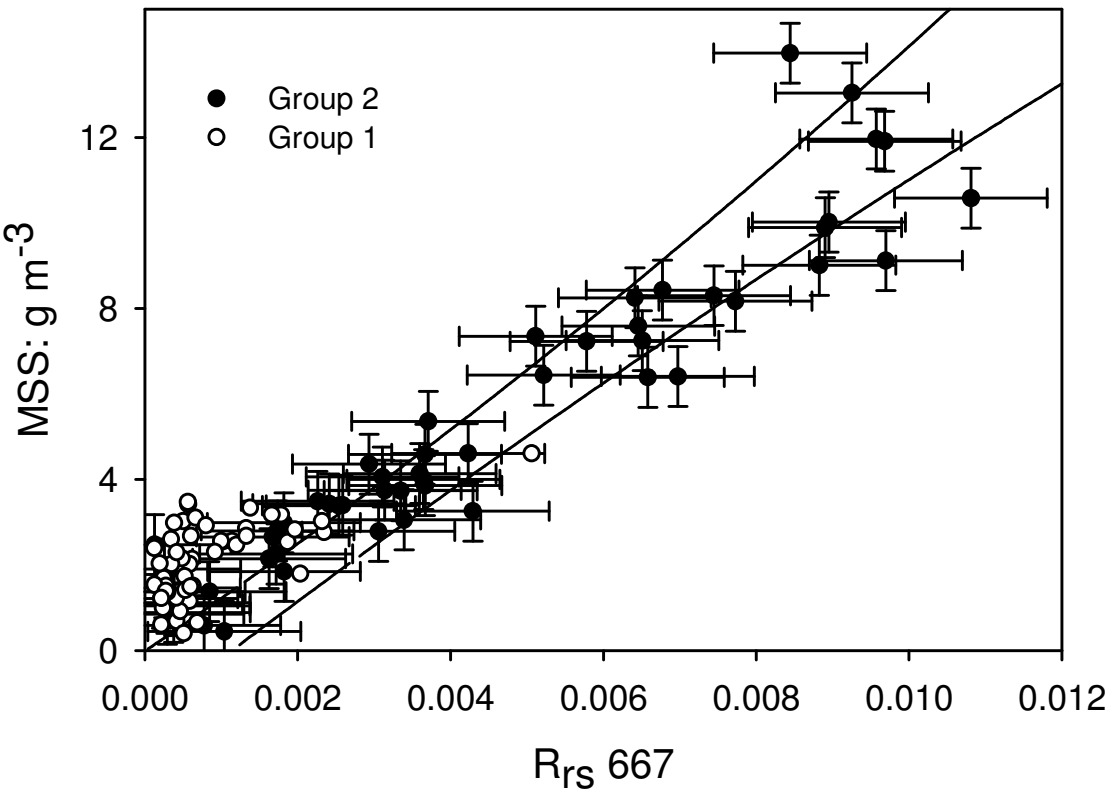

Figure 4.7 MSS determined by gravimetric analysis of near-surface water samples plotted against R_{rs} at 667 nm measured by in-situ radiometry, with estimated errors of observation for both variables. The solid lines indicate the upper and lower MSS limits predicted by radiative transfer modelling for the CHL and CDOM ranges used in Figure 4.5. White symbols indicate those stations classified as Group 1 and black symbols those classified as group 2 in Figure 4.6.

4.7 MSS mapping by satellite remote sensing

A contour map of $R_{rs}667$ generated from a MODIS image of the Irish Sea acquired 2nd May 2007 is shown in Figure 4.8. Transects drawn on Figure 4.8 run west to east, from the open waters of St Georges Channel (point A) into the Bristol Channel (point B) and south to north from point A into the Irish Sea (point C). The upper and lower limits of MSS calculated from equation (4.4) on the assumption that CHL and CDOM concentrations are unknown but fall within the ranges 0-10 mg m^{-3} and 0-1 m^{-1} respectively, are illustrated in Figure 4.9. The transects begin in the clear waters of the Celtic Sea. A steep increase in sediment concentration can be seen at 140 km as the first transect (A to B) enters the turbid inner Bristol Channel. A more gradual increase in MSS is found in transect 2 (A to C), where the location of the Celtic Sea front is indicated by an increase in sediment concentrations at 100 km. This figure shows that it is possible to locate major features and transitions in mineral particle distributions to within a few kilometres in spite of the calculated uncertainties in absolute values, and this capability is potentially important for validating sediment transport models using ocean colour imagery.

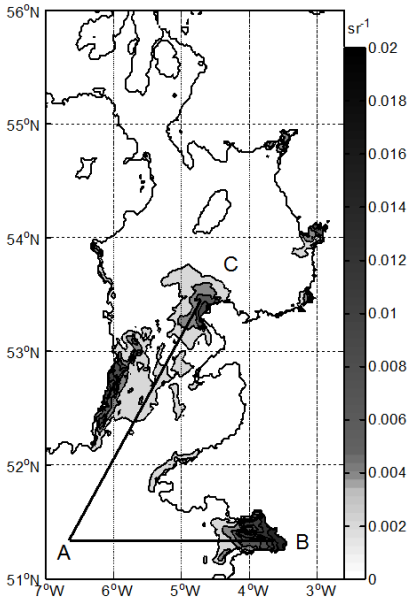

Figure 4.8 Remote sensing reflectance in the 667 nm waveband derived from a MODIS Aqua image acquired on May 2nd 2007, with transects extending from St Georges Channel (A) into the Bristol Channel (B) and the Irish Sea (C).

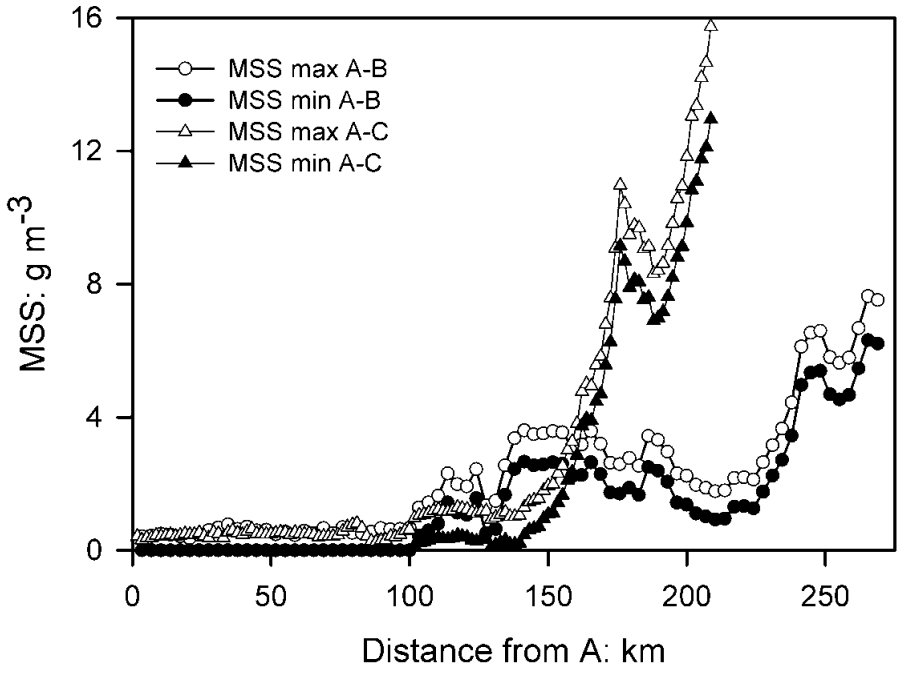

Figure 4.9 Upper and lower boundaries of possible MSS values for the transects drawn on Figure 4.8, on the assumption that CHL and CDOM concentrations are unknown but fall within the ranges 0-10 mg m^{-3} and 0-1 m^{-1} respectively, calculated using equation (4.4).

4.8 Discussion

The detection of low concentrations of MSS in coastal shelf seas is of considerable significance. These areas are subject to the greatest errors associated with concentration retrievals due to the complex composition of constituents contained within the water. Radiance transfer modelling has shown that a single-band algorithm relying on $R_{rs}667$ is an effective quantitative indicator of MSS with a maximum uncertainty of +/- 4 g m^{-3} for concentrations up to 20 g m^{-3}. This is true for areas containing CHL concentrations up to 10 mg m-3 and CDOM to $1m^{-1}$. The hyperbolic form of the MSS vs R_{rs} relationship suggests a non-linear approach is required for concentrations of MSS in excess of 20 g m^{-3}. Field observations measured during several Irish Sea research cruises confirm the existence of an approximate linear relationship between $R_{rs}667$ and concentrations of MSS. However a small number of stations exhibit non-consistent characteristics. One explanation is that a high proportion of the MSS measured at these stations consisted of diatom

frustules rather than suspended sediment. The development of a technique which specifies uncertainty in MSS values in terms of upper and lower boundaries has two advantages. First, it reflects the fact that the uncertainty arises from the composition of the water body being inadequately known as well as simply from errors of observation. Secondly, variable uncertainties can be generated through the seasonal adjustment of equation coefficients. Application of this technique to other regions depends on the degree of spatial variability of the specific backscattering coefficient (b_b*MSS). There is remarkably little published information on this variability and this is a topic which is in urgent need of further study.

Key points from chapter 4

1. In the presence of MSS, the fractional contribution of seawater to total absorption is significantly wavelength dependent and becomes increasingly dominant at red wavelengths. The backscattering contribution by seawater is contrastingly low, meaning total backscattering depends primarily on MSS concentration.

2. The effect of adding MSS to seawater was determined by radiance transfer modelling. A near linear relationship exists between $R_{rs}667$ and MSS concentration up to 20 g m^{-3}. Radiative transfer modelling confirms use of red wavelengths for remote sensing of MSS.

3. Addition of CHL and CDOM to radiance transfer calculations illustrated the effect of other optically significant material (OSM) on the MSS retrieval. The uncertainty in the MSS retrieval varied with OSM values and was best indicated by explicitly stating the range of MSS concentrations that would be associated with a given R_{rs} signal.

4. Validation of the MSS algorithm using in-situ observations shows good agreement with measured values. Boundaries generated by equation (4.4) explain a large portion of the variability observed in the in-situ dataset.

5. MSS distributions in coastal regions can be estimated to a precision of +/- 2.5 g m^{-3} at concentrations of 20 g m^{-3} and +/1.0 g m^{-3} at 5 g m^{-3} provided the concentrations of the other OSM are within the specified range of the model.

6. Application of the algorithm to satellite reflectance data reproduces spatial features commonly observed in the Irish Sea. $R_{rs}667$ is a suitable quantitative indicator of mineral suspended sediment concentration. Analyses in the following chapters are based on observations of Rrs667, with the implied assumption that Rrs can be converted to MSS using equation 4.4.

References

Aldridge, J.N., Kershaw, P., Brown, J., McCubbin, D., Leonard, K.S., Young, E.F., 2003. Transport of plutonium (Pu-239/240) and caesium (Cs-137) in the Irish Sea: comparison between observations and results from sediment and contaminant transport modelling. CONTINENTAL SHELF RESEARCH, 23 (9), 869-899.

Binding, C.E., Bowers, D.G., Mitchelson-Jacob, E.G., 2003. An algorithm for the retrieval of suspended sediment concentrations in the Irish Sea from SeaWiFS ocean colour satellite imagery. INTERNATIONAL JOURNAL OF REMOTE SENSING, 24 (19), 3791-3806.

Binding, C.E., Bowers, D.G., Mitchelson-Jacob, E.G., 2005. Estimating suspended sediment concentrations from ocean colour measurements in moderately turbid waters; the impact of variable particle scattering properties. REMOTE SENSING OF ENVIRONMENT, 94 (3), 373-383.

Charlesworth, M.E., Service, M., Gibson, C.E., 2006. The distribution and transport of Sellafield derived Cs-137 and Am-241 to western Irish Sea sediments. SCIENCE OF THE TOTAL ENVIRONMENT, 354 (1), 83-92.

D'Sa, E.J., Ko, D.S., 2008. Short-term influences on suspended particulate matter distribution in the northern Gulf of Mexico: Satellite and model observations. SENSORS, 8 (7), 4249-4264.

Doerffer, R., Schiller, H., 2007. The MERIS case 2 water algorithm. INTERNATIONAL JOURNAL OF REMOTE SENSING, 28 (3-4), 517-535.

Fournier, G.R., Forand, J.L., 1994. Analytic phase function for ocean water. OCEAN OPTICS XII, 2258, 194-201.

Hommersom, A., Wernand, M.R., Peters, S., de Boer, J., 2010. A review on substances and processes relevant for optical remote sensing of extremely turbid marine areas, with a focus on the Wadden Sea. HELGOLAND MARINE RESEARCH, 64 (2), 75-92.

Kirk, J. T. O., 1994. Light and photosynthesis in aquatic ecosystems. 2nd edition. Cambridge University Press.

Kuchinke, C.P., Gordon, H.R., Franz, B.A., 2009. Spectral optimization for constituent retrieval in Case 2 waters I: Implementation and performance. REMOTE SENSING OF ENVIRONMENT, 113 (3), 571-587.

Lahet, F., Stramski, D. , 2010. MODIS imagery of turbid plumes in San Diego coastal waters during rainstorm events. REMOTE SENSING OF ENVIRONMENT, 114 (2), 332-344.

Lohrenz, S.E., Cai, W.J., Chen, X.G., Tuel, M., 2008. Satellite assessment of bio-optical properties of northern Gulf of Mexico coastal waters following hurricanes Katrina and Rita. SENSORS, 8 (7), 4135-4150.

McKee, D., Cunningham, A., Dudek, A., 2007. Optical water type discrimination and tuning remote sensing band-ratio algorithms: Application to retrieval of chlorophyll and K-d(490) in the Irish and Celtic Seas. ESTUARINE COASTAL AND SHELF SCIENCE, 73 (3-4), 827-834.

Mobley, C. D., 1999. Estimation of the remote-sensing reflectance from above-surface measurements. APPLIED OPTICS, 38, 7442-7455.

Nechad, B., Ruddick, K.G. and Park, Y., 2010. Calibration and validation of a generic multisensor algorithm for mapping of total suspended matter in turbid waters. REMOTE SENSING OF ENVIRONMENT, 114 (4), 854-866.

Sathyendranath, S., 2000. Remote sensing of ocean colour in coastal, and other optically-complex, waters. Reports of the Ocean Colour Coordinating Group, No. 3, IOCCG, Dartmouth, Canada.

Tilstone, G.H., Smyth, T.J., Gowen, R.J., Martinez-Vicente, V., Groom, S.B., 2005. Inherent optical properties of the Irish Sea and their effect on satellite primary production algorithms. JOURNAL OF PLANKTON RESEARCH, 27 (11), 1127-1148.

Warrick, J.A., DiGiacomo, P.M., Welsberg, S.B., Nezlin, N.P., Mengel, M., Jones, B.H., Ohlmann, J.C., Washburn, L., Terrill, E.J., Farnsworth, K.L., 2007. River plume patterns and dynamics within the Southern California Bight. CONTINENTAL SHELF RESEARCH, 27 (19), 2427-2448.

Yan, Z.Z., Tang, D.L., 2009. Changes in suspended sediments associated with 2004 Indian Ocean tsunami. ADVANCES IN SPACE RESEARCH, 43 (1), 89-95.

Chapter 5

Temporal and spatial patterns of reflectance variability in the Irish Sea

Summary

This chapter considers the feasibility of developing an objective classification scheme from $R_{rs}667$ variability suitable for defining hydrological features in the Irish Sea. Time series constructed from 181 MODIS Aqua images were used to analyse seasonal and spatial patterns of variation in $R_{rs}667$, and by implication MSS. Results from autocorrelation analysis showed annual periodicity in all areas except the Bristol Channel. The spatial distribution in time series statistical parameters was used to classify the region into locations containing high and low reflectance variance. Increased values of variance occurred in shallow waters of the region of interest. A further classification scheme was devised by considering the distribution of individual time series around their mean values. By calculating the time spent below the mean reflectance the region can be classified into locations containing distinct hydrological dynamics. This technique was improved by determining the period spent below the Irish Sea spatial $R_{rs}667$ minimum value (= 9.148×10^{-3} sr^{-1}). Results accurately replicate seasonal sediment patterns in the Irish Sea. A thorough understanding of reflectance variability offers unique insights into the mechanisms driving physical processes.

5.1 Introduction

Mineral suspended solids (MSS) are the inorganic fraction of the total particulate matter suspended in coastal shelf seas. These cohesive or non-cohesive fine sediments include clays, silts and muds with particle diameters ranging from less than 0.01 mm to 0.1 mm. MSS plays an important role in the shelf sea ecosystem. As an efficient scatterer of light, mineral particles increase the magnitude of water leaving radiance returned to space, limiting the penetration of light within the upper layers of the ocean (Kirk, 1994). Accurate representation of MSS concentrations

from satellite imagery is therefore crucial for understanding the biological and physical dynamics of optically complex shelf seas (Robinson, 2008).

In principle, ocean colour observations acquired by means of satellite radiometry provide unparalleled insight into the dynamics of marine sediments in shelf seas due to the frequency of synoptic measurements. Information on short and long scale events can be extracted from an archive containing 30 years of satellite data. Bowers et al. (1998) and Eleveld et al. (2008) used satellite remote sensing to estimate seasonal variations in suspended sediment in the Irish and North Seas respectively, whilst Chen et al. (2007) considered monthly changes of turbidity in Tampa Bay. More recently Nechad et al. (2010) evaluated algorithm performance by comparing time series of sediment concentrations in Belgian waters derived from different satellite sensors. This study focuses on the application of time series analysis to reflectance signals measured over the Irish and Celtic Seas from July 2005 until July 2010. By considering the spatial and temporal variability of MODIS remote sensing reflectance measured at 667 nm, an objective classification scheme is derived for the hydrodynamically diverse geographical regions of the Irish Sea.

5.2 The test site

The Irish Sea is a semi-enclosed basin situated between the islands of Great Britain and Ireland. This area contains various interesting hydrodynamic features, including seasonal thermal stratification fronts and permanent salinity fronts. There are two well documented regions of persistent seasonal stratification located in the north west Irish Sea (Gowen et al., 1995 and Xing et al., 2001) and south at the Celtic Sea border (Brown et al., 2003). In both areas, stratification appears to correlate with the existence of low tidal currents (Bowers et al., 2002). The eastern Irish Sea contains a complex body of water which is subject to salinity stratification owing to the input of fresh water from three major rivers (Verspecht et al., 2009). Regions of high tidal energy (current velocity > 1.5 m s^{-1}) can be found in various locations such as the point north of Anglesey, east of Wicklow Head and the Bristol Channel (Simpson & Hunter, 1974).

There are two main sources of suspended sediment in the Irish Sea, those contributed by estuaries and rivers and sediment eroded as a result of shear friction on the sea floor. The contribution by estuaries and rivers only affects waters a small distance from the source. Sediment in suspension is transported throughout the water column by turbulent kinetic energy. A map of the Irish Sea marine landscape is shown in Figure 5.1. The majority of the region is covered by gravel and sand, with particle diameters greater than 0.1 mm. There are two muddy banks found at the north-west and north-east of the Irish Sea. A muddy section of the Bristol Channel may account for high MSS concentrations measured in this area. Small mud banks found close to Wicklow Head and North Anglesey may explain high concentrations measured at these locations, however rock formations suggest a more complex hydrodynamic system is present at North Anglesey (Bowers et al., 2005).

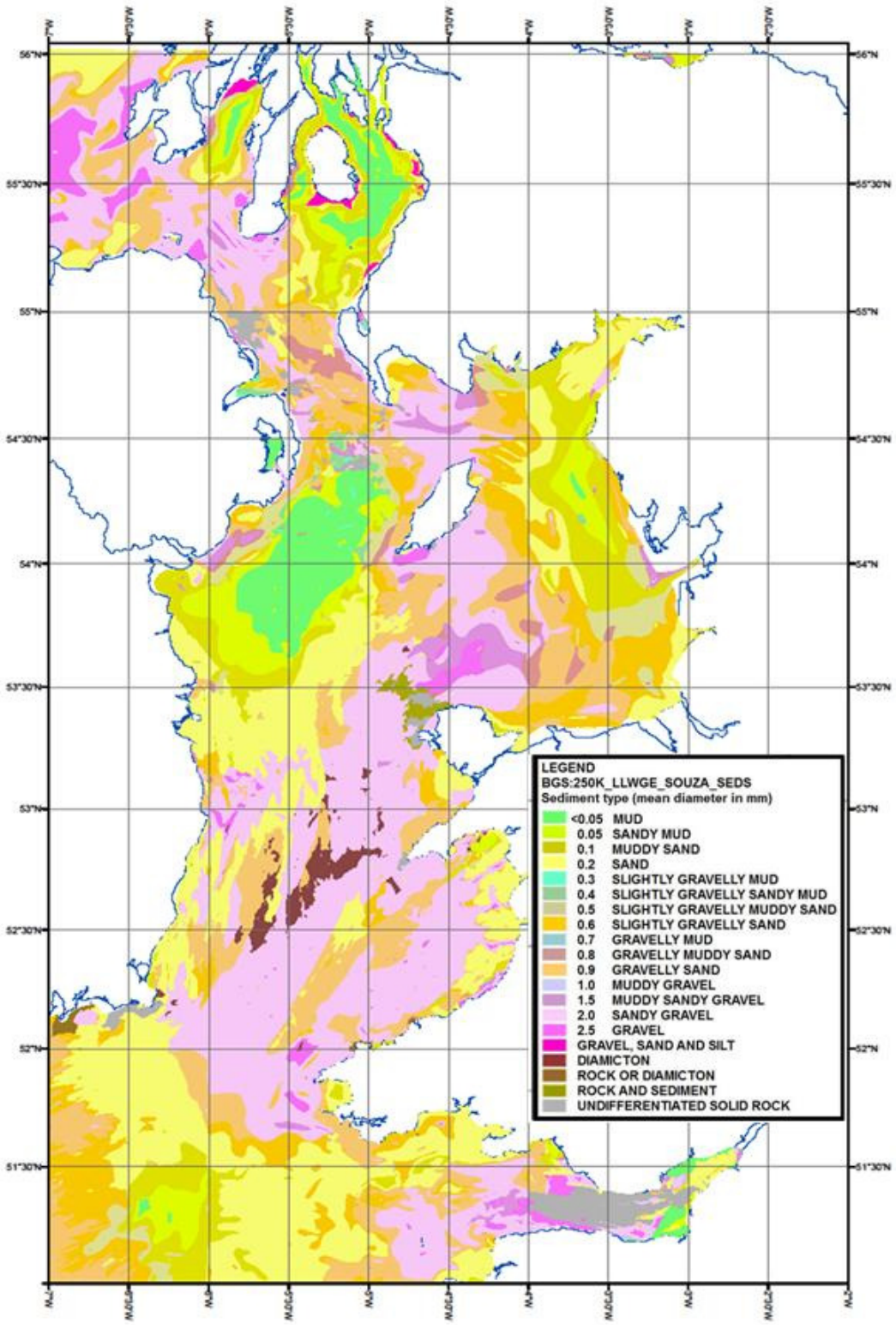

Figure 5.1 Marine landscape showing types and properties of sediments in the Irish Sea. MSS sediments are defined as particles < 0.1 mm (sand grain dimension). Image courtesy of National Oceanographic Centre, Liverpool.

5.3 MSS concentration from remote sensing reflectance

Commonly, algorithms used to derive sediment concentrations from reflectance spectra are developed using empirical relationships. These techniques can generate reasonable results but their reliance on a priori knowledge of the presence of other optically significant constituents prevents accurate representation of retrieval errors. In highly turbid areas (MSS > 20 g m^{-3}), Doxaran et al. (2003) demonstrated the effectiveness of estimating sediment concentrations from ratios of remote sensing reflectance. Single band algorithms exist for less turbid waters which rely on the same technique. There is some agreement in the research community that reflectance measured at red wavelengths is a useful quantitative indicator of sediment concentration (Binding et al., 2003, Nechad et al., 2010, Ouillon et al., 2008). The existence of a approximately linear relationship between R_{rs} at red wavelengths (667 nm, 678 nm) and concentrations of MSS less than 20 g m^{-3} , explained in detail in chapter 4, can be attributed to the b_b/a ratio. At red wavelengths, a is dominated by absorption due to seawater whilst b_b is determined predominantly by the MSS contribution. Consequently b_b increases significantly with increasing concentrations of MSS, whereas a remains relatively unchanged. Saturation of the curve becomes significant where MSS concentrations are in excess of 20 g m^{-3}.

Concentrations of MSS were obtained from measurements of $R_{rs}667$ (sr^{-1}) using the equation;

$$MSS_{(u,l)} = C_1(u,l) \times (R_{rs}667)^2 + C_2(u,l) \times (R_{rs}667) + C_3(u,l) \qquad (5.1)$$

with coefficients (C_1, C_2, C_3) for the upper and lower boundaries (u,l) listed in Table 4.3 . A full description of the derivation of this formula can be found in chapter 4.

5.4 Satellite data

Irish Sea $R_{rs}667$ signals measured by the MODIS Aqua radiometer were obtained from GSFC Ocean Color Web (section 2.1). Over 180 partially cloud free images were extracted from the archive spanning the time period July 2005 until July 2010. Data were processed using SeaDAS software version 6.1, using the default 2-band aerosol model with iterative NIR correction. Level 2 (R_{rs}) data was mapped to an equidistant cylindrical projection and further processing carried out in Matlab.

i) Overall patterns of reflectivity

Marked temporal and spatial variations in reflectance measured at red wavelengths are frequently observed in the Irish Sea. For example, figure 5.2 contains daily images of $R_{rs}667$ measured on a) 29 January 2006, b) 02 May 2007, c) 06 August 2005, and d) 08 October 2008. The obvious existence of seasonal variability suggests that the reflectance in this region may be temporally correlated with physical processes. Increased insolation during spring and summer promotes stratification of the water column in the Celtic Sea and north-west Irish Sea, allowing sediment to sink out of surface waters. This hydrological event is recognisable in the reflectance patterns of the May and August MODIS images, where reduced R_{rs} signals are found in stratified areas (section 1.3). A further reduction in R_{rs} across the majority of the Irish Sea in August suggests sediment is settling from the surface of the water column in both mixed and stratified regimes. This may be attributable to prolonged periods of calm weather. The January image, which is representative of winter conditions, shows a general increase in the background reflectance signal in all areas.

ii) Spatial features

Reflectance maxima remain spatially consistent in each of these images, with the brightest signals appearing in the Bristol Channel, North Anglesey and Wicklow Head (locations indicated in Figure 1.3). These geographical locations are subject to the greatest tidal current velocities in the Irish Sea, indicating a correlation between tidal stirring and remote sensing reflectance exists (Bowers et al., 1998). However, the tidal current velocities, which remain relatively unchanged temporally on a monthly scale, cannot explain the seasonal variations in R_{rs} observed in the MODIS satellite imagery. Therefore an alternative physical process must be influencing seasonal patterns of reflectance.

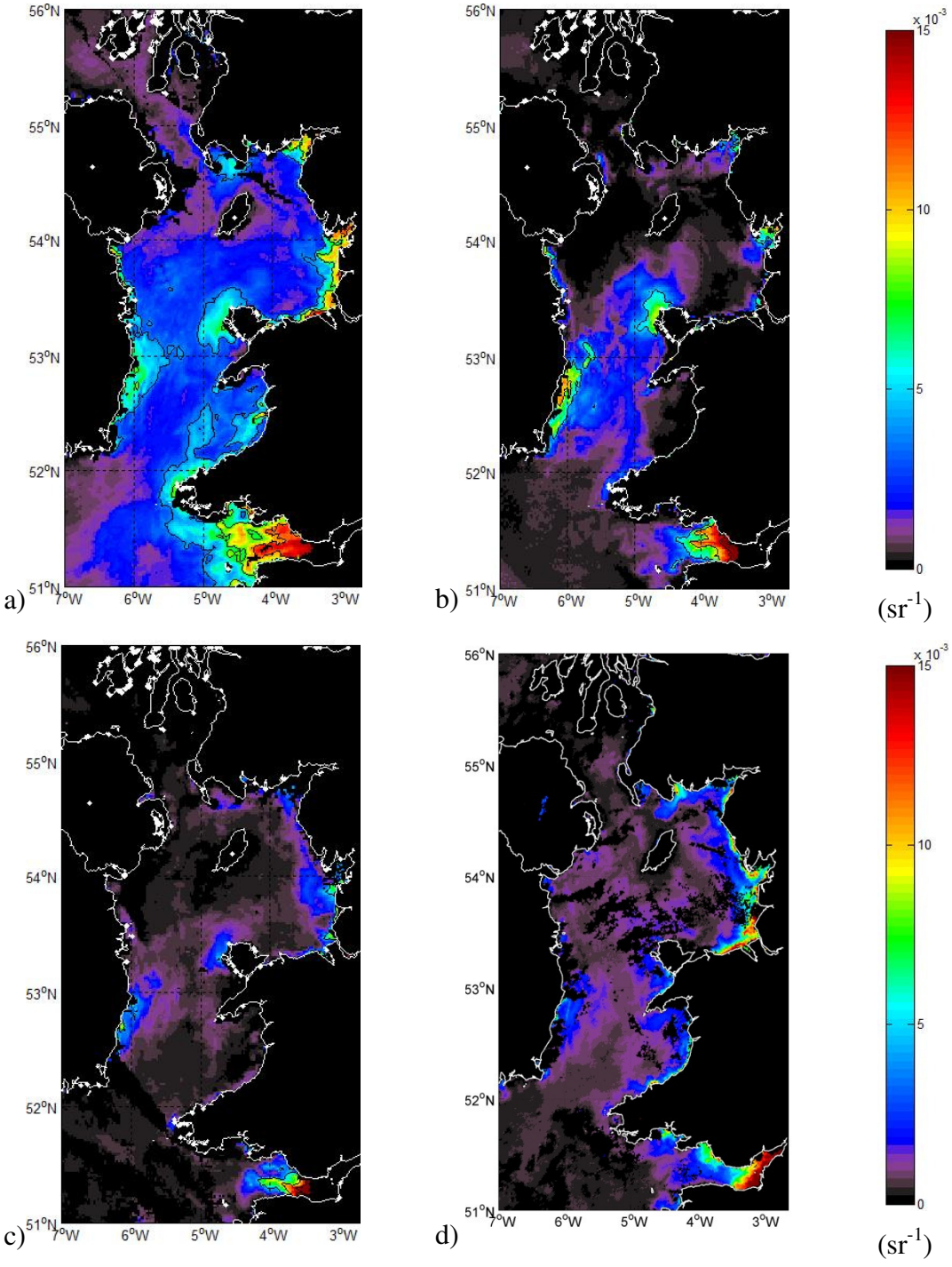

Figure 5.2 $R_{rs}667$ (sr^{-1}) measured by MODIS instrument on a) 29 January 2006, b) 03 May 2007, c) 06 August 2005 and d) 08 October 2008. Level 0 ocean colour data obtained from Goddard Space Flight Centre and processed using SeaDAS version 6.1 image processing software.

5.5 Time series processing

As a first step, MODIS $R_{rs}667$ data were projected onto a reduced resolution grid containing 29 x 49 grid cells. New pixel values, corresponding to a geographical area of approximately 12 km x 14 km, were generated by averaging all local R_{rs} signals. If more than 50 percent of the original values located in a cell were either cloud or negative pixels, no value was returned. The resulting data set consisted of 1421 individual time series covering the full extent of the Irish and north Celtic Seas. Each time series was linearly interpolated at 10 day increments to correct for missing data and inconsistent sample spacing. Next, noise was removed from the interpolated time series by twice applying a moving average smoother with an averaging window of 7 points. The existence of a potential trend was also considered when reprocessing the time series. An extra processing step involved linearly detrending the data and investigating the response from the linear contribution. The detrending routine subtracts the mean value from the data to redistribute points around y = 0 axis. A histogram of detrending gradients (Figure 5.3) showing a mode gradient of zero indicates no linear trend exists for this data set. The mean value was subtracted from the detrended time series so that it fluctuates around the y = 0 axis. Finally, the detrended time series was normalised by its mean maximum value. The data generated at each processing stage will be referred to as original, interpolated, smoothed, detrended and normalised respectively. A visual explanation of the processing stages is shown in Figure 5.4.

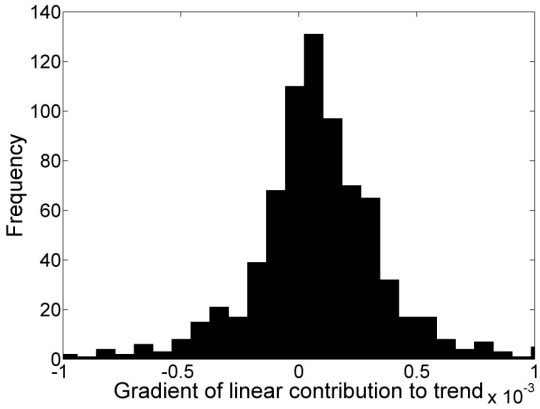

Figure 5.3 Gradient of linear contribution to the seasonal trend. Values close to zero indicate no trend exists in the Irish Sea time series data.

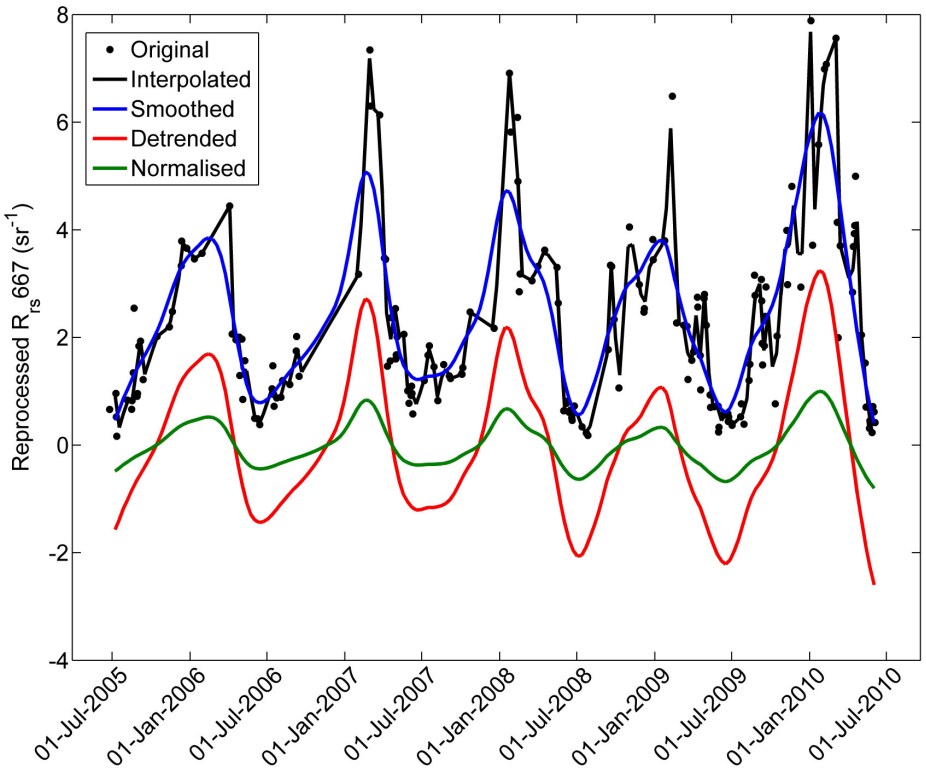

Figure 5.4 Manipulation of $R_{rs}667$ through time series reprocessing for a station location in the central Irish Sea.

5.6 Time series characteristics

Initial inspection of time series plots for several locations in the Irish Sea highlights the spatial and temporal variability of $R_{rs}667$ in this area. Sample normalised time series for three locations is shown in Figure 5.5 b) with corresponding grid locations shown in a). Asymmetric seasonal cycles are present in each of the grid cell examples. Therefore the reflectance variability cannot be accurately represented by fitting a sinusoidal function to the data. Large variations in amplitude and mean values are also noted. The time of maximum reflectance varies from mid December to mid February. Furthermore, there is no spatial link connecting the occurrence of the maxima. For example, an early peak in the Celtic Sea does not correlate to an early peak in the north Irish Sea.

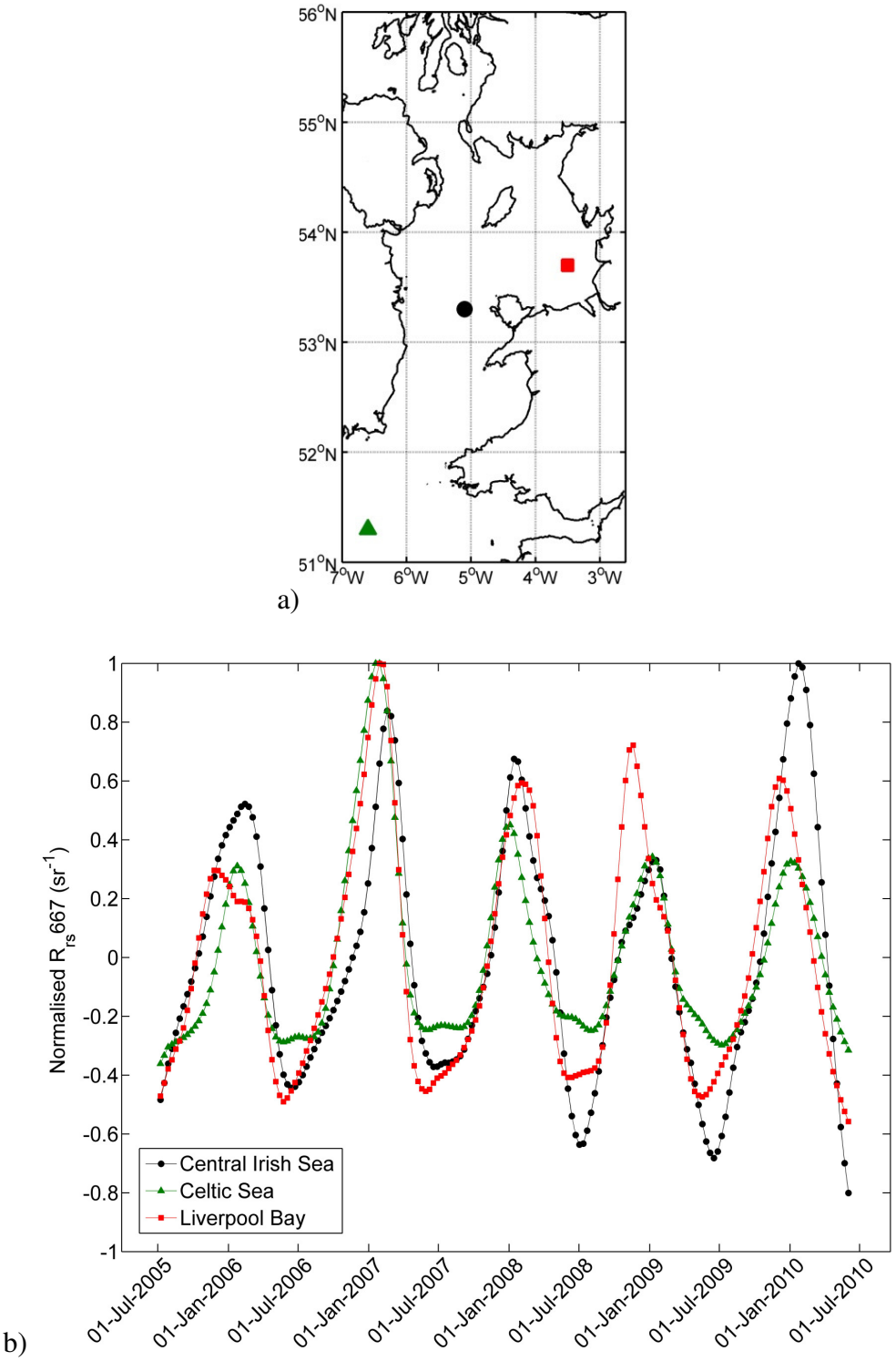

Figure 5.5 b) Normalised time series for three locations in the Irish Sea shown in a). An asymmetric pattern exists for all functions.

5.7 Periodic variability in the reflectance signal

Autocorrelation analysis is a statistical technique which describes how a signal is cross-correlated with itself as a function of the time separation. Statistically the autocorrelation function, $\rho(k)$, for a stationary, (mean and variance are time independent) random process is defined as;

$$\rho(k) = \frac{r(k)}{r(0)} = \frac{r(k)}{\sigma_x^2} \tag{5.2}$$

where σ_x is the variance of series x and $r(k)$ is the covariance between two observations, x_n and x_{n+k};

$$r(k) = E\left[(x_n - \mu)(x_{n+k} - \mu)\right] \tag{5.3}$$

Here, E, is the expectation operator. The autocorrelation coefficient has a value of 1 when observations are completely correlated and -1 when out of phase. By definition, at zero lag time every function has an autocorrelation coefficient equal to 1. If periodicity exists in a data set, the location of the second peak in a correlogram identifies the duration of the period, an example of which is shown in Figure 5.6. This figure contains two correlograms for time series measured at different locations in the Irish Sea. Figure 5.6 a) consists of a series of peaks which indicates some form of periodicity exists in the relevant location. Contrastingly, the correlogram presented in Figure 5.6 b) has one prominent peak at zero lag time then a series of randomly spaced peaks, suggesting this time series is non-periodic. Consistency in the time lags calculated between peaks one to three distinguishes periodic pixels. Application of autocorrelation analysis to the Irish Sea detrended time series has demonstrated annual periodicity in $R_{rs}667$ variability for the majority of the test site, as shown in Figure 5.7. Furthermore, pixels which exhibit non-annually periodic characteristics are found mainly in the Bristol Channel and at coastal locations corresponding to river inlets.

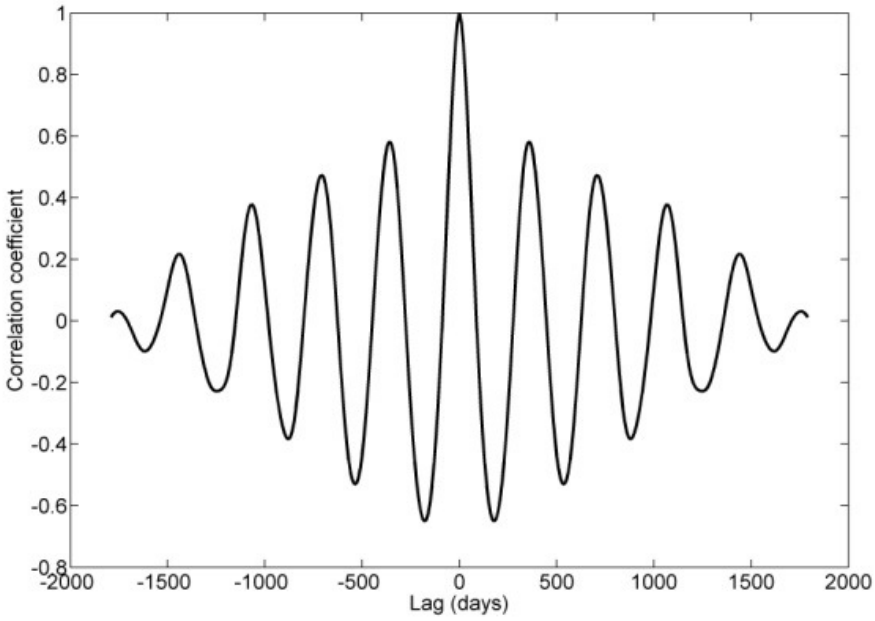

a)

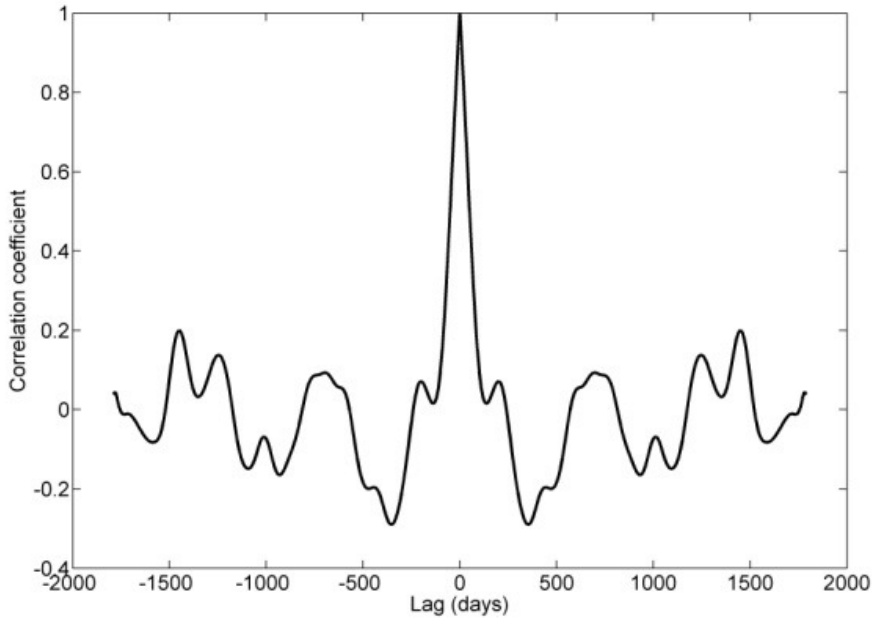

b)

Figure 5.6 Correlogram for periodic a) and non-periodic b) time series from the central Irish Sea (a) and the Bristol Channel (b). The location of the second peak in a) indentifies the period in days.

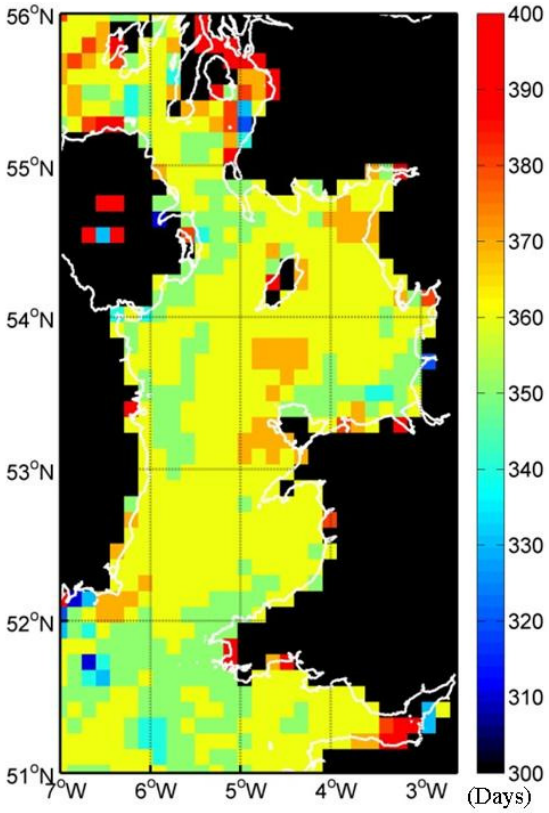

Figure 5.7 Irish Sea periodicity as determined by autocorrelation analysis. Pixels highlighted in red are non-periodic. The colour bar shows length of period in days. The majority of pixels exhibit approximately annual periodicity.

5.8 Objective classification scheme for the different regions of the Irish Sea

Spatial variations were analysed by generating time series statistics for each grid cell. As a first step, the image was characterised by four main parameters; detrended time series variance, mean maximum R_{rs} signal for each detrended time series, average minimum value for every time series and the smoothed time series mean (Figure 5.8). Features in the image of the spatial distribution on the statistical parameters correspond to geographical regions of interest in the Irish Sea.

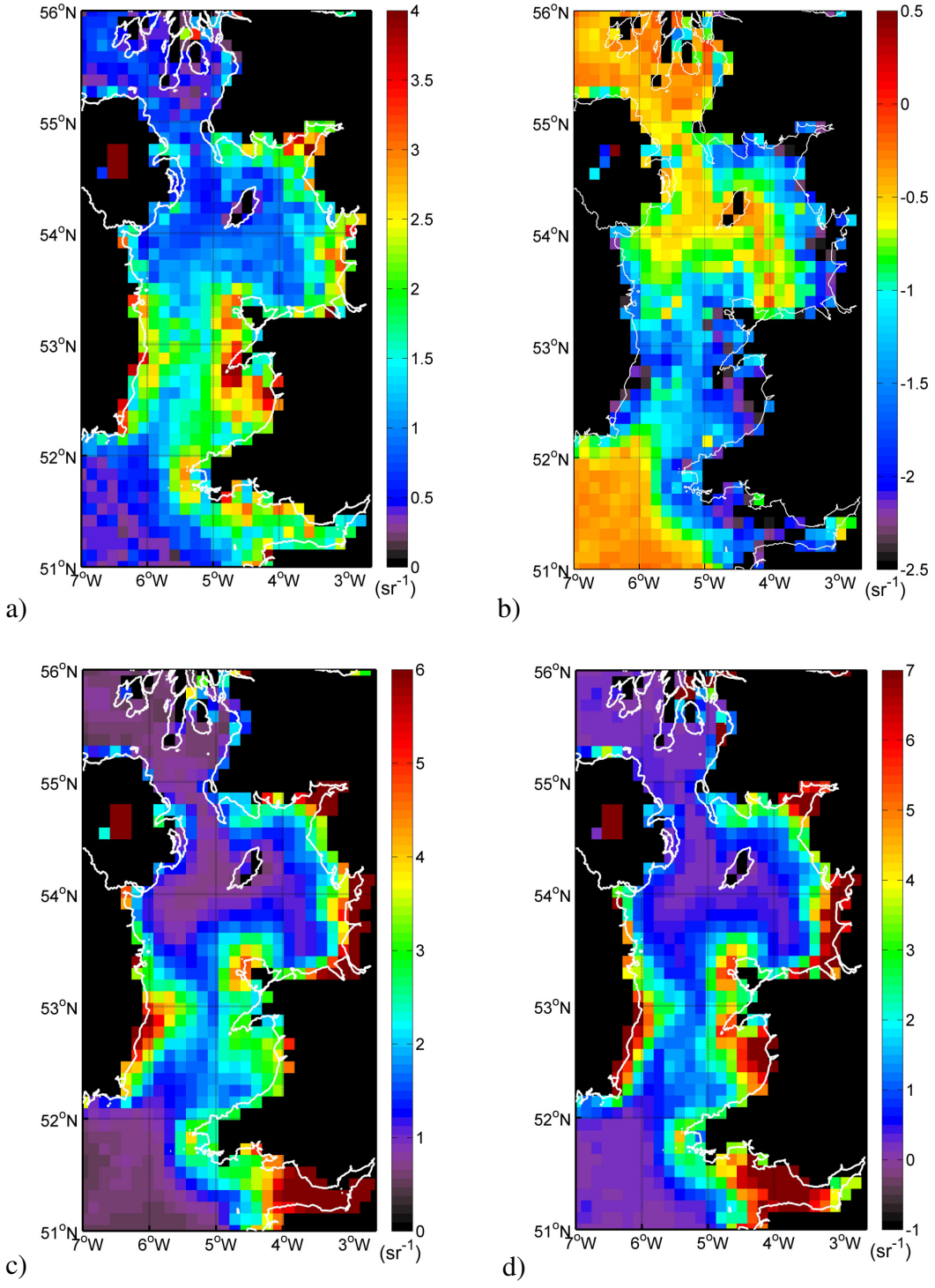

Figure 5.8 Maps of a) average maximum detrended $R_{rs}667$, b) average minimum detrended $R_{rs}667$, c) average smoothed $R_{rs}667$ and d) time series variance, (sr^{-1}). These parameters can be used as a preliminary classification scheme for indentifying geographical regions in the Irish Sea.

5.8.1 Reflectance variance classification

The area can be divided into patches containing high and low variance. If a time series is defined as having high variance, the difference between the seasonal minima and maxima is large. A threshold variance of 3 sr^{-1} was used to classify the region into high and low variance regimes (Figure 5.9). Geographical locations for this classification are illustrated in Figure 5.10 where black and white pixels occur in high and low variance regimes respectively. High variance is assigned to pixels in shallow waters, suggesting these areas are most susceptible to seasonal processes such as wind driven currents. Contrastingly, low variance values can be found in deeper parts of the Irish Sea where insolation is the only external seasonal change affecting the condition of the water column.

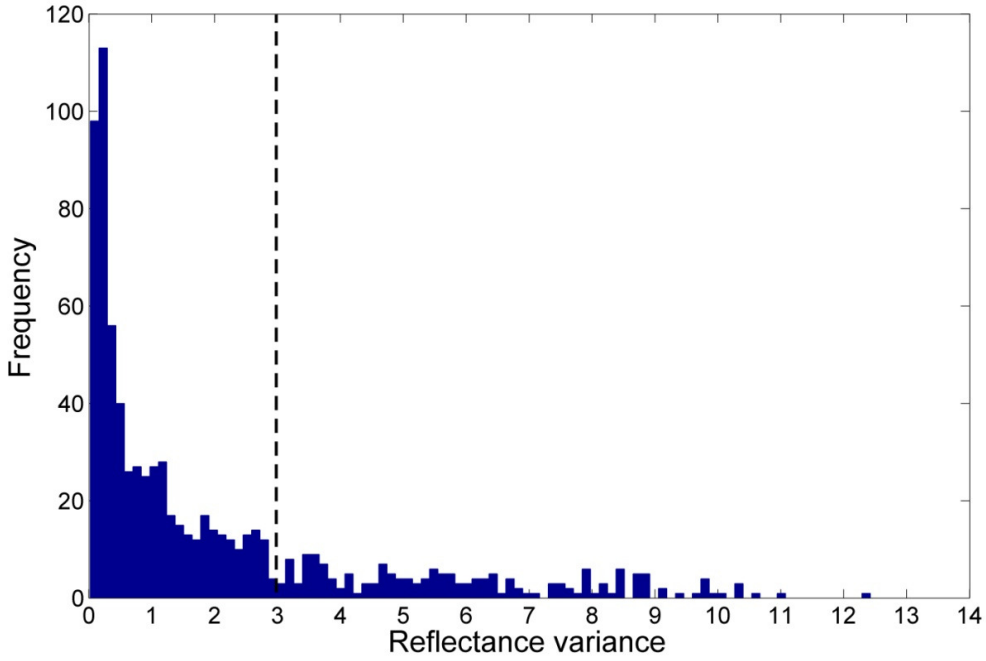

Figure 5.9 Histogram of reflectance variance showing classification threshold.

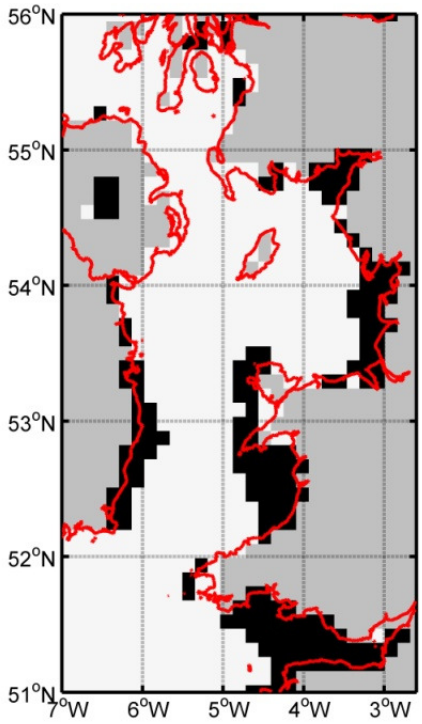

Figure 5.10 Classification of reflectance variance into high (black pixels) and low (white pixels) regimes. These classified regions will be considered individually in subsequent chapters.

5.9 Clarification rate

A noticeable feature of $R_{rs}667$, and by implication sediment, variability in the Irish Sea is the rate at which different regions clarify. Comparison of detrended time series extracted from two locations highlights the difference between waveforms (Figure 5.11). For the Celtic Sea time series, the reflectance signal decreases at a greater rate than that of the central Irish Sea, i.e. the reflectance signal falls below the mean value temporally earlier in the Celtic Sea time series. This suggests this region clarifies relatively quicker. Moreover, $R_{rs}667$ values generally recover in the Irish Sea before the Celtic Sea, meaning the central Irish Sea becomes more turbid earlier in the season. This translates as different roots or x-axis crossing points shown as coloured crosses on the detrended time series plot (Figure 5.11). The average time difference between the down to up crossing points provides temporal information on the stage of the clarification cycle. This is essentially the period of the year in which

reflectance lies below the mean value. It is possible to develop a classification scheme relating the difference in time to geographical regions with specific hydrological features in the Irish Sea. The product of this technique is the time $R_{rs}667$ spends below the pixel average for each individual grid cell. A contour of this parameter is shown in Figure 5.12. Relevant features such as known regions of stratification are identifiable on this map.

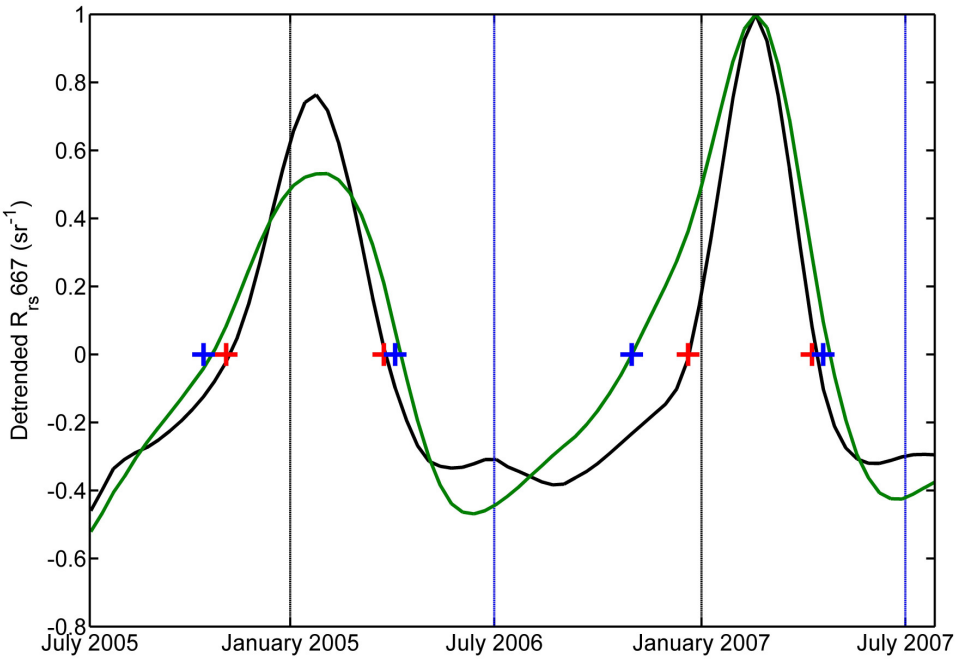

Figure 5.11 Crossing points for a Celtic Sea detrended time series (red crosses and black line) and a central Irish Sea time series (blue crosses with green line) for two years of the time series. Red points cross the y=0 axis before the blue when reducing from the maximum value, and appear after the blue when on the increasing slope.

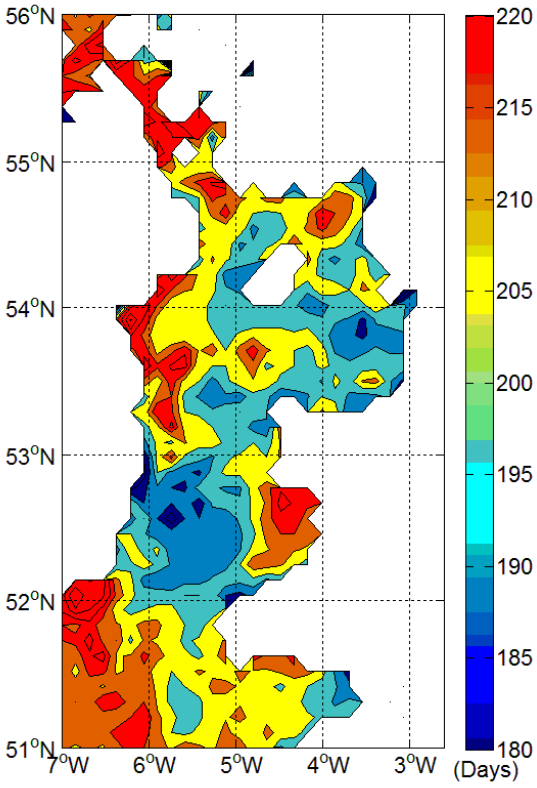

Figure 5.12 Classification scheme based on normalised time series. The contour levels indicate the time spent below the time series mean on a pixel by pixel basis.

The classification scheme can be improved by considering the time series distribution around an alternative value. The Irish Sea spatially averaged minimum $R_{rs}667$ was calculated by averaging the mean detrended time series minima for each individual grid cell located within the boundaries of the Irish Sea. This number, which can also be described as the Irish Sea mean background level of $R_{rs}667$, is equal to 9.148 x 10^{-3} sr^{-1}. The duration below the spatial minima threshold was determined by calculating the time difference between down to up crossing points. Results are shown in Figure 5.13. Each contour level defines a specific duration below the Irish Sea mean $R_{rs}667$ background level. The contour can be used as a predictor of how clear/turbid the region should be at various times of the year. This is a useful device suitable for the classification of water regimes in the Irish Sea.

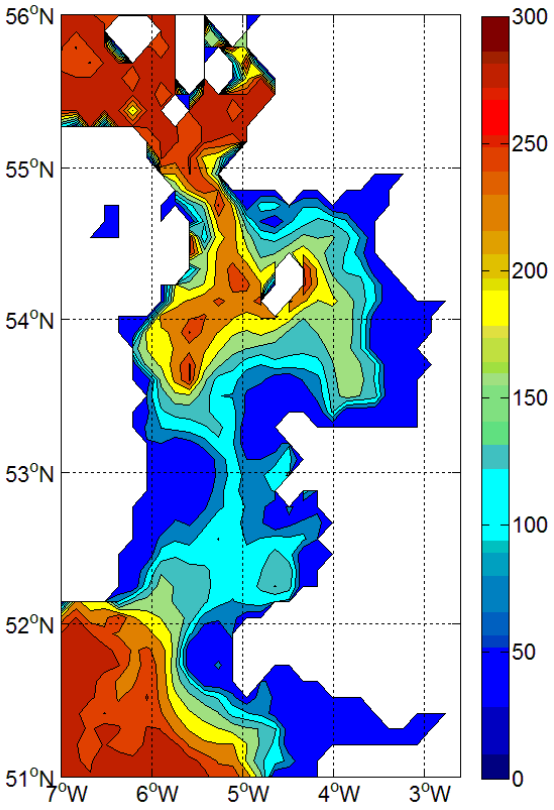

Figure 5.13 Classification scheme from distribution of normalised time series around the Irish Sea average minimum value. The contour levels indicate the time (days) spent below threshold value of $R_{rs}667$ (= 9.148 x10^{-3} sr^{-1}).

5.10 Discussion

Using $R_{rs}667$ as a quantitative indicator of MSS, the spatial and temporal variability of sediment in the Irish Sea was investigated. The existence of seasonal variability in the R_{rs} signal indicated that reflectance was spatially correlated with physical processes. Over 1000 individual time series covering the extent of the Irish Sea were generated from MODIS satellite images. The time series exhibited asymmetric properties, contrary to results published by Bowers et al. (1998) where a sine function was used to best represent the data set. A detrending routine applied to the time series data set demonstrated that no linear trend in $R_{rs}667$ variability exists in this area. However, strong periodic cycles were found at the majority of grid sites. Application of autocorrelation analysis to each time series produced periodic cycles of approximately 365 days. Annual periodicity was demonstrated in all regions

except the Bristol Channel. Here, $R_{rs}667$ signals remained consistently high suggesting reflectance had little or no response to seasonal processes. The variance of the reflectance time series was used as a feature extractor, where high and low values are separated into 2 groups covering identifiable geographical regions. High variance pixels were found in shallow regimes. These areas are subject to the additional external effects of wind driven currents and insolation. This may account for an increased variance in shallow waters. A second group was classified as low variance, occurring mainly in deeper waters (>50 m). Waves have an oscillatory velocity on the seafloor in water depths up to approximately 10 times the wave height (Whitehouse et al., 2000). Therefore, in these deeper sections of the Irish Sea, the only external seasonal process influencing the variability of suspended sediment is insolation. This may explain the existence of decreased variance as a reduction in energy input from external factors may dampen the pattern of seasonal variability. The hydrodynamics of each statistically different group shall be considered separately in the following chapters (chapters 6 and 7). In order to classify the region further, the distribution of time series data around its temporal mean was investigated. More precisely, the total time spent below the mean value characterised the degree of sediment clarification on a pixel by pixel basis. A contour map of the result acts as a simple predictor of sediment settling periods. This technique applied to any sea where time series data exists will classify regions based on their clearing characteristics. By incorporating local sediment statistics, an improved classification scheme was developed, which involved calculating the time spent below the Irish Sea mean background $R_{rs}667$ of 9.148×10^{-3} sr^{-1}. The more detailed contour map accurately replicates sediment patterns in the Irish Sea.

Key points from chapter 5

1. Consolidation of MODIS Aqua reflectance generates time series covering the extent of the Irish Sea. Applying a reprocessing routine which includes linear interpolation of data to specified increments fills the gaps of missing data. This makes it possible to reconstruct temporal events using the available series.

2. The reprocessing stages also indicate no linear trend exists in the reflectance variability. Furthermore, asymmetry in the seasonal cycle suggests variability cannot be represented by a sinusoidal wave.

3. Through autocorrelation analysis, annual periodicity was demonstrated in all regions of the Irish and north Celtic Seas, except the Bristol Channel.

4. Known hydrological features are highlighted in regional reflectance statistics, such as average minimum or mean reflectance. Reflectance variance can be used as an objective classification scheme.

5. The region was subsequently divided into geographical locations of high and low reflectance variance. High reflectance regions correspond mainly to shallow coastal areas, whilst low variance is observed in deeper parts of the Irish Sea. The hydrodynamics of each classified group shall be considered in the following chapters.

6. A further classification scheme was developed by considering the distribution of time series reflectance around their mean values.

References

Binding, C.E., Bowers, D.G., Mitchelson-Jacob, E.G., 2003. An algorithm for the retrieval of suspended sediment concentrations in the Irish Sea from SeaWiFS ocean colour satellite imagery. INTERNATIONAL JOURNAL OF REMOTE SENSING, 24 (19), 3791-3806.

Bowers, D.G., Boudjelas, S., Harker, G.E.L., 1998. The distribution of fine suspended sediments in the surface waters of the Irish Sea and its relation to tidal stirring. INTERNATIONAL JOURNAL OF REMOTE SENSING, 19 (14), 2789-2805.

Bowers, D.G., Gaffney, S., White, M., Bowyer, P., 2002. Turbidity in the southern Irish Sea. CONTINENTAL SHELF RESEARCH, 22 (15), 2115-2126.

Bowers, D.G., Ellis, K.M., Jones, S.E., 2005. Isolated turbidity maxima in shelf seas. CONTINENTAL SHELF RESEARCH, 25 (9), 1071-1080.

Brown, J., Carrillo, L., Fernand, L., Horsburgh, K.J., Hill, A.E., Young, E.F., Medler, K.J., 2003. Observations of the physical structure and seasonal jet-like circulation of the Celtic Sea and St. George's Channel of the Irish Sea. CONTINENTAL SHELF RESEARCH, 23 (6), 533-561.

Chen, Z.Q., Hu, C.M., Muller-Karger, F., 2007. Monitoring turbidity in Tampa Bay using MODIS/Aqua 250-m imagery. REMOTE SENSING OF ENVIRONMENT, 109 (2), 207-220.

Doxaran, D., Froidefond, J.M., Castaing, P., 2003. Remote-sensing reflectance of turbid sediment-dominated waters. Reduction of sediment type variations and changing illumination conditions effects by use of reflectance ratios. APPLIED OPTICS, 42 (15), 2623-2634.

Eleveld, M.A., Pasterkamp, R., van der Woerd, H.J., Pietrzak, J.D., 2008. Remotely sensed seasonality in the spatial distribution of sea-surface suspended particulate matter in the southern North Sea. ESTUARINE COASTAL AND SHELF SCIENCE, 80 (1), 103-113.

Gowen, R.J., Stewart, B.M., Mills, D.K., Elliot, P., 1995. Regional differences in stratification and its effect on phytoplankton production and biomass in the northwestern Irish Sea. JOURNAL OF PLANKTON RESEARCH, 17 (4), 753-769.

Kirk, J. T. O., 1994. Light and photosynthesis in aquatic ecosystems. 2nd edition. Cambridge University Press.

Nechad, B., Ruddick, K.G. and Park, Y., 2010. Calibration and validation of a generic multisensor algorithm for mapping of total suspended matter in turbid waters. REMOTE SENSING OF ENVIRONMENT, 114 (4), 854-866.

Ouillon, S., Douillet, P., Petrenko, A., Neveux, J., Dupouy, C., Froidefond, J.M., Andrefouet, S., Munoz-Caravaca, A., 2008. Optical algorithms at satellite wavelengths for Total Suspended Matter in tropical coastal waters. SENSORS, 8 (7), 4165-4185.

Robinson, I., 2008. Marine Board European Science Foundation Position Paper 12. Remote Sensing of Shelf Sea Ecosystem - State of the Art and Perspectives.

Simpson, J.H., Hunter, J.R., 1974. Fronts in the Irish Sea. NATURE 250, 404-406.

Verspecht, F., Rippeth, T.P., Howarth, M.J., Souza, A.J., Simpson, J.H., Burchard, H., 2009. Processes impacting on stratification in a region of freshwater influence: Application to Liverpool Bay. JOURNAL OF GEOPHYSICAL RESEARCH-OCEANS, 114, Art. No. C11022.

Whitehouse, R., Soulsby, R., Roberts, W., Mitchener, H., 2000. Dynamics of estuarine muds. Thomas Telford Publishing, London, 48-49.

Xing, J.X., Davies, A.M., 2001. A three-dimensional baroclinic model of the Irish Sea: Formation of the thermal fronts and associated circulation. JOURNAL OF PHYSICAL OCEANOGRAPHY, 31 (1), 94-114.

Chapter 6

Relationships between hydrological parameters and remote sensing reflectance in tidally stirred shelf seas. Part 1: stratification patterns in low reflectance variance regimes

Summary

This chapter investigates the feasibility of obtaining information on hydrological processes from ocean colour data measured at the locations identified in chapter 5 as having low temporal variance. Using $R_{rs}667$ as an indicator of suspended sediment concentration, variations of reflectance can be attributed to mechanisms driving sediment transport. The existence of a relationship between $R_{rs}667$ and model POLCOMS derived delta sigma, $\Delta\sigma$, was investigated through analysis of remote sensing time series. Initial results suggested a power law relationship connects these two parameters, but the classification of data into three distinct groups using Gaussian mixture modelling demonstrated the limitations of this relationship. It was shown that a time dependent factor was contributing to the breakdown of the simple relationship. This was apparent in time series where the sediment and hydrological dynamics were out of phase. Establishment of time dependent correlations may provide important information for the formulation and validation of hydrodynamic models and also for the choice of locally tuned algorithms for interpreting satellite images.

6.1 Introduction

Accurate representation of a shelf sea ecosystem relies on the knowledge of two co-dependent systems; the quantitative estimate of sea water and its constituent composition and the physical processes in which they are embedded (Robinson, 2008). Individually, each system provides useful information on the state of our oceans (Antoine et al., 1996, O'Reilly et al., 1998, Siegel et al., 2002). However, coincident analysis offers greater understanding of the mechanisms driving the apparent reflectance variability in coastal seas (Mortimer, 1988). Commonly, the

effects of physical forcing agents are considered when investigating phytoplankton bloom dynamics, where growth is controlled by the availability of light and nutrients which in turn depend on various climatic factors (Behrenfeld et al., 2006). As a result, chlorophyll a has been associated with stratification (Sathyendranath et al., 1995), tidal stirring (Cloern, 1991) and winds (Pennington et al., 2006). These physical factors also control sediment dynamics in shelf seas. In this case, concentrations of MSS can be used to identify and map hydrological features such as tidal maxima and river plume transport. In the 2009 paper published by Doxaran et al., satellite reflectance values were used in conjunction with field observations of salinity and turbidity to investigate the dynamics of a marked turbidity maximum (TM) in the Gironde estuary. It was shown that the TM location varied with river flow into the estuary whilst sediment concentrations were predominantly controlled by tidal currents. Although this estuarine environment differs significantly from the Irish Sea (sediment concentrations range from approximately 80 to 2000 gm^{-3}), this study demonstrates the effectiveness of physical-optical analysis. A similar study conducted for the Irish Sea showed that in some parts, patterns of suspended sediment were correlated with tidal stirring (Weeks et al., 1993 and Bowers et al., 1998). However, this did not account for the seasonal variability present in the region. In an attempt to fully understand the interacting processes driving seasonal patterns of sediment, Bowers et al., 2005 and Ellis et al., 2008 considered the size distribution of flocculated particles. It was suggested that the aggregation and break-up of cohesive sediment in response to turbulent shear was responsible for the temporally varying levels of suspended particulate matter at locations containing maximum values of tidal currents. Furthermore this provided a sustainable source of fine sediments at these locations.

In the central East China Sea, the existence and variability of a sediment plume was described by Shi et al. (2010) in terms of changes in the stability of the water column. Strong vertical mixing (identified by minimal temperature gradients measured between 0 and 50 m) and enhanced surface winds coincide with maximum levels of satellite derived diffuse attenuation at 490 m (Kd490). Contrastingly, low values of Kd490 were measured in summer months, where stratification reduced

sediment resuspension by vertical mixing. Physical-optical analysis is also useful for hydrological model tuning, whereby satellite estimates of suspended sediment load are provided as input parameters in numerical routines. Model variables can then be altered to demonstrate sensitivity to particular hydrodynamic parameters such as settling velocities and critical shear stresses for erosion. Data assimilation has proven effective in several studies, including Vos et al. (2000) in the North Sea, and more recently, van der Wal et al. (2010), in the Dutch Westerschelde estuary. In this paper, it was again proposed that patterns of suspended particulate matter, and bottom sediment, were related to tides, winds and freshwater discharge.

These examples highlight the prospect of improving our understanding of the shelf sea ecosystem by considering the driving forces responsible for spatial and temporal sediment variability. However, very few studies attempt to infer physical properties from ocean colour. One example by van der Lee et al. (2009) related the Kolmogorov microscale to satellite derived particle size in the Irish Sea. The relationship between these two parameters was complex, but it serves as a reminder that additional supplementary information can be obtained from the ocean colour signal. This study investigates the existence of a potential link between the optical reflectance signal measured remotely by satellite and the physical dynamics of mixing and stratification deduced from numerical modelling. Using mineral suspended solids (MSS) as a tracer of the hydrodynamics, a simple hypothesis was developed; in mixed regimes, turbulent energy transports sediment to the sea surface where an R_{rs} signal can be measured. In stratified waters, sediment sinks out of the upper layer, eliminating a detectable R_{rs} signal at the surface (Jones et al., 1998). A schematic description of the hypothesis is shown in Figure 6.1. Establishment of a correlation between $R_{rs}667$ and $\Delta\sigma$ may provide important information for the formulation and validation of hydrodynamic models and also for the choice of locally tuned algorithms for interpreting satellite images.

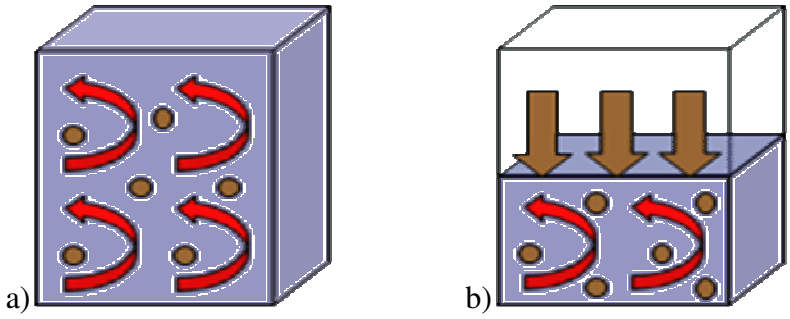

Figure 6.1 Schematic view of sediment dynamics under mixed a) and stratified b) conditions.

6.2 Test site

A possible link between vertical mixing processes and remote sensing reflectance was explored using the Irish Sea as a test site. This area contains various interesting hydrodynamic features, including seasonal thermal stratification fronts and permanent salinity fronts. It is also a region of high tidal energy (Simpson and Hunter, 1974). The Irish Sea offers several advantages as a test site, including the existence of a well-tested numerical model of its hydrodynamics (POLCOMS) (Holt et al., 2005; Brown et al., 2010) and a large database of observations of seawater composition and in-situ optical properties. Regions of low reflectance variance were considered (as classified in chapter 5) as locations potentially influenced by stratification. Their location is illustrated as red pixels in Figure 6.2.

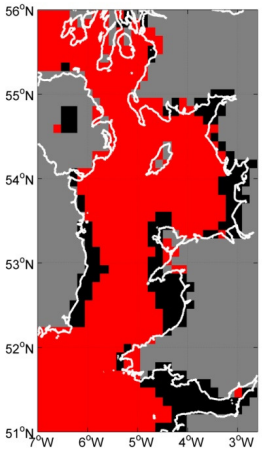

Figure 6.2 Regions of low reflectance variance classified in chapter 4 shown in red.

6.3 Modelled data

The stratification parameter, $\Delta\sigma$, was developed from POLCOMS calculations of daily averaged temperature and salinity, along with a map of Irish Sea bathymetry (chapter 3). These were obtained using climatological model inputs for 2007. Density at the top and bottom of the water column was determined using equations of state (Fofonoff and Millard, 1983). The corresponding difference in density, or $\Delta\sigma$, was used as an indicator of stratification (kg m^{-3}). The difference may be positive or negative depending on the choice of coordinates. Here, $\Delta\sigma$ is negative where the bottom density is subtracted from the top. Large absolute values of $\Delta\sigma$ are indicative of stratification, whilst small differences suggest the water column is homogeneously mixed. $\Delta\sigma$ was calculated for each day containing a cloud free satellite image. Monthly composites of $\Delta\sigma$ were also produced for the 2007 model outputs, and time series were generated by concatenating monthly data at each image pixel.

6.4 Satellite data

MODIS reflectance images of the Irish Sea were obtained from GSFC Ocean Color Web and processed using SeaDAS 6.1 with default atmospheric correction procedures (section 2.1). Using all cloud free images available in 2007 (32 images), monthly composites were generated by averaging pixels containing more than one reflectance value per month. This provided greater coverage of the test site, particularly in winter months where very few cloud free images were available. To compensate for a scarcity of observations during winter months, the January 2007 and December 2007 composites were combined with December 2006 and January 2008 respectively to generate the first and last winter scene. Time series of $R_{rs}667$ were also produced on a pixel by pixel basis.

For succinctness, analysis was performed using $R_{rs}667$, and by implication MSS. Conversion between the two parameters is possible at any stage of the study. Concentrations of the hydrodynamic tracer MSS can be obtained from measurements of $R_{rs}667$ (sr^{-1}) using the equation;

$$MSS_{(u,l)} = C_1(u,l) \times (R_{rs}667)^2 + C_2(u,l) \times (R_{rs}667) + C_3(u,l) \qquad (6.1)$$

with coefficients (C_1, C_2, C_3) for the upper and lower boundaries (u,l) listed in Table 4.3. A full description of the derivation of this formula can be found in chapter 4.

6.5 Seasonal variability of reflectance and Δσ

Marked temporal and spatial variations in reflectance measured at red wavelengths are frequently observed in the Irish Sea. Figure 6.3 contains three daily images of $R_{rs}667$ measured by MODIS Aqua on a) 29 January 2007, b) 02 May 2007, c) 06 August 2005 and the corresponding Δσ values determined for each of these days (d, e, f). Increased insolation during spring and summer promotes stratification of the water column in the Celtic Sea and north-west Irish Sea, allowing sediment to sink out of surface waters. This hydrological event is recognisable in the reflectance patterns of the May and August MODIS images, where reduced R_{rs} signals are found in stratified areas. The January image, which is representative of winter conditions, shows a general increase in the background reflectance signal. A significant reduction in Δσ during this period suggests that transportation of sediment to the surface is permitted due to destratification of the water column.

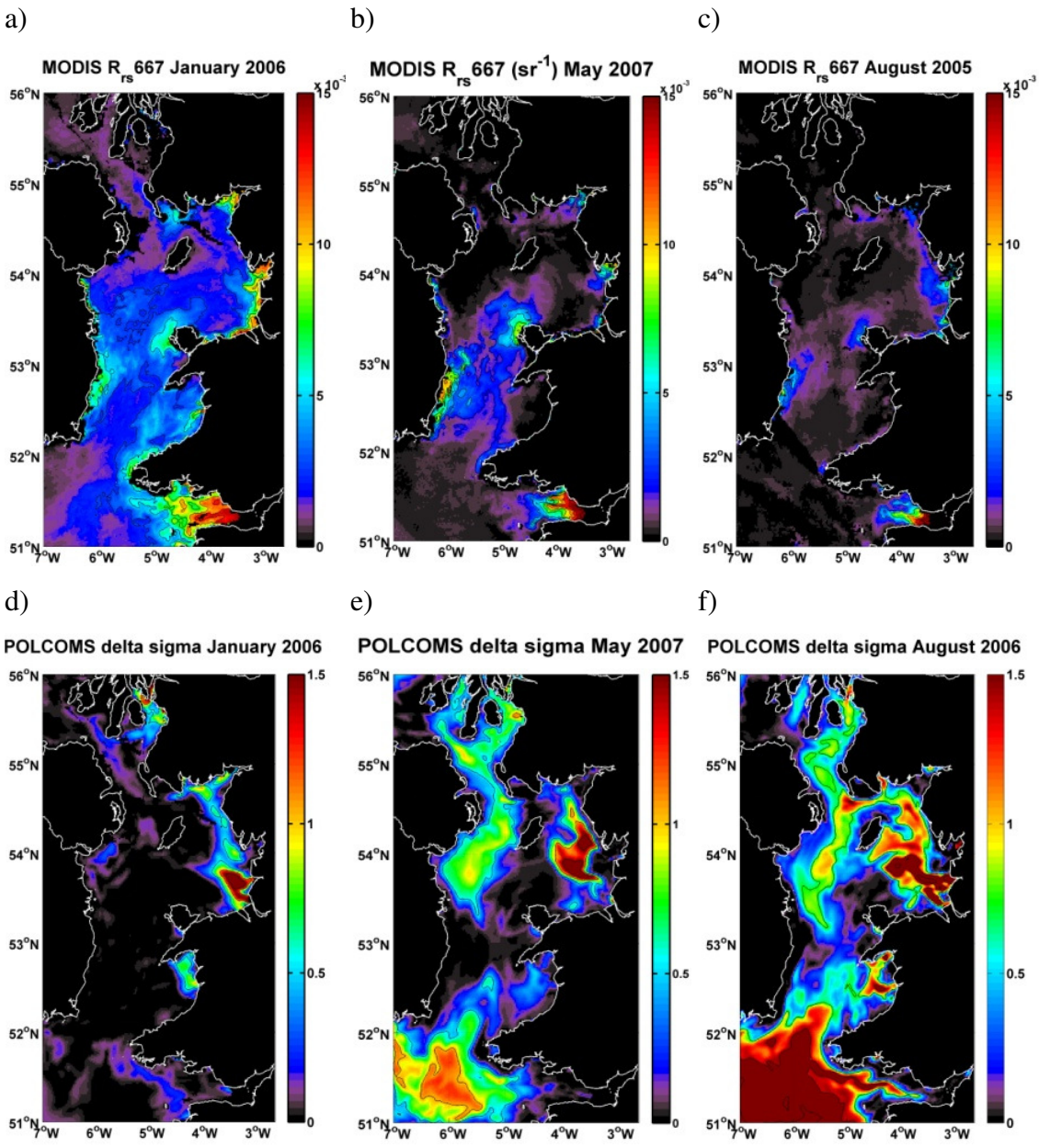

Figure 6.3 MODIS images of $R_{rs}667$ (sr^{-1}) measured a) 29 January 2007, b) 02 May 2007 and c) 06 August 2005. Significant spatial and temporal variations in $R_{rs}667$ can be seen in the Irish Sea throughout the year. These variations may be explained by changes in $\Delta\sigma$ ($kg\ m^{-3}$), as shown in (d, e, f).

6.6 Relationship between $R_{rs}667$ and $\Delta\sigma$

Visual comparison of $R_{rs}667$ and $\Delta\sigma$ suggests a potential inverse correlation between these parameters exists. However, a bivariate plot of May data, shown in Figure 6.4, reveals the complexity of this relationship. No simple formula relates these two parameters. Further investigation was conducted using the 2007 time series data. The duration spent below the annual spatial minima (see chapter 5 for description) was calculated for $R_{rs}667$, along with the temporally averaged $\Delta\sigma$ value for each individual pixel. An approximately trimodal frequency distribution is evident in histograms of these averaged parameters (Figure 6.5). Two break points were applied to determine three subgroups present in both data sets. The location of break points was chosen specifically to separate the apparent natural trimodal distribution of the data. Application of a Gaussian mixture model also identified three subgroups of data which were consistent with those determined from break points. The model fits and break points are also displayed in Figure 5.5.

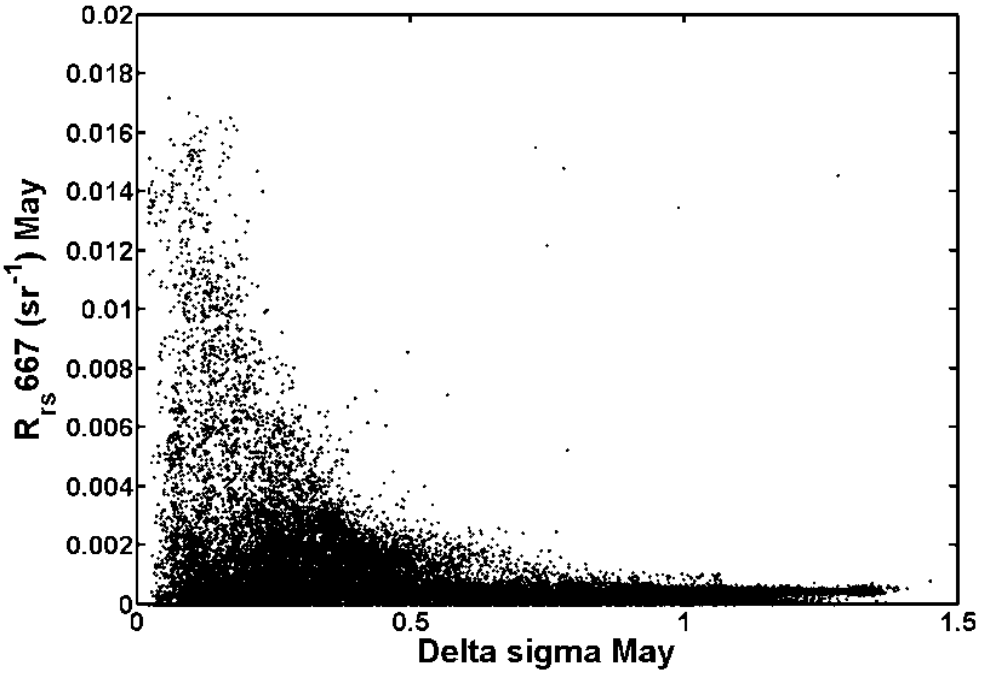

Figure 6.4 Bivariate plot of $\Delta\sigma$ and $R_{rs}667$ measured in May 2007. No simple relationship exists between these parameters.

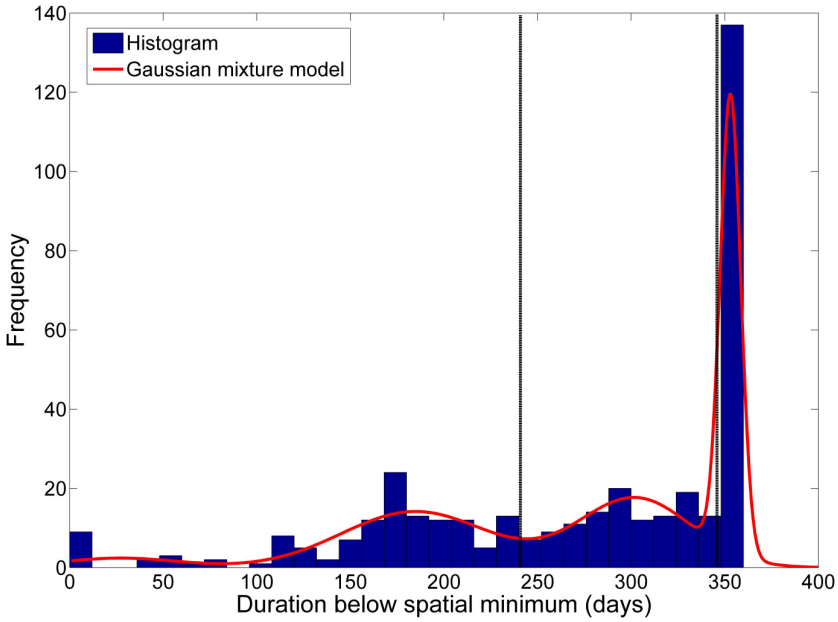

a)

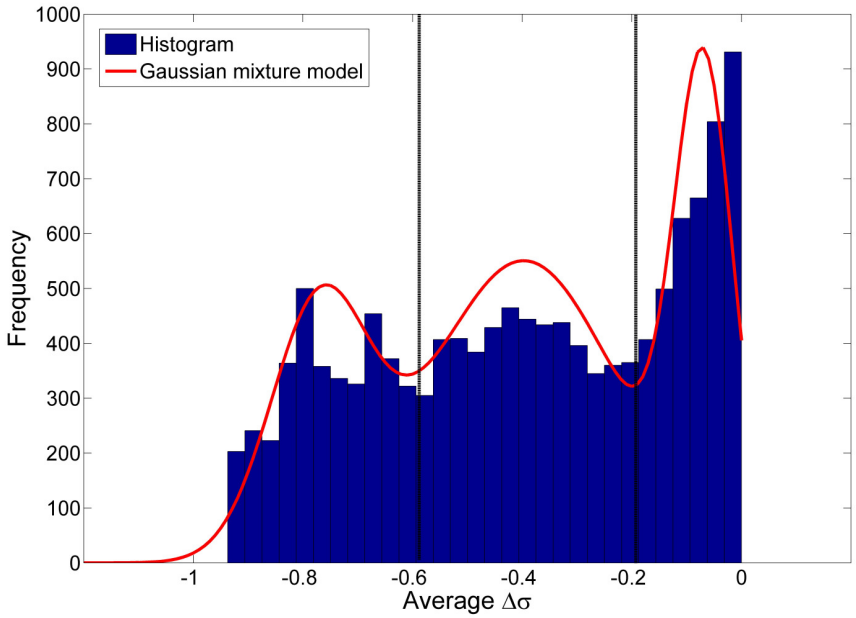

b)

Figure 6.5 Histograms of duration below average annual minima a) and annual mean Δσ b). Red lines depict model fits from a Gaussian mixture distribution routine. Data were separated into 3 subgroups, defined by the mixture model.

It is significant that points contained within each of the $R_{rs}667$ and $\Delta\sigma$ subgroups correspond to geographical regions of the Irish Sea with locations illustrated in Figure 6.6 a) and b). High variance regimes marked in red are excluded from this analysis and will be discussed in the following chapter. Yellow pixels occur in regions where $R_{rs}667$ spends the longest period below the average annual minima. These pixels also occur in areas exhibiting the largest stratification. Blue pixels appear to be an intermediate level for both $R_{rs}667$ and $\Delta\sigma$ parameters. Finally, black pixels, which are defined as mixed in the $\Delta\sigma$ classification, are present where $R_{rs}667$ spends a short period below the 2007 scene minima. The classification scheme appears to be consistent with the original hypothesis that mixed waters promote $R_{rs}667$ signals detectable at the surface whilst stratification inhibits surface reflectance.

As a next step, the spatial correlation or agreement between $R_{rs}667$ and $\Delta\sigma$ was investigated by comparing the classified groups of the two parameters. A simple subtraction of classified groups assigned numbers 1,2, or 3 highlights regions which contain data points consistent with the hypothesis. Moreover, deviations from the hypothesis, whereby classified groups do not occur in the same location, can also be determined. This result is shown in Figure 6.7. The map is colour coordinated depending on the level of agreement. Green pixels exhibit total agreement between the two classification schemes. These locations cover 66 percent of the test site. Values falling within an orange or red region are positioned in inconsistent groups, orange differing by one group and red by two. These are the spatial locations where the relationship between $R_{rs}667$ and $\Delta\sigma$ breaks down.

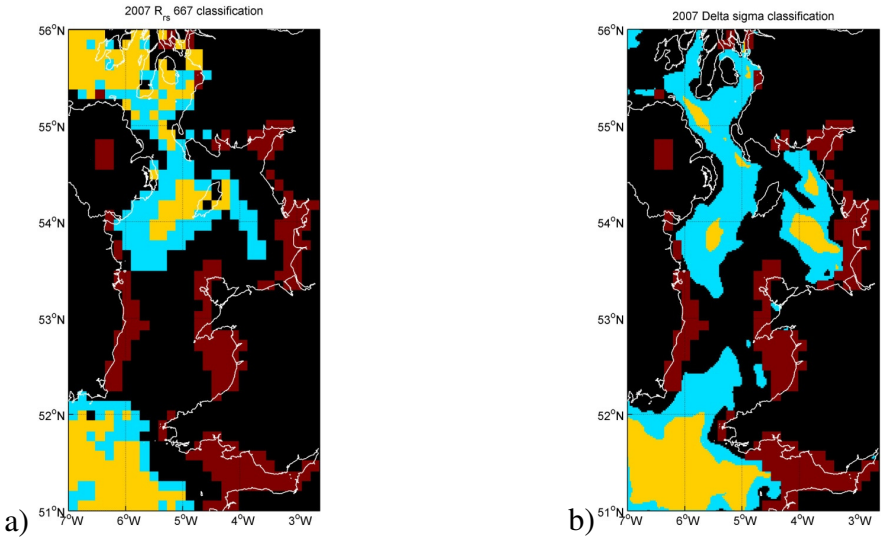

Figure 6.6 Classification of $R_{rs}667$ a) and $\Delta\sigma$ b) using subgroups presented in trimodal histogram distributions. Red areas are regions of high variance and are not included in this analysis.

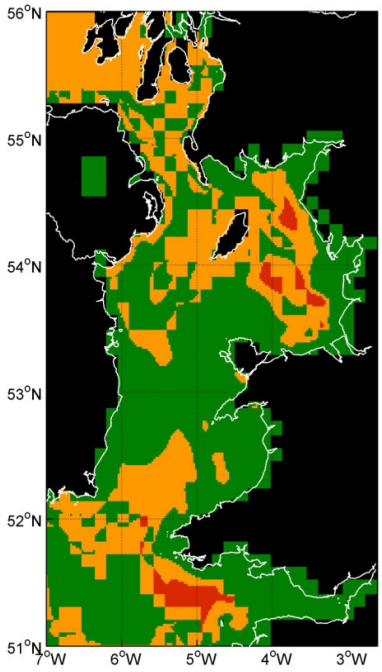

Figure 6.7 Map showing spatial correlation between the reflectance and $\Delta\sigma$ groups. Green pixels contain data points which appear in the same classified groups (Figure 6.5), whilst red and orange areas are inconsistent with the hypothesis.

6.7 Possible mechanisms generating complexity in the relationship between $R_{rs}667$ and $\Delta\sigma$

The deviation from a simple relationship was investigated using time series of monthly composites. Two example time series are shown in Figure 6.8 a) and b) taken from the Celtic Sea and eastern Irish Sea respectively, where $\Delta\sigma$ is depicted by blue curves and $R_{rs}667$ is shown in red. The variability of both parameters is illustrated effectively by this example. In the Celtic Sea, reflectance and stratification appear to be in phase. When stratification occurs, $R_{rs}667$ values decrease and destratification coincides with the recovery of sediment. However, the second (Irish Sea) example exhibits a more complex pattern, where the sediment dynamics do not necessarily follow stratification. In particular, there appears to be a time lag in the resuspension of sediment in the second half of the year. From this, we can deduce that a time dependent factor is contributing to the breakdown of the relationship between $R_{rs}667$ and $\Delta\sigma$.

Further investigation of the relationship was conducted using the following procedures: 1) Each time series was split into two parts, the first and second half of the year centred on 01 July. 2) The data were normalised by the maximum value to account for yearly variability in the available levels of sediment. 3) On a pixel by pixel basis the area under the curve was calculated for the two sections of the year, producing four output images (two for $\Delta\sigma$ and two for $R_{rs}667$). For $\Delta\sigma$, a large area calculated in the first half of the year suggests stratification occurs late, whilst an increase in the second part indicates early destratification. The same is also true for $R_{rs}667$ in terms of settling and resuspension rates. 4) The area under the curve calculated for the second half of the year was subtracted from the area of the first. Differences in the dynamics can be reviewed by this subtraction (Figure 6.9 a) and b)). Analysis of these results relies heavily on the interpretation of the images. However, prior knowledge of Irish Sea hydrodynamics allows a sensible explanation to be developed describing the breakdown of the relationship in various geographical regions.

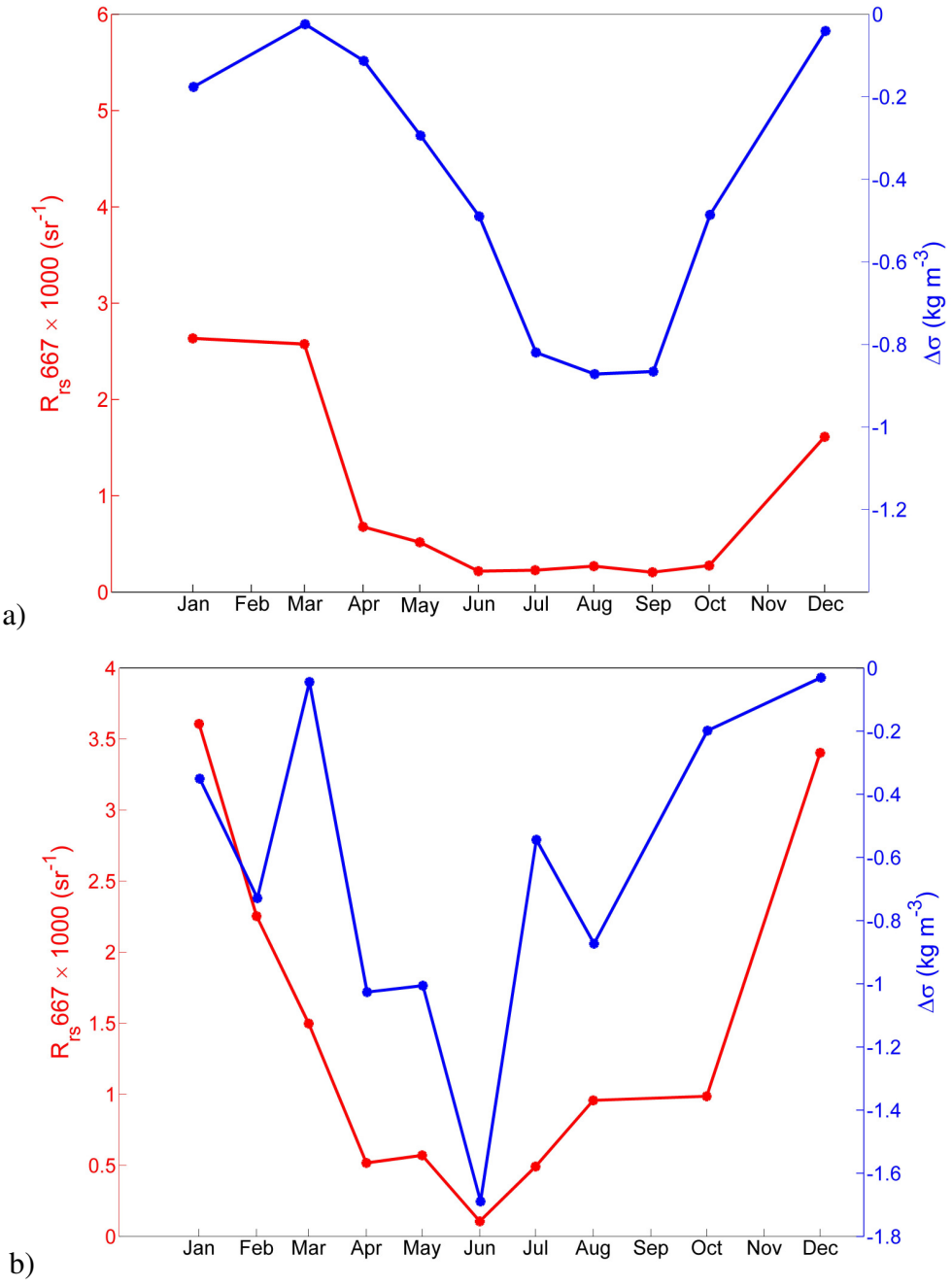

Figure 6.8 Time series of $R_{rs}667$ (red) and $\Delta\sigma$ (blue) taken from the 2007 archived data set measured at two locations in the test site. The sediment dynamics of the Celtic Sea, a), appear to be in phase with the hydrology of the water column. In the Eastern Irish Sea however, b) a more complex pattern of mixing exists which is not recognisable in the $R_{rs}667$ signal.

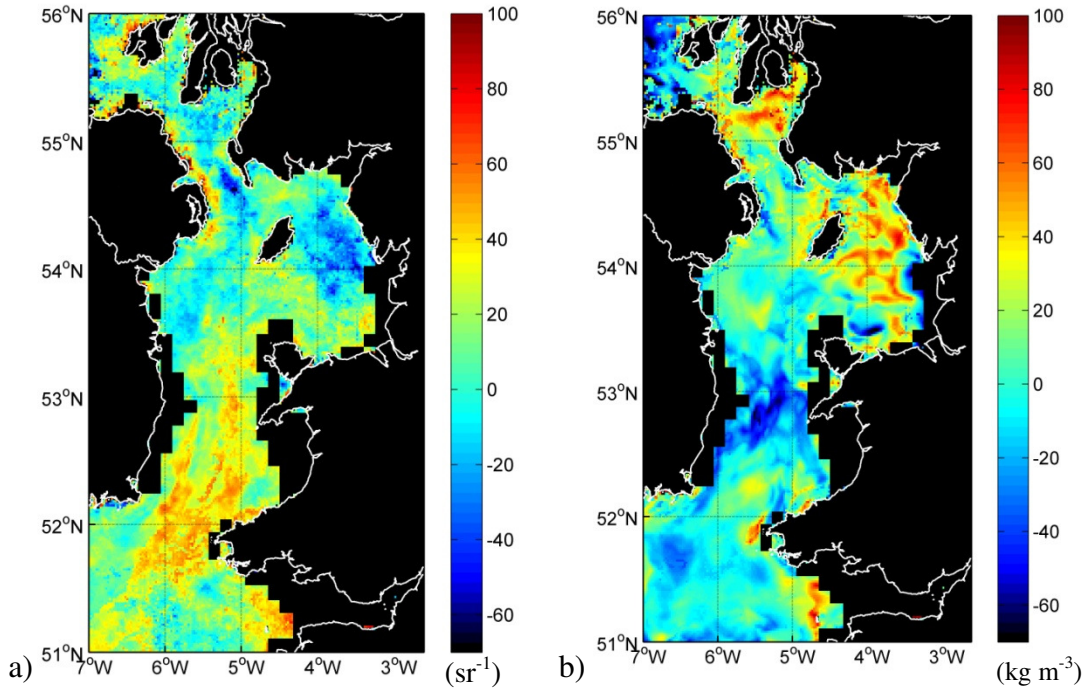

Figure 6.9 Differences in the area under the time series curve calculated for two parts of the year for a) $R_{rs}667$ and b) $\Delta\sigma$.

6.8 Discrepancies in the relationship described in terms of inconsistent dynamics

Figure 6.9 a) shows the difference by subtraction of the area describing the settling (first half of the year) and the resuspension of sediment (second half of the year). No difference in integrated area would be expected if a strong correlation existed between $R_{rs}667$ and $\Delta\sigma$ as the seasonal dynamics would be consistent in this case. A positive difference indicates the first half of the year contains the greatest area under the curve. This exists if the sediment settles at a later date or recovers slower. North of the Celtic Sea front, a delayed response of sediment settling is a reasonable explanation for the discrepancy. Evidence is provided in Figure 5.13 which shows the duration spent below the spatial minima is small for regions with positive differences. However, south of the front, slow recovery of sediment is more probable, particularly in deeper regions of the Celtic Sea.

In the case of $\Delta\sigma$, shown in Figure 6.9 b), a similar analysis offers interesting insight into the hydrodynamics of the region. The subtraction of the area 2 (second half of

the year) from area 1 (first half of the year) would generate positive values if the water column stratifies later or destratifies slower. From prior knowledge of the west Irish Sea, one would suggest slow breakup of the stratified regime is a sensible explanation for the failure of a simple relationship between $R_{rs}667$ and $\Delta\sigma$ in this location.

6.9 Production of hydrodynamical information from $R_{rs}667$

These examples serve as a reminder of the complexity of the physical dynamics in the Irish Sea and provide a potential explanation for the absence of a simple correlation between $R_{rs}667$ and $\Delta\sigma$. However for the majority of the test site a power law relationship can be indentified. Figure 6.10 gives an example of power model fits for three locations. The coefficients of the power function vary spatially across the Irish Sea. For regions with agreement between Gaussian mixture model classified groups, shown as green pixels in Figure 6.7, $R_{rs}667$ can be expressed in terms of $\Delta\sigma$ as follows;

$$R_{rs}667 = a_0 \Delta\sigma^{a1} \qquad (6.2)$$

Coefficients a_0 and a_1 are approximately equal to 0.3 and -0.5 respectively. Although limited to the boundaries defined by Figure 6.7, use of this formula can provide information on the hydrodynamics of the region by exploitation of satellite radiometric measurements of $R_{rs}667$. The R^2 value describing the goodness of the power law model fit varies across the region of interest. For the data contained within Figure 6.10, residual analysis determines an R^2 value of 0.51. Investigation of the sum of squares of the residuals suggests the model fails at low values of $\Delta\sigma$, shown in Figure 6.11. The results are normalized to the sum of the square of the distances of points from the mean of all satellite reflectance values. This implies the absolute magnitude of mixing cannot generate quantitative estimates of $R_{rs}667$. The presence of a surface reflectance signal can however provide qualitative information on the mixing dynamics. Furthermore, by ignoring the residuals calculated in the fully mixed regime and considering only data obtained in the hydrodynamic transition period the R^2 value is improved to 0.77.

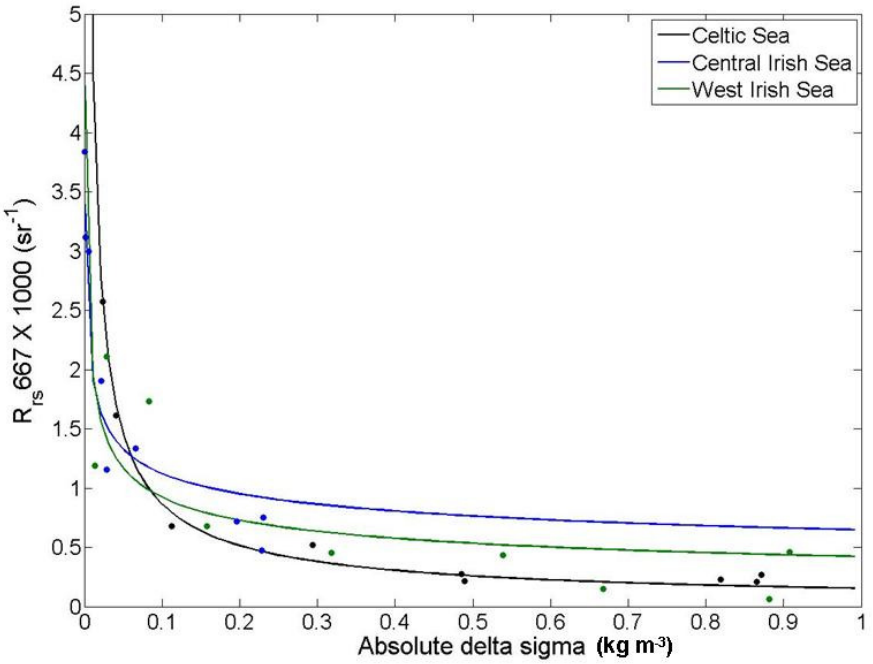

Figure 6.10 Power law fits for three locations in the Irish Sea.

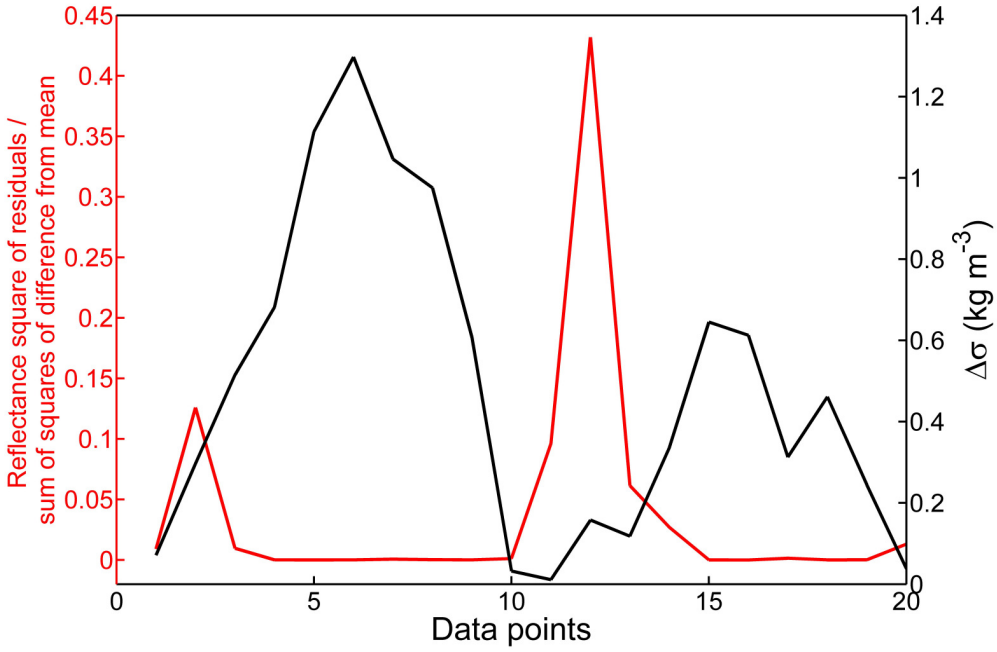

Figure 6.11 Plot of square of residuals with corresponding Δσ indicates the power law function fails to replicate $R_{rs}667$ at low values of Δσ.

6.10 Potential applications

The previous clarification of relationships between $R_{rs}667$ and $\Delta\sigma$ allows the development of practical applications, such as front detection from ocean colour images. Figure 6.12 shows transects taken from 2 locations in the Irish Sea, transect one from A to B and transect 2 from C to B. Annotated lines highlight the locations where sediment begins to drop from the upper layer of the water column. In both examples it can be seen that a corresponding gradient in $\Delta\sigma$ occurs at these locations. The initial point of $R_{rs}667$ reduction marks the location of the front. Changes in $R_{rs}667$ can therefore be used to determine the position of temporal onset of stratification fronts in the region.

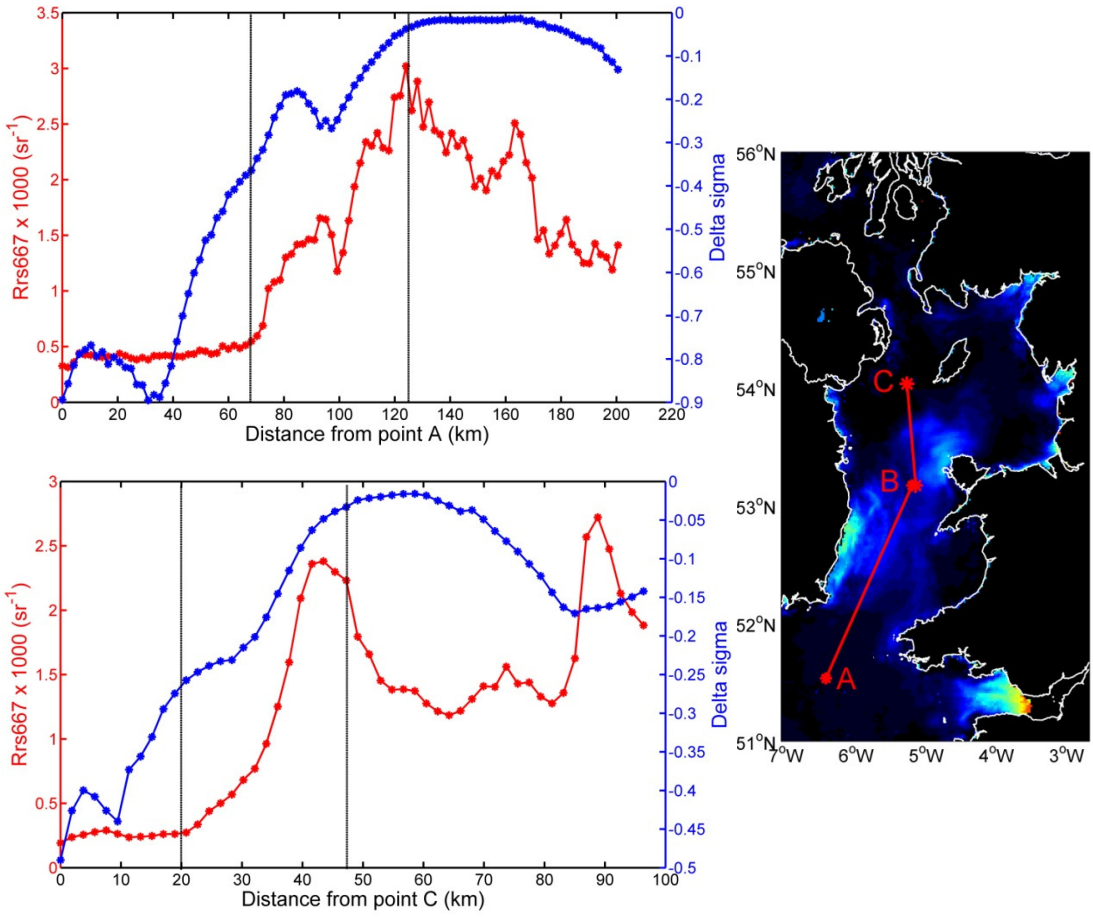

Figure 6.12 Transects taken from 2 locations in the Irish Sea demonstrate the potential of using gradients in ocean colour images to determine the location of fronts between stratified and mixed waters.

6.11 Discussion

Coastal shelf seas are subject to various physical and hydrodynamic processes that promote bed erosion and transport of sediment to the sea surface. Use of $R_{rs}667$ as an indicator of MSS concentrations allows spatial patterns and temporal variability of suspended sediment concentrations to be monitored using remotely sensed ocean colour data. By understanding the mechanisms driving the variability it is possible to link remote sensing reflectance to the hydrodynamics of the water column. Irish Sea time series were used to explore a potential correlation between $R_{rs}667$ and stratification parameter $\Delta\sigma$. On first inspection, a binary relationship appears to connect these two parameters, whereby the water column is either stratified with no reflectance signal or mixed with a signal. High surface reflectance is observed in regions of hydrodynamic mixing, whilst the absence of sediment in the upper layer of stratified waters prevents a detectable signal at the surface. However, further investigation suggests a more complex link exists. To fully understand the limitations of the simple binary relationship, data were categorised into three groups determined by Gaussian mixture modelling. This demonstrated regions of the test site in which consistent correlation existed between the two parameters. Moreover, this technique provided spatial classification of those geographical areas which showed $\Delta\sigma$ vs. $R_{rs}667$ relationships inconsistent with the original hypothesis. Time series measured at these locations showed sediment and hydrological dynamics were out of phase, suggesting a time dependent factor is contributing to the complexity of the relationship. Resistance to destratification in the eastern Irish Sea due to varying levels of freshwater input is one possible explanation for this discrepancy. However, further investigation is required to validate this hypothesis. Nonetheless, for the majority of the test site, the relationship between $R_{rs}667$ and $\Delta\sigma$ exists as power law. Transects taken from 2 locations in the Irish Sea demonstrate the potential of using gradients in ocean colour images to predict stratification fronts in coastal seas. This highlights the potential of exploiting satellite remote sensing to provide information on shelf sea dynamics.

Key points from chapter 6

1. A stratification parameter $\Delta\sigma$ was calculated for pixels located within the low variance regime. Data extracted for the 2007 model run were combined to generate time series of $\Delta\sigma$ for the Irish Sea.

2. Monthly composites of $R_{rs}667$ were generated and combined to create Irish Sea reflectance time series.

3. Images of $\Delta\sigma$ and $R_{rs}667$ were generated using Matlab image processing software and used to illustrate spatial and seasonal changes in both parameters. Visual comparison indicates an inverse relationship exists.

4. Application of a Gaussian mixture model to histograms of the annual average $\Delta\sigma$ and the duration spent below the spatial minimum reflectance subdivided the low variance regime into three groups, exhibiting contrasting optical and physical dynamics. These groups correspond to geographical locations in the Irish Sea, one which remains strongly stratified for the majority of the year, an intermediate group which stratifies relatively later and a final section which remains proportionately mixed all year round. Comparison of the optical and physical classified groups determined the level of conformity between parameters allowing geographical regions to be assigned by their level of correspondence.

5. Time series were used to highlight limitations of a simple power law relationship between $\Delta\sigma$ and $R_{rs}667$. Discrepancies in the relation were found at locations where time series displayed inconsistent dynamics i.e. were out of phase.

6. For the majority of the test site, surface reflectance values can be used as a predictive indicator of stratification. However, at locations containing dynamical discrepancies, such as slow recovery of reflectance or delayed destratification (red pixels in Figure 6.7) Rrs667 cannot be used to identify

fronts between stratified and mixed waters. Furthermore, the brightness of $R_{rs}667$ cannot determine the extent of stratification. The inverse argument for mixing is also true. Mixing of the water column may result in increased reflectance but the magnitude of mixing does not determine how much reflectance, and by implication MSS, will be measured at the surface.

References

Antoine, D., Andre, J.M., Morel, A., 1996. Oceanic primary production .2. Estimation at global scale from satellite (coastal zone color scanner) chlorophyll. GLOBAL BIOGEOCHEMICAL CYCLES, 10 (1), 57-69.

Behrenfeld, M.J., O'Malley, R.T., Siegel, D.A., McClain, C.R., Sarmiento, J.L., Feldman, G.C., Milligan, A.J., Falkowski, P.G., Letelier, R.M., Boss, E.S., 2006. Climate-driven trends in contemporary ocean productivity. NATURE, 444 (7120), 752-755.

Bowers, D.G., Boudjelas, S., Marker, G.E.L., 1998. The distribution of fine suspended sediments in the surface waters of the Irish Sea and its relation to tidal stirring. INTERNATIONAL JOURNAL OF REMOTE SENSING, 19 (14), 2789-2805.

Bowers, D.G., Ellis, K.M., Jones, S.E., 2005. Isolated turbidity maxima in shelf seas. CONTINENTAL SHELF RESEARCH, 25 (9), 1071-1080.

Brown, J.M., Souza, A.J., Wolf, J., 2010. An 11-year validation of wave-surge modelling in the Irish Sea, using a nested POLCOMS-WAM modelling system. OCEAN MODELLING, 33 (1-2), 118-128.

Cloern, J.E., 1991. Tidal stirring and phytoplankton bloom dynamics in an estuary. JOURNAL OF MARINE RESEARCH, 49 (1), 203-221.

Doxaran, D., Froidefond, J.M., Castaing, P., Babin, M., 2009. Dynamics of the turbidity maximum zone in a macrotidal estuary (the Gironde, France): Observations from field and MODIS satellite data. ESTUARINE COASTAL AND SHELF SCIENCE, 81 (3), 321-332.

Ellis, K.M., Binding, C.E., Bowers, D.G., Jones, S.E., Simpson, J.H., 2008. A model of turbidity maximum maintenance in the Irish Sea. ESTUARINE COASTAL AND SHELF SCIENCE, 76 (4), 765-774.

Fofonoff, N.P., Millard Jr, R.C., 1983. Algorithms for computation of fundamental properties of seawater. UNESCO TECHNICAL PAPERS IN MARINE SCIENCE, 44.

Holt, J.T., Allen, J.I., Proctor, R., Gilbert, F., 2005. Error quantification of a high resolution coupled hydrodynamic-ecosystem coastal-ocean model: Part 1 model

overview and assessment of the hydrodynamics. JOURNAL OF MARINE SYSTEMS, 57 (1-2),167-188.

Jones, S.E., Jago, C.F., Bale, A.J., Chapman, D., Howland, R.J.M., Jackson, J., 1998. Aggregation and resuspension of suspended particulate matter at a seasonally stratified site in the southern North Sea: physical and biological controls. CONTINENTAL SHELF RESEARCH, 18 (11), 1283-1309

Mortimer, C.H., 1988. Discoveries and testable hypotheses arising from Coastal Zone Color Scanner imagery of southern Lake Michigan. LIMNOLOGY AND OCEANOGRAPHY, 33 (2), 203-226.

O'Reilly, J.E., Maritorena, S., Mitchell, B.G., Siegel, D.A., Carder, K.L., Garver, S.A., Kahru, M., McClain, C., 1998. Ocean color chlorophyll algorithms for SeaWiFS. JOURNAL OF GEOPHYSICAL RESEARCH-OCEANS, 103 (C11), 24937-24953.

Pennington, J.T., Mahoney, K.L., Kuwahara, V.S., Kolber, D.D., Calienes, R., Chavez, F.P., 2006. Primary production in the eastern tropical Pacific: A review. PROGRESS IN OCEANOGRAPHY, 69 (2-4), 285-317.

Robinson, I., 2008. Marine Board European Science Foundation Position Paper 12. Remote Sensing of Shelf Sea Ecosystem - State of the Art and Perspectives.

Sathyendranath, S., Longhurst, A., Caverhill, C.M., Platt, T., 1995. Regionally and seasonally differentiated primary production in the North Atlantic. DEEP-SEA RESEARCH PART I-OCEANOGRAPHIC RESEARCH PAPERS, 42 (10), 1773-1802.

Shi, W.S., Wang, M.H., 2010. Satellite observations of the seasonal sediment plume in central East China Sea. JOURNAL OF MARINE SYSTEMS, 82 (4), 280-285.

Siegel, D.A., Maritorena, S., Nelson, N.B., Hansell, D.A., Lorenzi-Kayser, M., 2002. Global distribution and dynamics of colored dissolved and detrital organic materials. JOURNAL OF GEOPHYSICAL RESEARCH-OCEANS, 107 (C12), Art. No. 3228.

Simpson, J.H., Hunter, J.R., 1974. Fronts in the Irish Sea. NATURE, 250, 404 – 406.

van der Lee, E.M., Bowers, D.G., Kyte, E., 2009. Remote sensing of temporal and spatial patterns of suspended particle size in the Irish Sea in relation to the

Kolmogorov microscale. CONTINENTAL SHELF RESEARCH, 29 (9), 1213-1225.

van der Wal, D., van Kessel, T., Eleveld, M.A., Vanlede, J., 2010. Spatial heterogeneity in estuarine mud dynamics. OCEAN DYNAMICS, 60 (3), 519-533 Sp. Iss. SI.

Vos, R.J., ten Brummelhuis, P.G.J., Gerritsen, H., 2000. Integrated data-modelling approach for suspended sediment transport on a regional scale. COASTAL ENGINEERING, 41 (1-3), 177-200.

Weeks, A.R., Simpson, J.H., BOWERS, D., 1993. The relationship between concentrations of suspended particulate material and tidal processes in the Irish Sea. CONTINENTAL SHELF RESEARCH, 13 (12), 1325-1334.

Chapter 7

Relationships between hydrological parameters and remote sensing reflectance in tidally stirred shelf seas. Part 2: Bed shear stress in high reflectance variance regimes

Summary

This chapter investigates variability in remote sensing reflectance, and by implication in suspended sediment concentrations, in high reflectance variance regimes in terms of maximum bed shear stress, τ_{max}. The inclusion of a wave component in the total τ_{max} introduces a seasonal factor, where increased wind-induced waves in winter raise levels of τ_{max} in shallow waters. The statistical dependence of $R_{rs}667$ on τ_{max} was determined by calculating time series correlation coefficients. This demonstrated geographical locations where reflectance variability was attributed to variations in τ_{max}. For pixels where τ_{max} and $R_{rs}667$ were correlated, the relationship existed as an approximately logistic function. This was used to estimate a threshold value for bed erosion in shallow coastal areas of the Irish Sea.

7.1 Introduction

Marked spatial and temporal patterns of red reflectance are apparent in satellite images of the Irish Sea. Here, sediments are controlled by various physical forcing agents, such as tidal stirring, mixed layer processes and external climatic factors. Previous attempts to quantify sediment dynamics in this region have focussed on changes in particle size as the predominant physical driver (Bowers et al., 2005, Ellis et al., 2008, van der Lee et al., 2009) but several questions remain unanswered regarding the general variability across the entire area. This study looks at bed shear stress (BSS, N m^{-2}) as the physical mechanism controlling sediment and $R_{rs}667$ variability in coastal regions of the Irish Sea. A number of papers present BSS as the primary driver of sediment dynamics at similar sites. In the North Sea, Jones et al. (1998) illustrated through in-situ observations of currents and winds that tidal stirring alone was not sufficient to erode bottom sediments in summer, whilst a contribution

to BSS from wind/wave processes enhanced resuspension in winter or during storm events. A similar result was demonstrated in the Wadden Sea (Stanev et al., 2006) with the aid of a simple energy based model, where sediment concentrations increased in accordance with intensified wave-induced bottom shear stress. More recently, Stanev et al. (2009) tested their model result in the North Sea. Here, stresses due to waves and currents were compared with satellite derived surface suspended particulate matter (SPM) concentrations. It was shown for a large part of the test area, that surface sediment concentrations were a consequence of localised BSS. As a next step, model derived BSS was supplied as an input driver to simulate sediment variability in the North Sea (Dobrynin et al., 2010). Once again, SPM concentrations recovered from satellite measurements of reflectance were utilised for efficient validation of the model (Vos et al., 2000).

Knowledge of sediment dynamics is crucial for the improved understanding of pollutant transport and distribution in coastal seas. This was the primary focus of a study conducted by Aldridge et al. (2003) who used a coupled hydrodynamic-sediment transport model to map radionuclide transport across the Irish Sea. Although calculated sediment concentrations were in reasonable agreement with field and satellite data, the model was unable to reproduce seasonal variability. As noted, this may be a consequence of unaccounted wave erosion in winter. Also in the Irish Sea, an SPM model of sediment characteristics in Liverpool Bay showed a considerable percentage of sediment variance was explained by winds, waves and tidal currents (Krivtsov et al., 2008). More specifically, SPM variables were particularly influenced by winds and waves, whilst the relationship with tidal stirring remained generally weaker. These examples highlight the importance of wave-induced BSS in the Irish Sea. However, direct measurements of the parameter are difficult to measure in-situ and therefore emphasis is placed on modelling procedures.

This work investigates the potential of exploiting satellite observations of ocean colour to provide useful information on BSS in coastal regions of the Irish Sea for the formulation and calibration of sediment models. For the purpose of this study, the coastal region is defined as the high reflectance variance regime determined by objective classification in chapter 4. This area was identified as exhibiting high variability in the satellite measured range of reflectance. The relevant geographical region is shown in Figure 7.1.

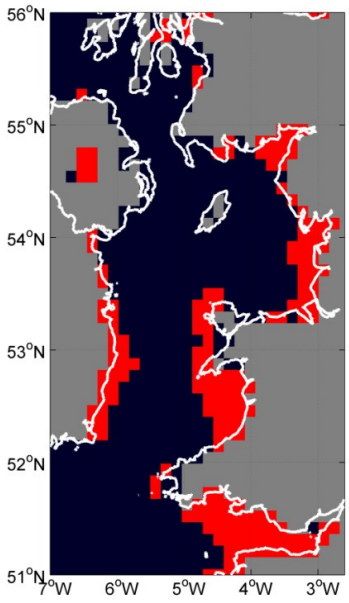

Figure 7.1 Regions with high reflectance variance, as classified in chapter 5, are shown in red.

7.2 Bed shear stress in the Irish Sea

High variance pixels are predominantly located in shallow waters (< 30 m) immediately adjacent to the coast, where the water regime remains mixed all year round. The group classified as high variance contains 3 regions of high tidal velocity, the Bristol Channel, Wicklow Head and North Anglesey, which appear to be correlated with the occurrence of high sediment concentrations. At all locations except the Bristol Channel, surface sediment patterns were found to be annually periodic, suggesting a seasonal process is contributing to suspended sediment variability. In sufficiently shallow water, an additional current velocity at the seafloor

is generated by wind-induced waves (Whitehouse et al., 2000). The wave orbital velocity, *Uw*, is effective to depths, *h*, determined by the wave height, *H*;

$$h < 10 \times H \tag{7.1}$$

Consequently, at high variance locations bed shear stress is a product of tidal and wind-induced wave inputs. An increase in wave height and period during winter months in the Irish Sea cause levels of BSS to rise. Depending on the inherent conditions, the magnitude of BSS may be sufficient to erode and resuspend sediment into the water column, with the level of suspension proportional to flow velocity and roughness of the seabed (Soulsby & Clarke, 2005). This may account for the marked seasonal variability apparent in satellite imagery. A simple hypothesis was therefore developed: increasing BSS as a consequence of enhanced waves results in raised levels of surface sediment, promoting a brightening of the reflectance signature. The validity of this hypothesis was explored using the Irish Sea as a test site.

For the year 2005, modelled wave and current values were extracted from the POLCOMS-WAM model (chapter 3). Calculations of maximum BSS, τ_{max}, were performed on daily maximum values of wave period, significant wave height and depth-averaged current velocity using equations (3.11) to (3.24). Monthly composites were then created by averaging daily values. Figure 7.2 a), b), c) and d) displays τ_{max} for months representing four seasons in 2005, January, May, August and October respectively. Marked spatial variability can be seen in Irish Sea BSS. Four locations, the inner Bristol Channel, Wicklow Head, Anglesey and Solway Firth, contain consistently high values of shear as a result of large tidal velocities. Geographically, these regions correspond to areas of maximum brightness in $R_{rs}667$ images (Figure 5.2). Significant temporal differences can be seen in BSS patterns recovered in Cardigan Bay, where large values are found in winter months, and a reduction is shown in summer. Similarly, this pattern is evident in the outer Bristol Channel and Liverpool Bay. These changes are a consequence of additional bed shear stress produced by waves.

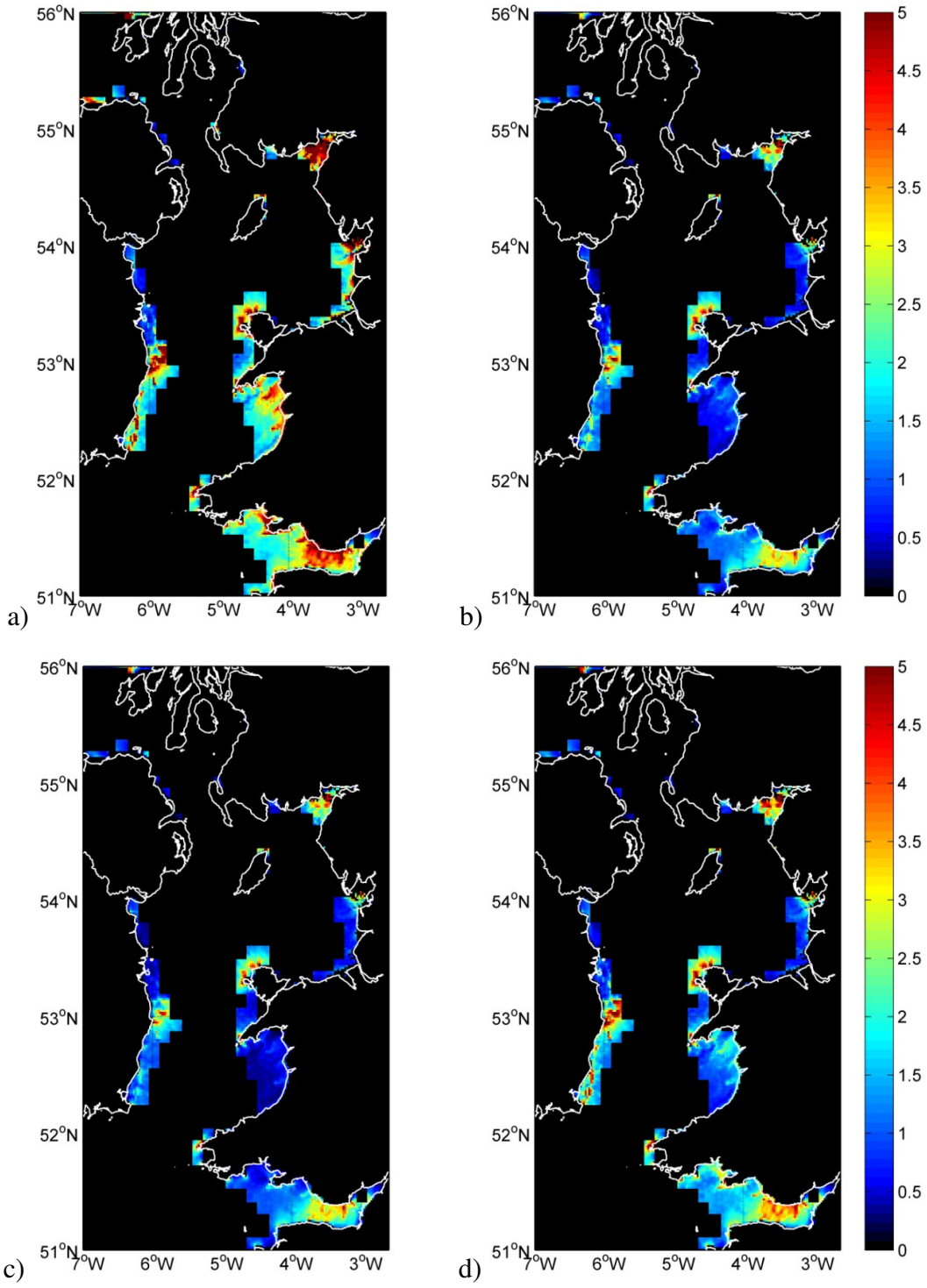

Figure 7.2 τ_{max} (N m^{-2}) calculated for a) January, b) May, c) August and d) October 2005. Marked spatial variability is demonstrated in these images. Consistently high values of BSS are found in the Bristol Channel, Wicklow Head and Anglesey.

7.3 $R_{rs}667$ as an indicator of suspended sediment concentrations

Optical measurements of ocean colour were obtained from the MODIS Aqua satellite (section 2.1). In 2005, 29 cloud free satellite images appeared over the Irish Sea. The data were subsequently processed using SeaDAS software and combined to generate monthly composite of $R_{rs}667$. This reflectance parameter can be used as a proxy of surface sediment concentrations in these waters (chapter 4). Conversion between $R_{rs}667$ and MSS is possible only within the limits given by the upper and lower bounds of the relationship described in chapter 4. However for succinctness, $R_{rs}667$ was used in analyses.

7.4 Time series analysis

Time series of τ_{max} and R_rs667 were created for pixels located within the high variance classification area, where each time series point was represented by monthly composite values. Examples of time series extracted from several marked locations in the Irish Sea are shown in Figure 7.3 a) to g). In these examples, the time frame is expressed in terms of serial date number, which increments 1 number per day.

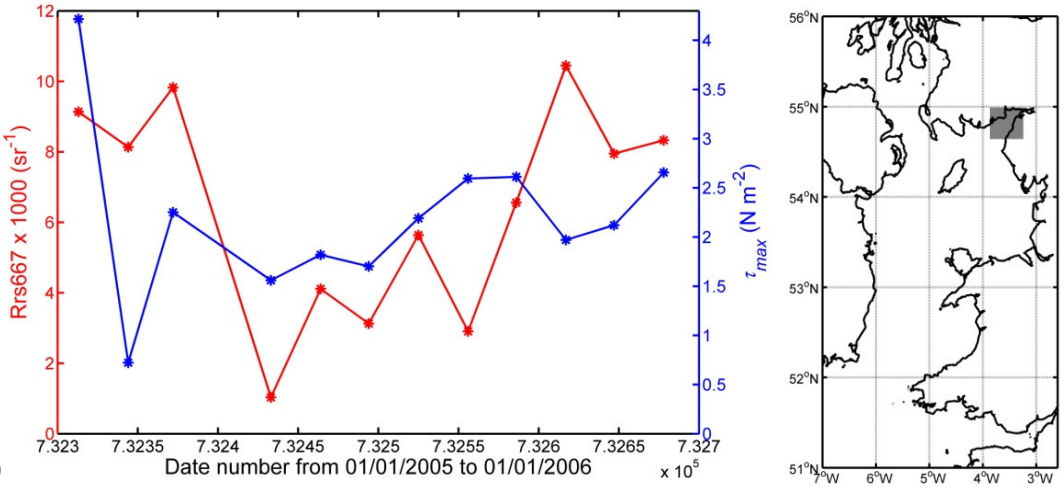

a)

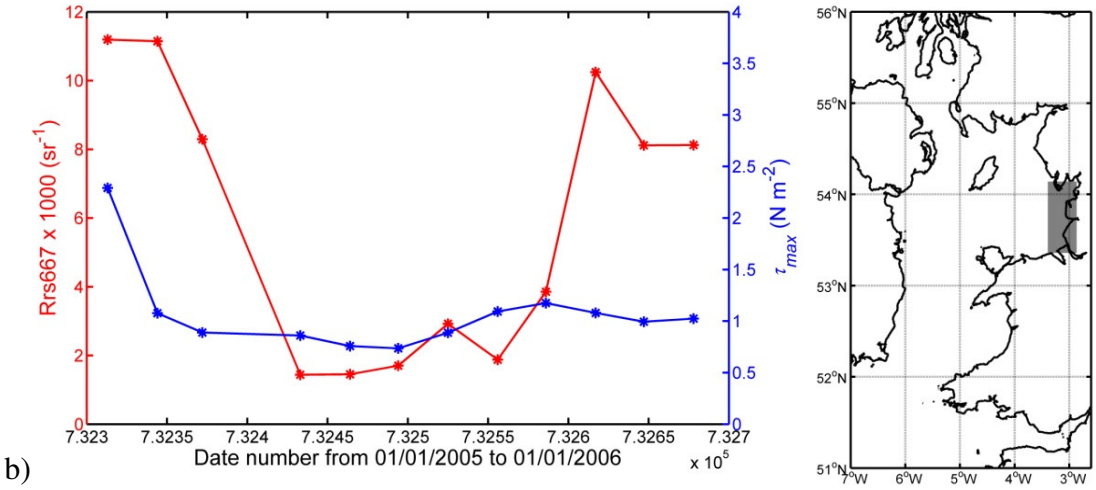
Rrs667 x 1000 (sr-1)
τmax (N m-2)
Date number from 01/01/2005 to 01/01/2006
x 10^5
7.323
7.3235
7.324
7.3245
7.325
7.3255
7.326
7.3265
7.327
56°N
55°N
54°N
53°N
52°N
51°N
7°W
6°W
5°W
4°W
3°W

b)

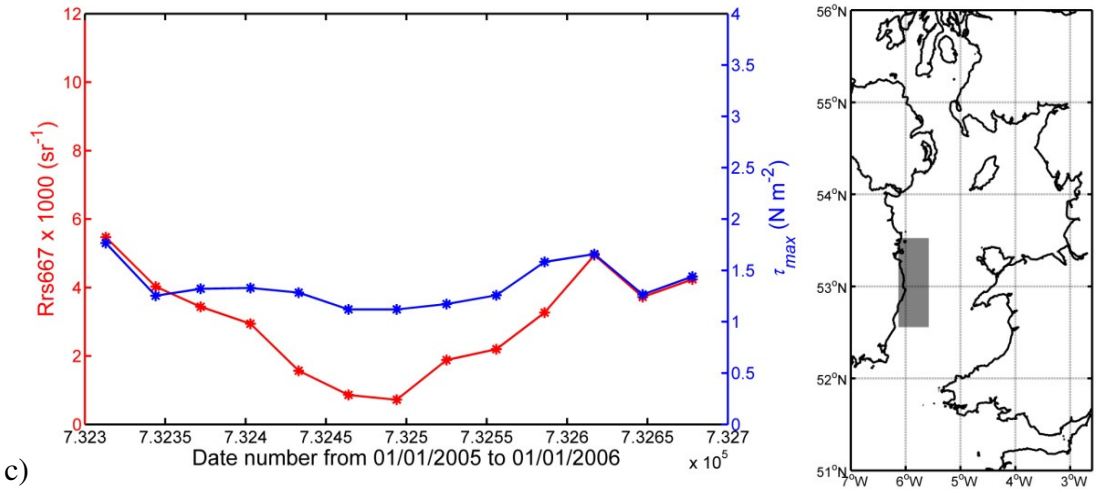
Rrs667 x 1000 (sr-1)
τmax (N m-2)
Date number from 01/01/2005 to 01/01/2006
x 10^5
7.323
7.3235
7.324
7.3245
7.325
7.3255
7.326
7.3265
7.327
56°N
55°N
54°N
53°N
52°N
51°N
7°W
6°W
5°W
4°W
3°W

c)

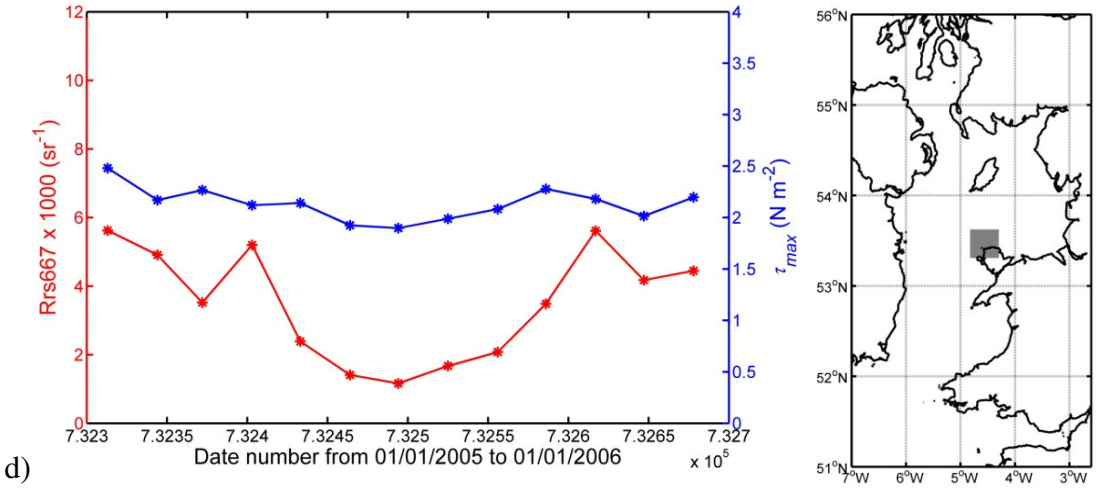
Rrs667 x 1000 (sr-1)
τmax (N m-2)
Date number from 01/01/2005 to 01/01/2006
x 10^5
7.323
7.3235
7.324
7.3245
7.325
7.3255
7.326
7.3265
7.327
56°N
55°N
54°N
53°N
52°N
51°N
7°W
6°W
5°W
4°W
3°W

d)

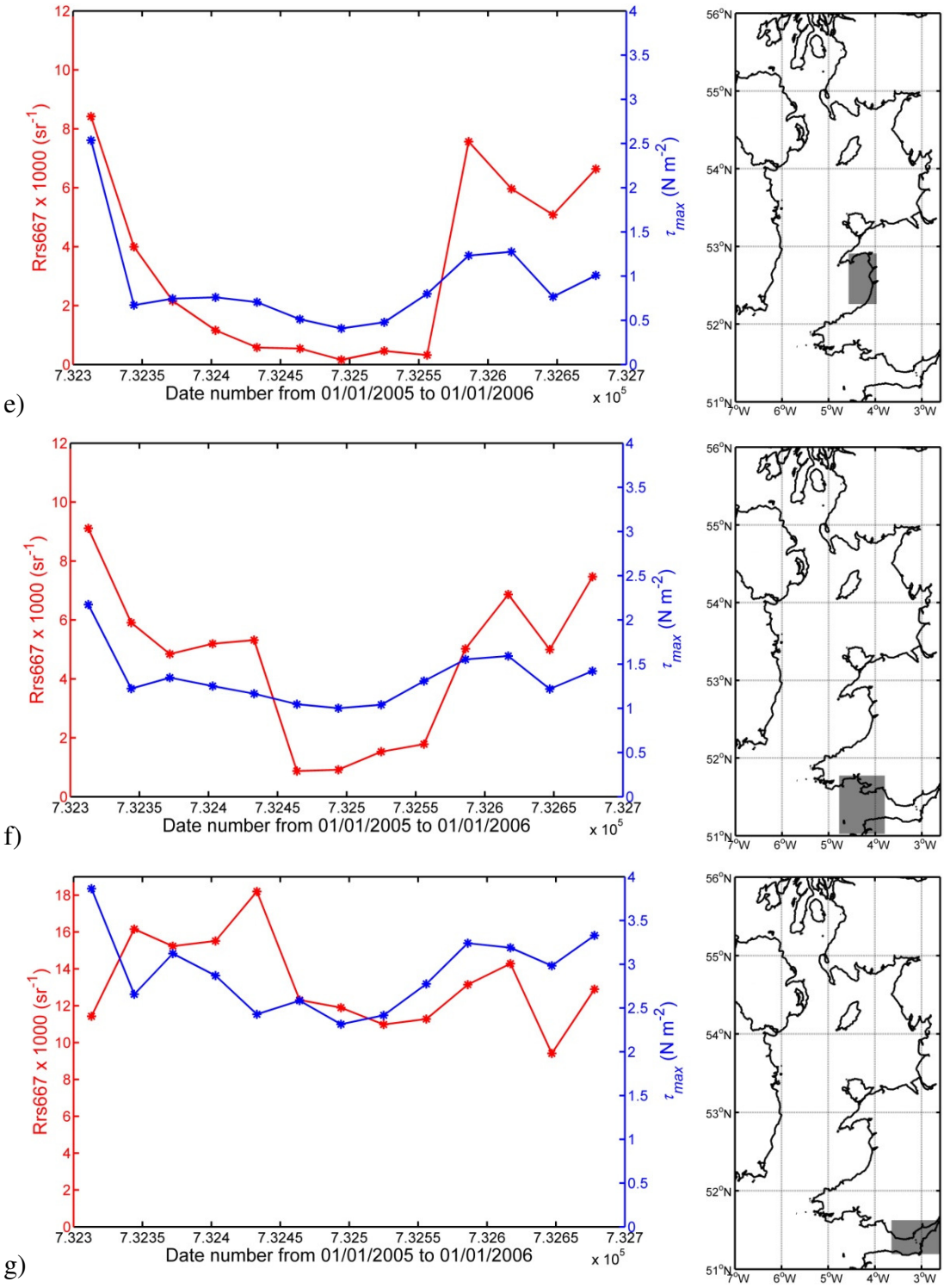

Figure 7.3 Time series of $R_{rs}667$ (red) and τ_{max} (blue) taken from several locations in the Irish Sea.

Marked variability is apparent in time series taken from the region of interest. These provide information on the optical and physical dynamics of the water column.

i) Figure 7.3 a) contains data extracted from Solway Firth. Seasonal variability in τ_{max} is apparent where lower values are found in summer months. Increases in $R_{rs}667$ appear to coincide with increased values of τ_{max}. Sporadic estimations of τ_{max} during summer months suggest sensitivity to wind-induced changes at this location.

ii) In Liverpool Bay, shown in Figure 7.3 b), seasonal changes in τ_{max} appear inconsistent. A significant reduction is apparent in spring resulting in a loss of sediment from the upper layer. The values remain consistently low during summer with a weak increase occurring in autumn, suggesting 2005 may have had a particularly calm winter. Further evidence is demonstrated by diminished levels of τ_{max} and $R_{rs}667$ in December months for all time series. Raised $R_{rs}667$ during autumn and winter implies the increase is sufficient to overcome the critical threshold of motion, τ_{cr}. This number must be exceeded for sediment resuspension to take place.

iii) At Wicklow Head, Figure 7.3 c), a small seasonal difference in τ_{max} corresponds to a reduction in MSS in summer. τ_{max} calculated at Anglesey, Figure 7.3 d), remain approximately consistent all year round. The corresponding variability in reflectance must be the result of an alternative forcing agent.

iv) A strong seasonal cycle is present in Cardigan Bay, Figure 7.3 e), with increased values of τ_{max} in winter generating more surface sediment.

v) Similarly, this pattern is apparent in the outer Bristol Channel, Figure 7.3 f). Moving towards the coast, τ_{max} recovered from the inner Bristol Channel τ_{max} remains the highest in the region, Figure 7.3 g). Here sediment dynamics are inconsistent with seasonal shear variations, suggesting another factor is forcing variability in this region.

7.5 Correlation analysis

The statistical dependence of $R_{rs}667$ on τ_{max} was evaluated by computing Spearman's rank correlation coefficient, ρ, (Wilcox, 2001). This non-parametric measure describes the effect of one data set on another;

$$\rho = 1 - \frac{6\sum d_i^2}{n(n^2-1)} \tag{7.2}$$

Here, $d_i = x_i - y_i$, is the difference between observational ranks (the order in which they lie in the n length data set). A Spearman correlation of 1 or -1 exists when two variables are monotonically related, even if their relationship is non linear. Contrastingly, a Spearman correlation of zero indicates there is no tendency for one data set to increase or decrease with the other. ρ coefficients were calculated for Irish Sea time series, shown in Figure 7.4, illustrating locations where $R_{rs}667$ and τ_{max} are statistically linked.

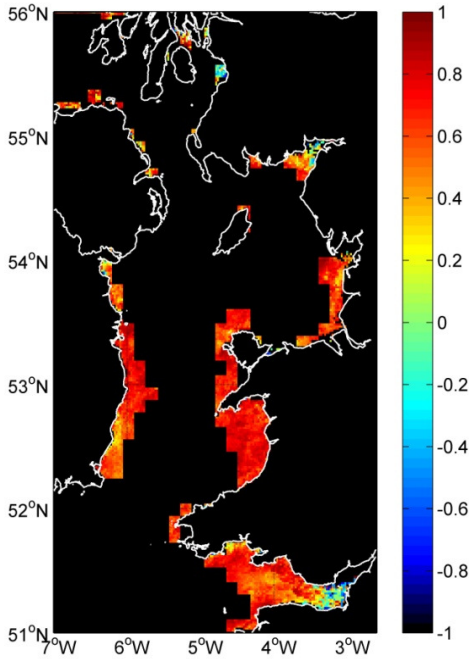

Figure 7.4 Spearman's correlation coefficient, ρ, calculated from Irish Sea time series. A value of 1 or -1 indicates a perfect monotonic relation exists between the parameters.

From this we have some indication as to where τ_{max} is controlling sediment dynamics in the Irish Sea. Significant correlation is demonstrated in Cardigan Bay and parts of Wicklow Head and the outer Bristol Channel, whilst negligible dependence is found at the inner Bristol Channel and Solway Firth.

7.6 Relationship between $R_{rs}667$ and τ_{max}

Further investigation was conducted by generating simple scatter plots of τ_{max} and normalised $R_{rs}667$, focussing on regions known to exhibit correlation between the two parameters. An example scatter plot containing data extracted from Cardigan Bay is shown in Figure 7.5. The non-linear trend exhibited in this example is common to the region. Data appears to exist in three groups, the first occurring at low values of τ_{max} and $R_{rs}667$. Here, increasing τ_{max} does not increase reflectance signals which remain close to zero. This could be due to levels of τ_{max} not exceeding the critical value required for sediment erosion, τ_{cr}. Next, the intermediate group containing spring/autumn and winter data show coincidental increase of $R_{rs}667$ and τ_{max}. A final group can be classified where maximum values of $R_{rs}667$ occur. Finite availability of sediment for suspension places an upper limit on the potential magnitude of $R_{rs}667$, translating as a plateau on the scatter plot. Increasing BSS will not continue to increase $R_{rs}667$ once the saturation point is reached. Scatter plots of these two variables appear to exhibit sigmoid curve characteristics, with an initial exponential stage inverting to a saturated plateau. The relationship between τ_{max} and $R_{rs}667$ can be described by an approximately logistic function of the form;

$$Y = \frac{1}{1+\exp(-z)} \tag{7.3}$$

where $z = \beta_0 + \beta_1 X$. Here β_0 is the curve intercept and β_1 controls the steepness of the sigmoid. A generalized linear model (GLM) was used with a logistic link function to effectively model reflectance values from τ_{max}. Coefficient estimates were determined at 5 locations in the Irish Sea by application of a least squares optimisation routine. Predicted values for the generalized linear model (solid lines) are shown with corresponding observations (points) in Figure 7.6.

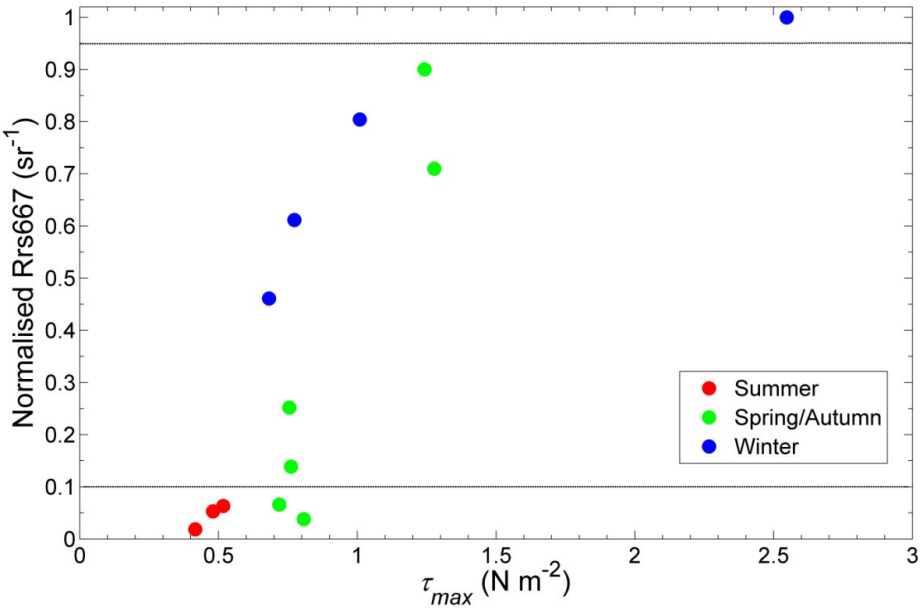

Figure 7.5 Scatter plot of τ_{max} Vs $R_{rs}667$ showing three seperate levels of data. The seasonal behaviour of $R_{rs}667$ offers some insight into hydrological dynamics controlling sediment variability.

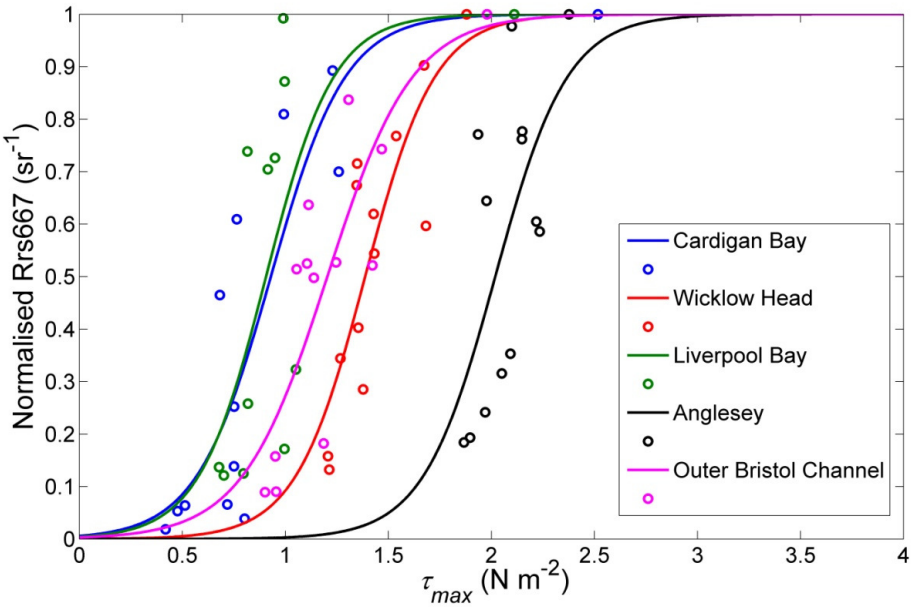

Figure 7.6 Logistic regression model (lines) applied to Irish Sea time series data (points). Generalized model coefficients determined by least squares regression.

Coefficient variability can be seen clearly from modelled predictions. Whilst steepness (β_1) remains relatively constant, the curve growth sections cover a wide range of values due to varying intercepts (β_0). For example, model predictions for Cardigan Bay (depicted in blue) estimate initial growth at $\tau_{max} \approx 0.25$ N m^{-2}, whereas the increase does not occur in Anglesey (black) until $\tau_{max} \approx 1.25$ N m^{-2}. This may be a consequence of geographically varying thresholds of sediment erosion, τ_{cr}, as $R_{rs}667$ cannot increase until τ_{max} exceeds this limit. Coefficient variability prevents development of a general formula connecting surface sediment patterns to bed shear stress. Nonetheless, error statistics from residual analysis, shown in Table 7.1, indicate a definite relationship exists between $R_{rs}667$ and τ_{max} at three locations in the Irish Sea, Cardigan Bay, Wicklow Head and the outer Bristol Channel.

Table 7.1 Error statistics for logistic regression models.

LOCATION	R^2	RMSE
Cardigan Bay	0.7702	0.1924
Wicklow Head	0.7134	0.1533
Outer Bristol Channel	0.6549	0.1722
Liverpool Bay	0.4086	0.2857
Anglesey	0.4031	0.2322

7.7 Estimates of threshold shear stress for sediment erosion, τ_{cr}, (N m^{-2})

The threshold BSS for erosion is an important factor for coastal engineering studies. It determines whether stresses applied to the sea floor by wave and current flows are sufficient to erode and resuspend sediment in the water column. Using scatter plots of τ_{max} and $R_{rs}667$, τ_{cr} can be estimated from generalized linear model coefficients. It is reasonable to assume that critical values for erosion have been exceeded when sediment levels reach half their potential magnitude. Assigning Y = 0.5 sr^{-1}, equation (7.3) can be rearranged to give;

$$X = \frac{-\beta_0}{\beta 1} \qquad (7.4)$$

This is the value of τ_{max} where $R_{rs}667$ equals half of the total signal and provides an indication of expected τ_{cr}. Maps of τ_{cr} are obtained by applying this technique to regions of the Irish Sea containing regression R^2 values greater than 0.6, Figure 7.7. Validation is challenging due to insufficient availability of field data, however laboratory measurements of τ_{cr} published by HR Wallingford (Whitehouse et al., 2000) can be used for approximate comparison (Table 7.2). These show that values of τ_{cr} predicted by equation (7.4) are within recognised UK ranges. However further validation is required to accurately assess retrievals and associated errors.

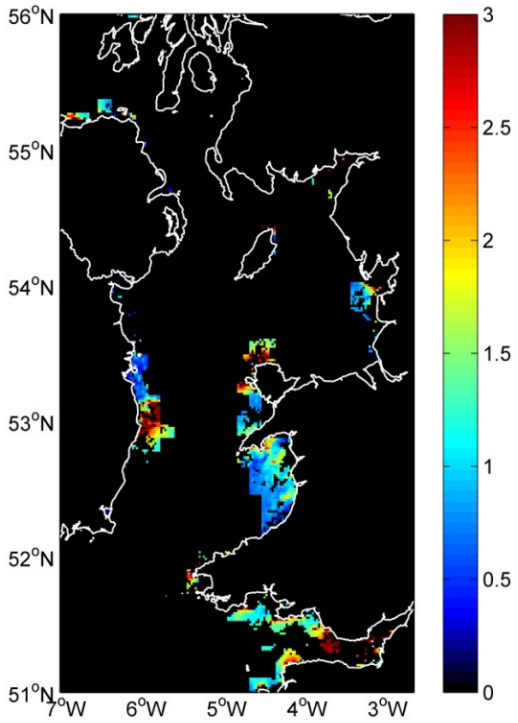

Figure 7.7 τ_{cr} (N m^{-2}) calculated from generalized linear model coefficients.

Table 7.2 Erosion properties determined in laboratory tests with muds extracted from UK locations.

LOCATION	τ_{cr} (N m^{-2})
Cardiff Ely	1.1
Cardiff Rhymney	2.5
Fawley	2.2
Grangemouth	1.4
Harwich	1.8
Ipswich	4.4
Kingsnorth	1.6
Medway	1.4
Mersey	0.8

7.8 Discussion

Coastal shelf seas remain the most productive yet endangered part of our marine environment and thorough coastal management is essential for its long term protection. Satellite remote sensing provides a means of studying mesoscale changes and long term trends in biogeochemical and physical processes. This chapter explored the extent to which information on physical dynamics can be obtained from ocean colour, in particular, the relationship between $R_{rs}667$ and the parameter controlling sediment resuspension, τ_{max}. The hypothesis that increases in τ_{max} would result in raised levels of surface sediment was investigated using MODIS Aqua observed reflectance and POLCOMS modelled waves and currents. Focussing on high reflectance variance regimes, time series analysis demonstrated the existence of a correlation between these two parameters in several regions of the Irish Sea, mainly Cardigan Bay, the outer Bristol Channel, Wicklow Head, Liverpool Bay and Anglesey. τ_{max} appears to influence the magnitude of surface sediment as well as temporal patterns. Moreover, this initial analysis indicated sediment variability was not a function of τ_{max} in the inner Bristol Channel or Solway Firth. Results were corroborated by determination of the statistical dependence between $R_{rs}667$ and τ_{max} through calculation of Spearman's rank correlation coefficient. At locations

consistent with the hypothesis, the relationship between $R_{rs}667$ and τ_{max} was an approximately logistical function. Coefficients determined through generalized linear modelling were variable throughout the test site, preventing the development of a general formula. Residual analysis highlighted three main regions where sediment dynamics were controlled by τ_{max}, mainly Cardigan Bay, the outer Bristol Channel and Wicklow Head. Here estimations of the threshold of erosion were generated by a simple ratio of generalized linear model coefficients. Regions inconsistent with the hypothesis are; the Inner Bristol Channel, Solway Firth, Liverpool Bay and Anglesey. At these locations, additional physical processes appeared to be driving sediment variability. For example, it may be reasonable to assume that the Bristol Channel and Solway Firth estuaries require an alternative approach as their characteristics are inconsistent with open shelf seas. This is also true in Liverpool Bay, where the complex physical dynamics driven by freshwater input may cause deviations from a simple relationship. At this location sediment deposition appeared to correspond to a reduction in τ_{max} however resuspension of sediment was not the result of increased shear. In Anglesey, τ_{max} was shown to be relatively constant; however sediment patterns exhibited annual periodicity. This suggests an alternative physical process is causing sediment to fall during summer periods. One suggestion is the existence of biologically mediated cohesion, increasing the mass, and subsequently the settling velocity, of MSS and causing it to fall out of the surface layer (Jago et al., 2006). Sediment variability in this region may be a consequence of horizontal advection processes whereby sediment is transported to a location horizontally rather than vertically from the sea floor (Perianez et al., 2002). In this case, a reduction in wind strength would reduce the magnitude and frequency of horizontally advected sediment concentrations thus producing lower surface estimates. These inconsistencies point to further work in the field. Nonetheless, investigation of the existence of potential relationships between hydrological and optical parameters is providing novel insights into the physical dynamics controlling sediment variability in coastal shelf seas.

Key points from chapter 7

1. For 2005, modelled wave and current data were extracted from the POLCOMS-WAM model and used to calculate maximum bed shear stress in the Irish Sea high variance regions. Time series were created by combining daily average values. Monthly composites of $R_{rs}667$ were also combined to generate 2005 reflectance time series.

2. Images of τ_{max} were created to show seasonal and spatial variability in the region of interest.

3. Concurrent time series analysis of τ_{max} and $R_{rs}667$ showed regions where increased $R_{rs}667$ coincided with increases in τ_{max}. This was further demonstrated by correlation analysis.

4. Scatter plots were used to show an approximate logistic function connects $R_{rs}667$ and τ_{max} at various high variance regions of the Irish Sea. Error statistics for logistic regression modelling showed in Cardigan Bay, the outer Bristol Channel and Wicklow Head increasing τ_{max} results in increased $R_{rs}667$.

5. Inconsistencies were found at the Inner Bristol Channel, Solway Firth, Liverpool Bay and Anglesey. At these locations, additional physical processes are driving sediment variability.

6. The critical value for sediment erosion can be estimated using ocean colour data at locations were sediment dynamics are controlled by the magnitude of bed shear stress.

References

Aldridge, J.N., Kershaw, P., Brown, J., McCubbin, D., Leonard, K.S., Young, E.F., 2003. Transport of plutonium (Pu-239/240) and caesium (Cs-137) in the Irish Sea: comparison between observations and results from sediment and contaminant transport modelling. CONTINENTAL SHELF RESEARCH, 23 (9), 869-899.

Bowers, D.G., Ellis, K.M., Jones, S.E., 2005. Isolated turbidity maxima in shelf seas. CONTINENTAL SHELF RESEARCH, 25 (9), 1071-1080.

Dobrynin, M., Gayer, G., Pleskachevsky, A., Gunther, H., 2010. Effect of waves and currents on the dynamics and seasonal variations of suspended particulate matter in the North Sea. JOURNAL OF MARINE SYSTEMS, 82 (1-2), 1-20.

Ellis, K.M., Binding, C.E., Bowers, D.G., Jones, S.E., Simpson, J.H., 2008. A model of turbidity maximum maintenance in the Irish Sea. ESTUARINE COASTAL AND SHELF SCIENCE, 76 (4), 765-774.

Jago, C.F., Jones, S.E., Sykes, P., Rippeth, T., 2006. Temporal variation of suspended particulate matter and turbulence in a high energy, tide-stirred, coastal sea: Relative contributions of resuspension and disaggregation. CONTINENTAL SHELF RESEARCH, 26 (17-18), 2019-2028.

Jones, S.E., Jago, C.F., Bale, A.J., Chapman, D., Howland, R.J.M., Jackson, J., 1998. Aggregation and resuspension of suspended particulate matter at a seasonally stratified site in the southern North Sea: physical and biological controls. CONTINENTAL SHELF RESEARCH, 18 (11), 1283-1309.

Krivtsov, V., Howarth, M.J., Jones, S.E., Souza, A.J., Jago, C.F., 2008. Monitoring and modelling of the Irish Sea and Liverpool Bay: An overview and an SPM case study. ECOLOGICAL MODELLING, 212 (1-2), 37-52.

Perianez, R., 2002. Modelling the suspended matter dynamics in a marine environment using a three dimensional sigma coordinate model: application to the eastern Irish Sea. APPLIED MATHEMATICAL MODELLING, 26 (5), 583-601.

Soulsby, R.L., Clarke, S., 2005. Bed Shear-stresses Under Combined Waves and Currents on Smooth and Rough Beds. Defra project FD1905 (EstProc), TR 137, Rev 1.0.

Stanev, E.V., Wolff, J.O., Brink-Spalink, G., 2006. On the sensitivity of the sedimentary system in the East Frisian Wadden Sea to sea-level rise and wave-induced bed shear stress. OCEAN DYNAMICS, 56 (3-4), 266-283.

Stanev, E.V., Dobrynin, M., Pleskachevsky, A., Grayek, S., Gunther, H., 2009. Bed shear stress in the southern North Sea as an important driver for suspended sediment dynamics. OCEAN DYNAMICS, 59 (2), 183-194 Sp. Iss. SI.

van der Lee, E.M., Bowers, D.G., Kyte, E., 2009. Remote sensing of temporal and spatial patterns of suspended particle size in the Irish Sea in relation to the Kolmogorov microscale. CONTINENTAL SHELF RESEARCH, 29 (9), 1213-1225.

Vos, R.J., ten Brummelhuis, P.G.J., Gerritsen, H., 2000. Integrated data-modelling approach for suspended sediment transport on a regional scale. COASTAL ENGINEERING, 41 (1-3), 177-200.

Whitehouse, R., Soulsby, R., Roberts, W., Mitchener, H., 2000. Dynamics of estuarine muds. Thomas Telford Publishing, London, 48-49.

Wilcox, R., 2001. Fundamentals of Modern Statistical Methods: Substantially Improving Power and Accuracy. Springer Publishing, London, 190-195.

Chapter 8

Conclusions and future work

Summary

This chapter contains the conclusions drawn during the course of the work presented in this thesis. A brief general discussion is presented prior to specific conclusions relating to each issue identified in chapter 1. This chapter concludes with recommendations for future work in the field.

8.1 General discussion: summary of work

The multidisciplinary nature of this project required a number of different data collection techniques. The first phase of the study concentrated on satellite measurements of reflectance. Over 200 satellite images covering the Irish Sea were obtained and processed during the course of this study, creating an extensive image archive. Processing was carried out using SeaDAS software, which incorporated the default 2-band aerosol model with iterative NIR correction. Various Matlab programming scripts were developed for data analysis and image processing. A simple validation was performed with the small number of available in-situ matchups which indicated remote sensing reflectance values were recorded at sufficient accuracy to be utilised in the study. The second aspect of the research was concerned with data derived from in-situ optical measurements obtained from various Irish Sea research cruises. These were predominantly used for algorithm validation purposes. SPMR measurements of radiance and irradiance were collated with water sample analyses and quality checked to create a dataset suitable for interdisciplinary comparisons. An alternative processing routine was developed to correct a ProSoft processing error uncovered during the course of the study. The third aspect of the research focussed on radiative transfer modelling. IOPs, determined as the product of SIOPs and varying combinations of optically significant constituents, were supplied to the Ecolight radiative transfer numerical modelling package to simulate shelf sea radiance distribution. This generated 20328 model runs suitable for effective

representation of the Irish Sea optical environment. Validation of Ecolight model outputs with in-situ reflectance data showed that reflectance is sufficiently modelled at red wavelengths. Matlab scripts were created to assist with Ecolight batch processing and the extraction of data from output files. The final phase of this study required hydrodynamic data from the POLCOMS numerical modelling system. This was provided by the Proudman Oceanographic Laboratory along with several Matlab scripts developed for data extraction. Temperature and salinity calculated at the top and bottom of the water column were used in conjunction with depth to determine density from the equation of state. Surface temperature values predicted by the model were validated using MODIS Sea Surface Temperature data. This indicated that the locations of hydrodynamic features such as thermal fronts were not affected by the existence of a temperature offset. Comparison of top and bottom density values provided an indication of stratification, whereby large differences in density were indicative of a stratified water column. The use of $\Delta\sigma$ as an effective stratification parameter was confirmed using in-situ measurements of water column density structure. Stations exhibiting density gradients in CTD *sigma-T* profiles were located in regions of stratification predicted by the $\Delta\sigma$ parameter. As a final step, Irish Sea maximum bed shear stress, τ_{max}, was calculated from POLCOMS-WAM wave and current data.

Chapter 4, which focussed on the development of an algorithm appropriate to recovering MSS concentration from optically complex seas, contained the first primary results of the study. Using a combination of water sample analyses and radiance transfer simulations, it was shown that reflectance measured at red wavelengths was the optimal parameter for remote sensing of MSS. The effect of CHL and CDOM on the MSS recovery was also determined through use of radiance transfer modelling. The algorithm presented in chapter 4 recovers MSS as a function of other optically significant materials. It relies on the assumption that concentrations of CHL and CDOM lie within the specified range of the model. By recovering a range of MSS for a given $R_{rs}667$ signal, the retrieval error is encompassed in the estimate. Through comparison with in-situ observations, a degree of optical closure was obtained. The variability observed in field measurements of reflectance can be

explained by the presence of other optically significant constituents. Application of the algorithm to satellite $R_{rs}667$ data accurately reproduced known sediment feature sin the Irish Sea. It was demonstrated, therefore, that $R_{rs}667$ can be used as a suitable indicator of surface sediment concentrations.

Chapter 5 contained a detailed description of $R_{rs}667$, and by implication MSS, variability in the Irish Sea. Time series of $R_{rs}667$ were generated at each point of a mesh grid devised to cover the extent of the test site, reducing the computational time and memory storage required for 181 satellite images. A reprocessing routine was developed to normalise data and fill gaps corresponding to cloud cover in satellite images. A by-product of this routine demonstrated that no linear trend exists in the Irish Sea reflectance dataset. Using autocorrelation analysis, the periodicity of reflectance variability was defined as annual for the majority of the test site. Time series statistics could effectively highlight hydrological features. Reflectance variance was used to objectively classify the region into two regimes exhibiting distinct optical characteristics. It can therefore be assumed that surface sediment patterns observed in each regime are controlled by different physical processes. The test site was further classified by considering the distribution of time series points around their mean value. This technique can also be improved by considering duration spent below a threshold value of the average Irish Sea minimum reflectance. Both methods highlight hydrological features and can be used as a temporal predictor of water column clarification.

Chapter 6 used the variance objective classification formed in chapter 5 to analyse low variance reflectance pixels in terms of stratification. Time series of monthly average modelled $\Delta\sigma$ were generated for the 2006 model run, along with time series of monthly composites of satellite $R_{rs}667$ for the same period. Maps of stratification were composed to display spatial and temporal changes across the region of interest. Using histograms of average $\Delta\sigma$ and the duration spent below the spatial minimum reflectance, the Irish Sea was subdivided into three groups with distinct hydrological and optical characteristics. Comparison of the physical and optical pixels contained within each group provides information on regions in which a simple relationship

correlates stratification and $R_{rs}667$. Furthermore, this technique also highlighted geographical locations in the Irish Sea where a more complex relationship exists between the two parameters. Investigation of time series at locations of inconsistencies showed sediment and stratification dynamics were out of phase. This was used to provide a potential explanation for the failure of a simple relationship. Nonetheless, for the majority of the low variance region, a power law correlates stratification and $R_{rs}667$. As the water column begins to stratify, the magnitude of $R_{rs}667$ decreases. By applying transects to satellite images, it was shown that $R_{rs}667$ can be used as a qualitative indicator of stratification. However, the reflectance signal cannot determine the degree to which the water column is stratified.

Chapter 7 focussed on high variance pixels to investigate changes in surface sediment patterns as a function of varying bed shear stress. For this study, the 2005 time series of monthly maximum bed shear stress, τ_{max}, were generated by averaging daily maximum values. Monthly composites of $R_{rs}667$ were also combined to compose a time series of satellite data for the same period. Images of τ_{max}, were produced to illustrate how bed shear stress changes spatially and temporally, where the wave component adds a seasonal factor to the total value. Time series demonstrated the optical variability in conjunction with τ_{max} and it was shown at several locations, $R_{rs}667$ values intensified with increased levels of τ_{max}. In these regions, τ_{max} was controlling sediment resuspension. This was also demonstrated through correlation analysis, which proved useful for indentifying areas where no relationship existed between $R_{rs}667$ and τ_{max}. Locations where sediment dynamics are not attributable to τ_{max} are Anglesey, the inner Bristol Channel and Solway Firth. In Cardigan Bay, the outer Bristol Channel and Wicklow Head, an approximately logistic function connects $R_{rs}667$ and τ_{max}. Coefficients from a generalized linear model of these parameters were used to predict the threshold for sediment erosion.

8.2 Implications

This section reviews the key issues identified in chapter 1.

1. *Can methods of quantitatively interpreting satellite images in optically complex waters be developed?*

Attempts to develop algorithms that are capable of the simultaneous recovery of CHL, MSS and CDOM, often encounter difficulties (Sathyendranath 2000). The problem is made simpler by considering only one constituent. This study has demonstrated that it is possible to develop methods for quantitatively deriving MSS from reflectance signals measured over optically complex waters. Using a combination of radiative transfer modelling and in-situ field observations, an algorithm specific to the recovery of MSS concentrations has been designed (equation 4.4). Radiative transfer modelling is an excellent tool for investigating parameters that influence the light distribution in shelf seas, and complements the traditional empirical analysis of field data. The use of radiative transfer modelling provides insights into potential sources of error, such as the affect of other optically significant constituents on the MSS retrieval. The algorithm developed during the course of study incorporates this error in the result. Radiance transfer calculations were conducted using SIOPs representative of UK shelf waters. In reality, even in a small geographical area such as the region of interest, SIOPs may exhibit significant variability. However, from equation (1.28) the numerator is controlled predominantly by MSS backscattering. Even if the CHL backscattering SIOP was increased by a factor of 5, backscattering by MSS would remain the dominant parameter for this region where concentrations of MSS are relatively high, meaning the relationship would stay unchanged. This leaves the specific absorption coefficients. Increasing a*CHL by a factor of 5 would result in the denominator being controlled by seawater and CHL concentration. In this case, the boundaries of the MSS retrieval range would be altered. Nonetheless, the proposed retrieval method captures the range of a*CHL values derived from optical measurements of UK shelf seas and could be altered to best represent optical properties of other locations. For this reason, a general algorithm covering the extent of a large region, for example, the European

continental shelf, is not applicable. Algorithms must be optimised to embody local optical characteristics. Knowledge of the physical dynamics of the water column may also assist with this process. By applying, *a priori* conditions, the maximum algorithm boundaries can be restricted. For example, during winter periods the modelled range of CHL can be reduced, resulting in a refinement of the retrieved MSS values. Once MSS has been recovered from the reflectance signal, it may be possible to infer concentrations of the remaining constituents, in particular CDOM. Figure 8.1 a) shows $R_{rs}667$ against $R_{rs}443$ calculated by radiance transfer modelling, where concentrations of CHL, MSS and CDOM lie within the ranges specified in chapter 4. Each colour on the figure represents a different concentration of MSS. Figure 8.1 b) shows the same ratio of reflectance, however in this example each colour represents a different concentration of CDOM. It may be possible to estimate the concentration of CDOM from the y-axis intercept (Figure 8.1 b) once the MSS group has been established. This points to future work in the field.

a)

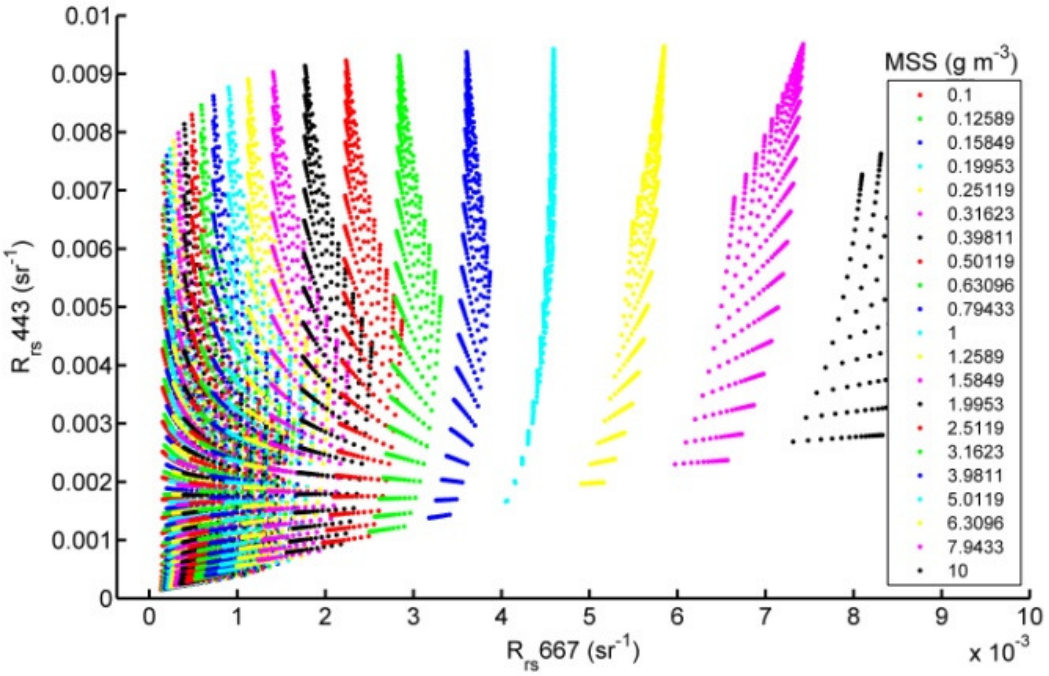

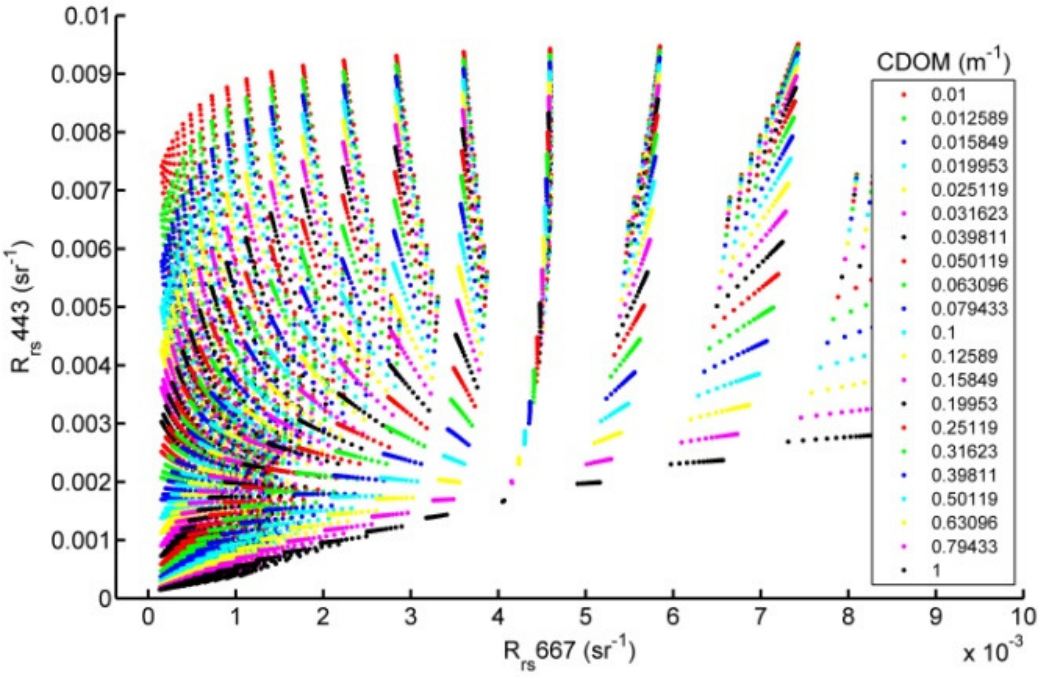

b)

Figure 8.1 Ratio of reflectance measured at blue and red wavelengths. Colour points represent different concentrations of a) MSS and b) CDOM. The range of points is determined from combinations of each constituent supplied to the model. There is some indication that CDOM concentrations could be estimated from $R_{rs}443$ once the MSS group has been classified.

2. *Given the existence of a significant archive of ocean colour images, is it possible to reconstruct temporal events from time series, even in areas such as the UK where there is high cloud cover?*

Ocean colour images can be combined to generate time series of satellite data, allowing the investigation of the temporal patterns of reflectance. Analysing satellite measurements in this way can yield more information than an individual image. Seasonal changes and long term trends can be surmised from the time series dataset, whilst cross comparisons provide information relating to the spatial consistency of variability. There exist various methods for analysing time series datasets, including resampling and interpolation procedures which essentially replace missing data in the series. This is particularly useful in regions such as the Irish Sea where few cloud free images are produced each year. Provided there are sufficient cloud free pixels to compose monthly composite images, temporal events such as maxima and minima can be accurately reconstructed by integration of satellite data. This was highlighted by results shown in chapter 5, where 5 years of seasonal patterns were effectively recreated from 181 satellite images. If however a significant break in the data set exists, interpolation methods assign erroneous values to the relevant increment space. Here, numerical shelf sea models could prove useful in predicting missing values. Time series analysis may assist with operational prediction and modelling purposes, where statistics could provide information on frequency and probability distributions. Coincident analysis with physical dynamics offers a real insight into the mechanisms driving reflectance variability in shelf seas. Time series analysis has proven crucial for this study and forms the basis of the main results presented in this thesis.

3. *Is it possible to use ocean colour radiometry to gain useful insights into physical processes in shelf seas beyond patterns of primary productivity?*

The determination of patterns of primary productivity is commonly regarded as one of the fundamental objectives of ocean colour remote sensing. However the reflectance measured remotely by satellite can be utilised to provide information on a range of other processes. This study has demonstrated the potential of gaining useful insight into physical processes influencing shelf seas by analysing the dynamics of sediment (chapters 6 and 7). To do this, MSS was treated as a tracer of the water column hydrodynamics and ocean colour images were used to map surface sediment patterns. A rise in $R_{rs}667$ during winter periods was attributed to a well mixed water column or increased bed shear stress, whilst reductions of the reflectance signal in summer may signify water column stratification. Spatial patterns of $R_{rs}667$ could also be associated with physical processes through comparisons with tidal current velocities. Maximum values of $R_{rs}667$ are often observed in regions containing strong tidal currents. These examples illustrate how spatial and temporal patterns of suspended sediment can provide information on physical processes. This technique may also be extended to consider alternative optical constituents such as CDOM, whose dynamics could be closely monitored at the ocean-continent interface to investigate, for example, the influence of river runoff. Satellite data recorded at higher resolution (MERIS Full Resolution/ESA) would be required to enhance detail. Formal establishment of relationships between ocean colour and physical properties may assist with the development of hydrodynamic models as satellite imagery could be used to tune the model to better replicate hydrological features such as thermal fronts.

4. *Can it be demonstrated that surface reflectance signals are driven by processes deeper in the water column?*

One recent development in shelf sea science is the creation of high resolution numerical models. The tuning and validation of these models requires a synoptic view of shelf sea processes that is difficult to obtain from ship-based sampling or instrumented moorings. Ocean colour observations can potentially fulfil this requirement if it can be demonstrated that the surface signals are driven by processes deeper in the water column. This study has shown that this condition is true for the Irish Sea. Using coincident analysis of satellite remote sensing data and oceanic properties derived from a numerical model, the relationship between surface $R_{rs}667$ and water column stratification was quantified for the region of interest (chapter 6). Reflectance signals generally begin to fall at the onset of stratification. Values at the surface can only be measured in regions of non-stratified water. However, the inverse statement is not true; a mixed water column does not ensure a reflectance signal will be detected. Because of this, the relationship between $R_{rs}667$ and water column stratification is a complex one. In an attempt to explain regions of inconsistency, $R_{rs}667$ was investigated in conjunction with bed shear stress (chapter 7). This physical parameter is known to control sediment resuspension in shallow waters. It was demonstrated at various locations that reflectance values changed according to the magnitude of stress applied at the sea bed. As with stratification, there were regions where sediment dynamics appeared to be influenced by alternative physical processes. However, for the majority of the test site, surface values of $R_{rs}667$ could be explained by the mechanisms driving reflectance variability. Figure 8.2 shows a hierarchal diagram of established relationships, and locations identified as requiring further study. Results presented in chapters 6 and 7 could be improved and validated using in-situ data. However this was unavailable at the time of writing.

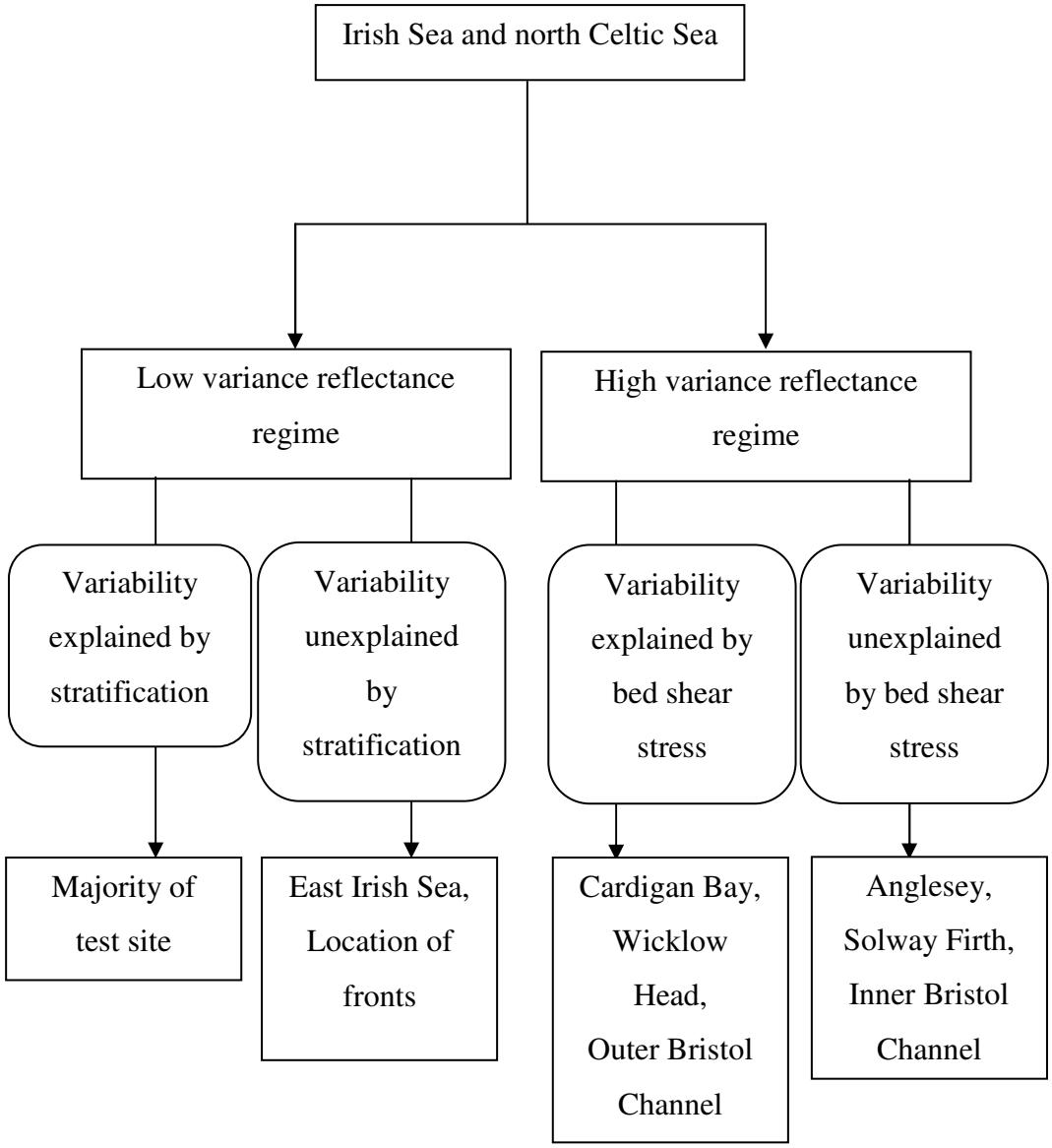

Figure 8.2 Hierarchal diagram of regions in which reflectance variability is explained by physical process.

5. *Is it possible to infer directly from ocean colour, physical properties of the water column through development of simple algorithms?*

Having established that reflectance variability observed in the majority of the Irish and north Celtic Sea can be related to physical processes, this study has further demonstrated the difficulty of extracting quantitative properties of these processes from the reflectance signal. For a large area of the test site, a power law relationship exists between satellite measured $R_{rs}667$ and model derived stratification. At these locations, the reflectance signal could be used to predict the difference in density using an equation of the form (6.2). This result would be strengthened by validation with in-situ field data, but this was not available at the time of writing. For regions containing more a complex relation, $R_{rs}667$ cannot determine the extent of stratification. The inverse argument for mixing is also true. Mixing of the water column may result in increased reflectance but the magnitude of mixing does not determine how much reflectance, and by implication MSS, will be measured at the surface. The breakdown of a simple relationship serves as a reminder of the physical complexity of this relatively small region. In shallow waters, a logistic function correlates $R_{rs}667$ and maximum bed shear stress. Therefore, to derive τ_{max} from the reflectance signal, one would require *a priori* knowledge of the logistic steps and intercept. Coincident analysis of modelled τ_{max} and $R_{rs}667$ has presented a simple equation for estimating the threshold stress for sediment erosion from satellite ocean colour. If corroborated with in-situ data, this could prove an extremely useful result.

8.3 Suggestions for future work

The results presented in this thesis illustrate the effectiveness of a multidisciplinary approach to interpreting satellite ocean colour data and open up an exciting new field of study. The method applied to retrieving MSS concentrations from ocean colour may be extended to include other constituents such as CDOM. This may prove useful when attempting to understand the effects of freshwater processes, such as river runoff, at the ocean-continent interface. Coincident analysis with hydrodynamic models could also be extended to include sedimentary models. This would be useful for validation purposes, particularly model validation. The fundamental objective of this type of research is assimilation of satellite remote sensing data into hydrodynamic models. This work could be extended to assist this difficult task. For example, ocean colour derived measurements of MSS could be applied as an initialization parameter for sediment transport models. Consecutive ocean colour images would then provide continued initialization or validation tools. As mentioned previously in this work, satellite ocean colour images could also be utilised to better represent hydrological features such as thermal fronts. Moreover, assimilation of into numerical models could essentially fill the gaps in satellite time series. Accurate assimilation of ocean colour into ocean numerical models offers major research potential.

In the context of this work, further research is required to explain reflectance variability at several locations in the Irish Sea. Incorporation of particle size distributions may shed light on the complex dynamics observed in Anglesey, whilst the Solway Firth and the inner Bristol Channel require an alternative hydrodynamic descriptor. This is also true for the eastern Irish Sea, where intricate relations with salinity stratification govern sediment resuspension and deposition. All results would be strengthened with the availability of additional in-situ data, obtained from research cruise expeditions or fixed moorings. These issues point to the need for further work in the field.